UNIVERSITÀ DEGLI STUDI FIRENZE

European Laboratory for Non-Linear Spectroscopy
(LENS)

Doctoral School in Atomic and Molecular Photonics
Ciclo XXXV

Single photon emitters

Candidate

Andrea Ristori (ID number DT30541)

Thesis Advisor

Prof. Francesco Biccari

Director

Prof. Diederik Wiersma

Academic Year 2021/2022

Thesis not yet defended

Single photon emitters

PhD thesis. University of Florence

© 2023 Andrea Ristori. All rights reserved

This thesis has been typeset by LaTeX and the UniFiTh class.

Version: March 18, 2023

Author's email: andrea.ristori@unifi.it

Abstract

Single photon emitters (SPEs) are the most promising candidates for the implementation of Quantum Information Technologies (QIT). A SPE is a light source that emits, on demand, one photon at a time in a pure quantum state. The possibility to control the properties of the emitted photon makes them perfectly suitable for applications in Quantum Cryptography and Quantum Computing.

Among the different processes to generate single photons, the most promising ones are solid-state SPEs. They consist in emitters embedded in a solid-state matrix which makes them easily identifiable, controllable and integrable in photonic circuits. Solid-state SPEs can be divided in two main groups: luminescent point defects and quantum dots (QDs). The former are defects formed in the crystalline structure, whose presence leads to the formation of energy levels within the energy gap of the hosting material. The latter are small volumes of semiconductor embedded in a material with a higher energy gap. This leads to a 3D confinement of the charges and thus to an atom-like energy level structure.

In this thesis work we have focused on two different solid-state SPEs: isolated $GaAs_{1-x}N_x$ QDs and ensemble of G-centers (luminescent point defects in silicon).

Regarding the former, we present the results of a recently developed fabrication technique for the realization of $GaAs_{1-x}N_x$ QDs. Exploiting the properties of $GaAs_{1-x}N_x$ and the use of photonic jets (PJ), which are intense light beam characterized by a sub-diffraction lateral size, we were able to laser-write QDs of different sizes. The PJs were obtained illuminating dielectric microsphere deposited on the sample, which had the additional advantage of increasing the collected luminescence emitted by the fabricated QDs. The QDs realized were thoroughly characterized by means of micro-photoluminescence (micro-PL) spectroscopy and their SPE nature was proved. Finally, we have reported the results of a novel set of simulations as a basis to achieve a better control over the fabrication process.

Concerning the G-centers, we present the results of a novel technique to tune their emission with strain. The technique is based on the realization of silicon suspended membranes, which are then strained depositing a silicon nitride layer on top. The presence of strain causes a splitting of the G-centers zero phonon line in two peaks. The energy difference between the peaks is directly related to the amount of strain introduced, which, in our technique, is controlled by changing the membranes size. Indeed, the realization of smaller membranes results in a stronger strain and vice versa. Therefore, by simply engineering the material we were able to tune the G-centers emission. Moreover, we have proved that these manipulations do not affect the optical properties of the emitters.

It is worth mentioning that both techniques presented in this work can be applied to other SPEs that share similarities with the ones studied in this work. Moreover, these technique represent innovative approaches to solving know problems related to SPEs such as their realization, their limited brightness and the control over their emission.

Papers produced during the PhD

- "*Tuning G-centers emission with strain*", **A. Ristori**, M. Khoury, M. Salvalaglio, M. Abbarchi, F. Biccari
  Under preparation

- "*Photonic jets and single photon emitters*", **A. Ristori**, M. Felici, G. Pettinari, L. Pattelli, F. Biccari
  Advanced Photonics Research, 2100365 (2022)

- "*Near-field hyper-spectral imaging of resonant Mie modes in a dielectric island*", N. Granchi, M. Montanari, **A. Ristori**, M. Khoury, M. Bouabdellaoui, C. Barri, L. Fagiani, M. Gurioli, M. Bollani, M. Abbarchi, F. Intonti
  APL Photonics, 6, 126102 (2021)

- "*A new route for caesium lead halide perovskite deposition*", N. Falsini, **A. Ristori**, F. Biccari, N. Calisi, G. Roini, P. Scardi, S. Caporali, A. Vinattieri
  J. Eur. Opt. Soc.-Rapid Publ., 17 (1), 1-7, (2021)

- "*Photonic jet writing of quantum dots self-aligned to dielectric microspheres*", **A. Ristori**, T. Hamilton, D. Toliopoulos, M. Felici, G. Pettinari, M. Gurioli, H. Mohseni, F. Biccari
  Advanced Quantum Technologies, 4 (9), 2100045, (2021)

- "*Large-area nanocrystalline caesium lead chloride thin films: a focus on the exciton recombination dynamics*", N. Falsini, N. Calisi, G. Roini, **A. Ristori**, F. Biccari, P. Scardi, S. Caporali, A. Vinattieri
  Nanomaterials, 11 (2), 434, (2021)

- "*Quantum Dots Luminescence Collection Enhancement and Nanoscopy by Dielectric Microspheres*", F. Biccari, T. Hamilton , **A. Ristori**, S. Sanguinetti, S. Bietti, M. Gurioli, H. Mohseni
  Part. Part. Syst. Charact., 37 (1), 1900431, (2020)

Acknowledgments

Per primo vorrei ringraziare il mio relatore, Francesco. Ormai ci conosciamo sin dal periodo della mia tesi magistrale e in tutto questo tempo non è mai mancato nel suo ruolo di insegnante e di supporto alla mia attività di ricerca. Anche nei momenti più impegnativi e stressanti ha sempre avuto parole di incoraggiamento e di sostegno. Grazie ai suoi consigli e alla sua guida spero di essere riuscito a migliorare sia come ricercatore che come persona.

Vorrei poi ringraziare tutte le altre persone che mi hanno accompagnato in questo percorso e mi hanno consigliato, insegnato e supportato: penso ad Anna, Francesca e Massimo. Un grazie va anche a Nicoletta, Naomi, Giammarco e Pier Paolo con cui mi sono lamentato quando le cose non funzionavano e ho festeggiato quando (raramente) tutto filava liscio. Inoltre vorrei ringraziare Marco per avermi permesso di visitare e lavorare a Marsiglia, dove ho potuto accrescere le mie conoscenze in un ambito a me estraneo e dove ho potuto conoscere altre persone interessanti come Momo, Driss e Mario. A quest'ultimo va un ringraziamento speciale per la sua amicizia, per la sua vicinanza quando ero lontano da casa e per tutte le gioie e sofferenze che abbiamo condiviso nel fabbricare e misurare i campioni che hanno infine costituito gran parte di questo lavoro.

Un ringraziamento va anche ai compagni di pause pranzo e di caffè quotidiani con cui poter parlare di tutto e non solo di Fisica: Tommi, Save, Vio, Francesca e Josephine. Grazie agli amici di sempre (fisici e non), perdonatemi se non vi elenco tutti altrimenti non si finisce più, sappiate che anche senza vedersi quotidianamente mi avete aiutato in questo percorso. Mi dispiace se sto dimenticando qualcuno, ma sappiate che sono grato a tutte le persone con cui sono entrato in contatto durante il dottorato e che lo hanno reso un'esperienza indimenticabile.

Vorrei poi ringraziare i miei genitori per avermi supportato (e, come sempre, sopportato) durante questo periodo anche se non capivano cosa stessi facendo (ma soprattutto perché). Grazie di cuore, mi siete sempre stati vicini senza mai limitarmi ed entusiasmandovi anche per quei piccoli successi che mi sembravano insufficienti. Grazie grazie grazie.

Infine, per ultima ma non meno importante (anzi), vorrei ringraziare Martina. Non sa che la sua presenza al mio fianco è stata essenziale per poter affrontare tutte le sfide e i problemi che ci sono stati durante questi tre anni, dal risolvere i piccoli problemi in laboratorio all'affrontare insieme una pandemia. Condividere con lei i momenti felici ed i successi li ha resi indubbiamente migliori e più memorabili. Non so esprimere a parole quanto sia grato per questa vita insieme, per cui mi limiterò ad un semplice "Grazie patata".

Contents

Introduction **1**

1 Single Photon emitters **5**
1.1 Statistics of light sources . . . 5
1.2 First and second order autocorrelation functions . . . 7
1.3 Optimal properties for single photon emitters . . . 10
1.4 State of the art single photon emitters . . . 12
1.5 Techniques to maximize the photon collection efficiency . . . 14

2 $GaAs_{1-x}N_x$ quantum dots and G-centers in silicon **17**
2.1 $GaAs_{1-x}N_x$ . . . 17
2.1.1 H effect on $GaAs_{1-x}N_x$ . . . 19
2.1.2 $GaAs_{1-x}N_x$ QDs as single photon emitters . . . 21
2.1.3 Strain control in $GaAs_{1-x}N_x$ . . . 25
2.2 G-centers in silicon . . . 26
2.2.1 Luminescent point defects . . . 26
2.2.2 Properties of the G-centers . . . 28
2.2.3 Fabrication of G-centers . . . 30
2.2.4 G-centers as single photon emitters . . . 31
2.2.5 Other technologies related to G-centers . . . 33

3 Experimental details **35**
3.1 Fabrication techniques and setups . . . 35
3.1.1 Molecular Beam Epitaxy . . . 35
3.1.2 Ions implantation . . . 37
3.1.3 Optical lithography . . . 38
3.1.4 Electron beam lithography . . . 39
3.1.5 $GaAs_{1-x}N_x$ QDs fabrication setup . . . 39
3.1.6 Plasma-enhanced chemical vapor deposition . . . 40
3.1.7 Rapid Thermal Processing . . . 41
3.1.8 $GaAs_{1-x}N_x$ QDs sample structure . . . 42
3.1.9 G-centers sample structure . . . 43
3.2 Characterization techniques and setups . . . 45
3.2.1 Micro-photoluminescence setup . . . 45
3.2.2 Ellipsometry . . . 47
3.2.3 Micro-Raman setup . . . 48

3.3 Simulation techniques and software 49
3.3.1 Finite-Difference Time Domain simulations 49
3.3.2 SMUTHI 50
3.3.3 Finite Element Method simulations 50
3.3.4 SRIM 51

4 $GaAs_{1-x}N_x$ Quantum Dots 53
4.1 The role of photonic jets in the QDs fabrication process 53
4.2 The characterization of the emitters 55
4.2.1 Identification of the QD emission lines 57
4.2.2 Time-resolved PL measurements 59
4.2.3 The second order autocorrelation function 60
4.2.4 Evaluation of the collection enhancement 62
4.3 Summary and future developments of the technique 68
4.3.1 Future developments 69

5 Engineer G-centers emission with strain 75
5.1 The samples structure 75
5.2 Samples characterization 76
5.2.1 Microphotoluminescence maps 78
5.2.2 FEM simulations 79
5.2.3 Analysis of the microphotoluminescence spectra 81
5.2.4 Time-resolved photoluminescence measurements 85
5.2.5 Polarization measurements 86
5.3 Summary and future developments 88

6 Conclusions and future perspectives 91

A $GaAs_{1-x}N_x$/GaAs quantum well 95

B Evaluation of the quantum dots diameter 97

C Second-order autocorrelation fitting model 99

Introduction

A single photon emitter (SPE) is a light source that emits one photon at a time in a pure quantum state. Ideally, this photon is identical, in all its properties, to all the others emitted by the SPE[1]. Moreover, the photons are emitted on demand, i.e. after an optical or electrical trigger of the source. Thanks to the possibility to control the quantum correlation of the emitted photons, SPEs represent the central building block of many Quantum Information Technologies (QIT)[2, 3, 4, 5, 6, 7]. In particular, the two more interesting applications are Quantum Cryptography[8, 9, 10] and Quantum Computing[7, 11, 12, 13]. The former relies on the law of quantum mechanics to exchange encrypted information between two users. In this framework, the generation of single photons is needed for the Quantum Key Distribution (QKD) process[14, 15, 10, 16], where the two users share a secret key to encrypt and decrypt messages. While in Quantum Computing SPEs would be used as sources for qubits (the quantum version of the classical bit) or quantum memories.

Among the years, several processes to generate single photons have been studied. Starting from the first demonstration of a SPE, performed with sodium atoms[17], cold atoms represent an efficient and reliable source of single photons with optimal optical properties[18, 19, 20]. However, they need complex setups to work, they are characterized by low operation rates and they cannot be easily implemented in integrated circuits. Alternatively, single photons can be generated by spontaneous parametric down-conversion[21, 22, 23](SPDC). In this approach a photon is converted into a couple of photons with lower energy thanks to a non-linear crystal. Therefore, detecting one of the two photons grants the presence of the other, these sources are indeed defined as "heralded SPE". This technique can also be used to realize entangled photon pairs[24]. Nonetheless, there are some issues: the spontaneous nature of process leads to a lack of control over the photon emission time, moreover SPDC is characterized by a poor single-photon purity and a reduced efficiency due to the many losses in the system. Even though the first issue has been solved by using multiplexing schemes, there is still much work to do to optimize this technique.

One of the most promising types of single-photon sources are solid-state SPEs[1, 25]. These emitters can be distinguished in two major groups: quantum dots (QDs) and point defects. The latter are defects in crystalline structure, e.g. vacancies, substitutional and/or intestitial atoms etc., which introduce one or more discrete energy levels within the band gap of the hosting material becoming able to absorb and emit light. The core of this group of SPEs was traditionally formed by the color centers in bulk crystals[26, 27, 28, 29] however, in the last few years, an increasing attention is dedicated to other defects-hosting materials such as carbon nanotubes[30] or 2D materials (e.g. hexagonal boron-nitride, hBN, or transition metal dichalcogenides, TMDC)[31, 32, 33]. On the other hand, a QD simply consists in a small volume (typically of the order of some hundreds nm^3) of semiconductor embedded in a material with an higher energy gap. As a consequence the QDs have an

atom-like energy levels structure due to the 3D confinement of the charges[34]. Therefore, both QDs and defect share the same outstanding optical properties of atoms while being embedded in an host material making them perfectly suitable for scalability.

Solid-state SPEs are bright sources which can be easily integrated in photonic circuits[35, 36] and some of them can even emit single-photons at room temperature[37, 38, 39]. However, being embedded in an host material entails some disadvantages including the linewidth homogeneous broadening due to the presence of unwanted defects, leading to photons distinghuishability, and a reduced photon collection extraction[40]. Indeed, especially when the surrounding material has an high refractive index, the photons emitted by the source are not able to exit from the host material due to total internal reflection. To solve this issue, several technologies have been proposed and are currently under study[41]. Some of them relies on coupling the SPE to a cavity mode[42, 43, 44, 45] or to a plasmonic field[46, 47], while others relies on different approaches such as reducing the total internal reflection and/or increasing the directionality of the emission[48, 49, 50, 51]. Regardless of their working mechanism, it is of utmost importance to investigate newer and better technologies to enhance light collection from solid-state SPEs to make them practically usable in all the different applications.

In the framework of identifying and studying novel SPEs to be employed in QIT, this work presents the characterization of two solid-state SPEs: isolated $GaAs_{1-x}N_x$ QDs, along with a technique to increase the emitted photon collection; ensembles of G-centers, whose emission was tuned by localized strain. G-centers are point defects in silicon made by two carbon atoms bound to an interstitial silicon atom. They have some interesting optical properties, such that their zero phonon line (ZPL), at low temperature (10 K), is peaked at around 0.969 eV (~ 1280 nm), perfectly within the so called telecom O-band of the optical fibers. This transmission band ranges between 1260 nm and 1360 nm and it includes both the ZPL and the phonon sideband of G-centeres. This is a relevant aspect since for the G-centers a huge fraction of the total emitted photoluminescence (~ 85 %) is contained within the phonon sideband[29]. Moreover, they are easy to realize, the broadening of their ZPL can be as small as 1 μeV (in ^{28}Si) and can be detected up to 110 K. On the other hand, even $GaAs_{1-x}N_x$ QDs are easy to realize, moreover their emission can be arbitrarily tuned both by controlling the nitrogen concentration in $GaAs_{1-x}N_x$ and/or by simply changing the QDs size. Considering that an increase in the N concentration leads to a reduction in the $GaAs_{1-x}N_x$ energy gap[52], a combination of the two effect can be exploited to fabricate $GaAs_{1-x}N_x$ QDs emitting in the same telecom O-band as the G-centers.

In particular, in this thesis work it will be presented the fabrication and characterization of samples containing these SPEs. The characterization was performed by means of low temperature (10 K) micro-photoluminescence, which was exploited to study the optical properties of the emitters. In addition to that, an innovative technique to fabricate $GaAs_{1-x}N_x$ will be described along with the results of a novel approach to tune the G-centers emission on a nanometic scale. The former represents a cheap, fast and easy alternative to realize $GaAs_{1-x}N_x$ QDs with the intrinsic advantage of increasing the photoluminescence collection of the fabricated emitters[48, 53]. On the other hand, the G-centers emission was locally tuned exploiting strained suspended membranes. It is worth noting that, to our knowledge, this is the first attempt to achieve this result with a micrometric device.

In details, this work will be divided in five chapters.

Chapter 1 will contain an introduction to SPEs, starting from the description of their photon statistics which let us distinguish between a SPEs and other light source. Then, their

most important properties will be described and related to the requirements that SPEs have to fulfill in order to be employed in QIT. In light of this, the state of the art SPEs with their properties will also be presented. Finally, the last part of the chapter will be dedicated to the light collection problems and the state of the art solutions to solve this issue.

Chapter 2 will focus on the two SPEs studied in this work. It will be divided in two parts, one for each SPE studied. Both parts will contain a description of the more important properties of the SPE presented, along with the state of the art technologies based on it.

Chapter 3 will be devoted to the description of all the experimental setups employed both in fabrication and in characterization processes, along with a brief description of the software employed for the various simulations presented. It will also contain the description of the samples employed in this thesis work.

Chapter 4 will contain all the experimental results from the measurements performed on $GaAs_{1-x}N_x$ QDs. In detail, the novel fabrication technique developed to laser-write $GaAs_{1-x}N_x$ QDs will be described, along with the characterization of the realized QDs. Moreover, the measurement of the PL collection enhancement obtained from the dielectric microspheres employed to fabricate the QDs will be shown. Lastly, the results of a set of simulation to carefully optimize this technique will be described.

Chapter 5 will focus on presenting the successful realization of a novel technique to tune the G-centers emission with strain.

The **Conclusions and future perspectives** chapter will summarize the most important results of this work with an eye to the possible future developments.

Chapter 1

Single Photon emitters

A single photon emitter (SPE) is a source able to generate wavepackets of light on demand, where each wavepacket contains exactly one photon in a pure quantum state. An example of SPE is an isolated two level system in the excited state which spontaneously return to the ground state emitting a photon. SPEs are non-classical light emitters that show some unique properties. To understand this, it is useful to compare the statistical properties of their light states with the ones of thermal light and coherent light. The parameter of interest to properly do so is the photon number fluctuation, which will be evaluated in the three cases and compared.

1.1 Statistics of light sources

Thermal light is the electromagnetic radiation resulting by the thermal equilibrium between absorption and emission of a radiation field and an ensemble of emitters[34]. In this system, the mean number of photons per pulse, $\langle n \rangle$, with frequency ω and at the temperature T is[54]:

$$\langle n \rangle = \frac{1}{e^{(\hbar\omega/k_B T)} + 1} \tag{1.1}$$

and the photon number probability $P(n)$, i.e. the probability of each pulse of containing n photons, can be written as:

$$P(n) = \frac{\langle n \rangle^n}{(1 + \langle n \rangle)^{n+1}}. \tag{1.2}$$

Since $n \geq 0$ by definition, it can be easily demonstrated that $P(n)$ is maximum for $n = 0$ and it decreases as n increases. Moreover, it is worth noting that the probability does not show any particular peak at $\langle n \rangle$ (see Figs.1.1a) and d)).

The variance of the distribution gives a statistical evaluation of the photon number fluctuation and can be evaluated as follows:

$$(\Delta n)^2 = \sum_n (n - \langle n \rangle)^2 P(n) = \langle n^2 \rangle - \langle n \rangle^2 = \langle n \rangle^2 + \langle n \rangle \tag{1.3}$$

where for the last equality it was exploited[1] that $\langle n(n-1) \rangle = 2\langle n \rangle^2$ and it directly leads to

[1]It derives from the property of $P(n)$ by which: $\langle n(n-1)(n-2)\ldots(n-r-1) \rangle = r!\langle n \rangle^r$, where r is any positive integer[54].

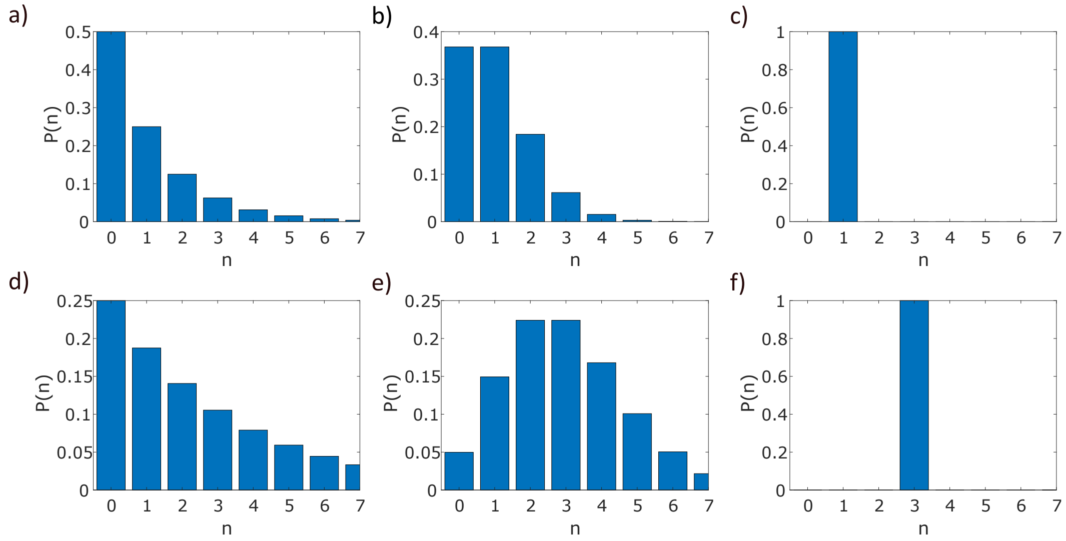

Figure 1.1. Photon statistics for different kind of lights. a) and d) Photon number probability for a thermal light source with $\langle n \rangle$ equals to 1 and 3, respectively. b) and e) Photon number probability for a coherent light source with $\langle n \rangle$ equals to 1 and 3, respectively. c) and f) Photon number probability for a Fock state with $\langle n \rangle$ equals to 1 and 3, respectively.

the fluctuation of the photon number:

$$\Delta n = \sqrt{\langle n \rangle^2 + \langle n \rangle} \tag{1.4}$$

From this expression of the fluctuation it is clear that for $\langle n \rangle \gg 1$ $\Delta n \approx \langle n \rangle$. Therefore the relative fluctuation of the photon number ($\Delta n / \langle n \rangle$) tends to a constant value increasing the photons number.

A light field is called coherent when there is a fixed phase relationship between its electromagnetic field values at different locations or times. The typical example of coherent light source is a laser. From the point of view of quantum mechanics, a coherent source generates Glauber states, also called coherent states, described by the ket $|\alpha\rangle$. In this state, the photon number distribution $P(n)$, i.e. the probability that the coherent state is occupied by n photons, is Poissonian and can be written as follows:

$$P(n) = e^{-\langle n \rangle} \frac{\langle n \rangle^n}{n!}. \tag{1.5}$$

This distribution is clearly peaked at $n = \langle n \rangle$ (see Figs.1.1b) and e)) and, being a Poissonian distribution, it is characterized by a variance of $(\Delta n)^2 = \langle n \rangle$ and thus $\Delta n = \sqrt{\langle n \rangle}$. In this case, the relative fluctuation of the mean photon number approach zero increasing the photon number.

A single photon source, on the other hand, generates only purely non-classical light states called Fock states, or photon number states. These states are described by the ket $|n\rangle$, where n is the number of photon in such state[2]. They are eigenvalues of the photon number operator $\hat{n}$, hence a mode excited in this state will be occupied by exactly n photons with fluctuation $\Delta n = 0$ (see Figs.1.1c) and f)).

[2]A single photon source will thus generates a $|1\rangle$ state.

It is clear that the statistics of these three light sources are profoundly different. Moreover, it is evident that a true SPE cannot be substituted by an attenuated thermal or coherent sources, even if the mean photon number of those sources would be $\langle n \rangle \approx 1$.

1.2 First and second order autocorrelation functions

It is now of interest to define a function which can be used to evaluate if a light source is a SPE. To do so, it is useful to recall the expression of the first and second order temporal autocorrelation functions. Considering an electric field $\mathbf{E}$ in stationary conditions and evaluated at time t and $t+\tau$ in the same spatial point, classically the first order coherence function is defined as:

$$g^{(1)}(\tau) = \frac{\langle \mathbf{E}^*(t)\mathbf{E}(t+\tau)\rangle}{\sqrt{\langle|\mathbf{E}(t)|^2\rangle\langle|\mathbf{E}(t+\tau)|^2\rangle}} \tag{1.6}$$

while the second order autocorrelation function is given by:

$$g^{(2)}(\tau) = \frac{\langle \mathbf{E}^*(t)\mathbf{E}^*(t+\tau)\mathbf{E}(t+\tau)\mathbf{E}(t)\rangle}{\langle \mathbf{E}(t)\mathbf{E}(t)\rangle^2} \tag{1.7}$$

where the operation $\langle \dots \rangle$ represents the average over time. From its definition it can be shown that classically: $g^{(2)}(\tau) = g^{(2)}(-\tau)$, $1 < g^{(2)}(0) < \infty$ and $g^{(2)}(\tau) < g^{(2)}(0)$.

To extend the definitions of $g^{(1)}(\tau)$ and $g^{(2)}(\tau)$ to quantum mechanics we need to recall the the quantization of the electric field:

$$\hat{\mathbf{E}}(\mathbf{r}) = \hat{\mathbf{E}}^{(-)}(\mathbf{r}) + \hat{\mathbf{E}}^{(+)}(\mathbf{r}) \quad \text{with} \quad \hat{\mathbf{E}}^{(-)}(\mathbf{r,t}) = i\sum_{\mathbf{k},\lambda}\sqrt{\frac{\hbar\omega_{\mathbf{k}}}{2\epsilon_0 V}}\epsilon_{\mathbf{k},\lambda}\hat{a}^\dagger_{\mathbf{k},\lambda}e^{i(\mathbf{k}\cdot\mathbf{r}-\omega_k t)} \tag{1.8}$$

where $\hat{a}^\dagger_{\mathbf{k},\lambda}$ is the creation operator of a photon with wavevector $\mathbf{k}$, wavelength λ and frequency $\omega_{\mathbf{k}}$ and $\hat{\mathbf{E}}^{(-)}(\mathbf{r})$ is the Hermitian conjugate of $\hat{\mathbf{E}}^{(+)}(\mathbf{r})$ and vice versa. Therefore, substituting Eq. 1.8 in Eqs. 1.6 and 1.7 results in:

$$g^{(1)}(\tau) = \frac{\left\langle \Psi \middle| \hat{a}^\dagger(t)\hat{a}(t+\tau) \middle| \Psi \right\rangle}{[\langle \Psi | \hat{a}^\dagger(t)\hat{a}(t) | \Psi\rangle \langle \Psi | \hat{a}^\dagger(t+\tau)\hat{a}(t+\tau) | \Psi\rangle]^{1/2}} \tag{1.9}$$

$$g^{(2)}(\tau) = \frac{\left\langle \Psi \middle| \hat{a}^\dagger(t)\hat{a}^\dagger(t+\tau)\hat{a}(t)\hat{a}(t+\tau) \middle| \Psi \right\rangle}{\langle \Psi | \hat{a}^\dagger(t)\hat{a}(t) | \Psi\rangle \langle \Psi | \hat{a}^\dagger(t+\tau)\hat{a}(t+\tau) | \Psi\rangle} \tag{1.10}$$

where $|\Psi\rangle$ is a pure state and all the constants are simply ignored for the sake of simplicity. The first and second order autocorrelations can be exploited to obtain information on the light source by measuring them with a Michelson interferometer[55] and a Hanbury-Brown and Twiss interferometer[56], respectively. For example, the probability of detecting a photon, ω_1, is directly connected to the absorption of such photon by a detector, thus ω_1 can be associated with a transition between an initial field state Ψ and possible final states Ψ_f, hence accordingly to the Fermi golden rule:

$$\omega_1(\tau) \sim \sum_f |\left\langle \Psi_f \middle| \hat{a}(t) \middle| \Psi \right\rangle|^2 = \left\langle \Psi \middle| \hat{a}(t)^\dagger \hat{a}(t) \middle| \Psi \right\rangle \tag{1.11}$$

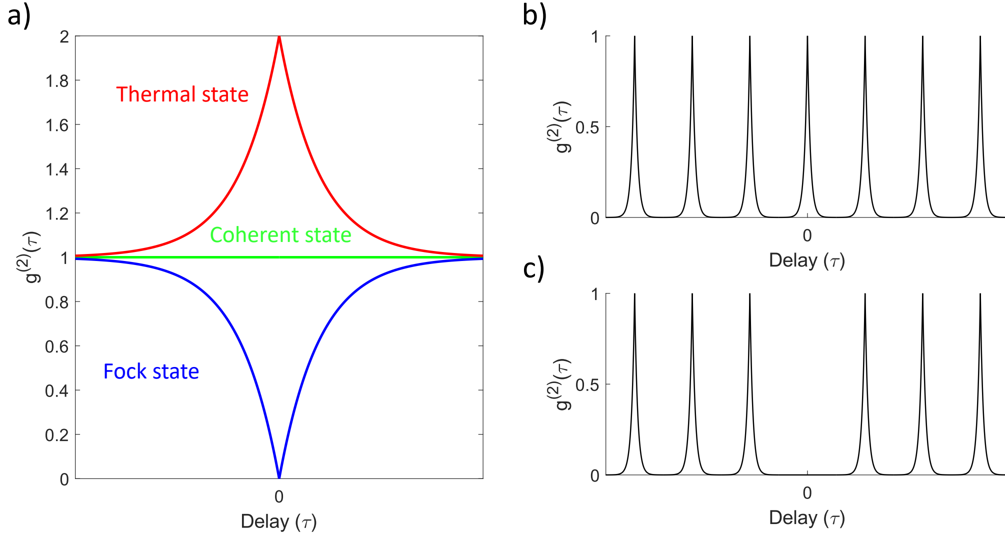

Figure 1.2. a) Second-order autocorrelation functions for the different kinds of light, distinguished by colour, under continuous wave excitation. b) and c) second-order autocorrelation function for a coherent light state and a Fock state, respectively, under pulsed excitation.

where it was exploited that $\sum_f |\Psi_f\rangle\langle\Psi_f| = 1$ and $\hat{a}(t)$ is the destruction operator of a photon at the time t. Therefore, comparing Eq. 1.11 and Eq. 1.9 results clear that the first order autocorrelation function is, apart from a scale factor, the photon detection probability and thus it is directly connected to the counting rate of the photodetector. However, it is worth noting that the $g^{(1)}(\tau)$ is insensitive to photon statistics since it only depends on the average photon number $\langle\hat{n}\rangle = \langle\hat{a}^\dagger\hat{a}\rangle$[3]. Therefore, thermal and coherent light will exhibit the same value of first order autocorrelation, provided that the thermal light is spectrally-filtered.

On the other hand the second-order autocorrelation function can be used to distinguish between different type of light fields. Indeed, its value at zero delay, i.e. $g^{(2)}(0)$, can be written as a function of the photon number fluctuation:

$$g^{(2)}(0) = 1 + \frac{(\Delta n)^2 - \hat{n}}{\langle\hat{n}\rangle^2}. \tag{1.12}$$

Therefore, for the three different light states results:

- Thermal light

$$g^{(2)}(0) = 1 + \frac{(\Delta n)^2 - \langle\hat{n}\rangle}{\langle\hat{n}\rangle^2} = 2 \tag{1.13}$$

  where the value of $(\Delta n)^2$ was obtained from Eq.1.3.

- Coherent state $|\alpha\rangle$ [4]

[3]Here a compact notation is used, where $\langle\Psi|\hat{n}|\Psi\rangle = \langle\hat{n}\rangle$, which is valid if $|\Psi\rangle$ is a pure state.

[4]The same result is obtained substituting the definition of coherent state into equation 1.12. Indeed, $|\alpha\rangle = e^{-\frac{|\alpha|^2}{2}}\sum_n \frac{\alpha^n}{\sqrt{n!}}|n\rangle$ where $|n\rangle$ is the Fock state, and it is an eigenstate of the annihilation operator with eigenvalue α, i.e. $\hat{a}|\alpha\rangle = \alpha|\alpha\rangle$ and $\langle\alpha|\hat{a}^\dagger = \langle\alpha|\alpha^*$. Therefore equation 1.12 becomes: $g^{(2)}(0) = \frac{\langle\alpha|\hat{a}^\dagger\hat{a}^\dagger\hat{a}\hat{a}|\alpha\rangle}{(\langle\alpha|\hat{a}^\dagger\hat{a}|\alpha\rangle)^2} = 1$.

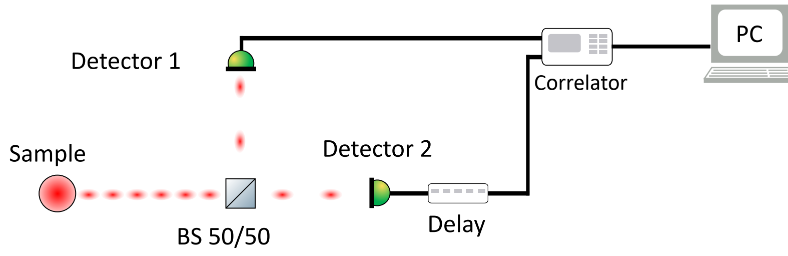

Figure 1.3. Scheme of a Hanbury-Brown and Twiss interferometer[56].

$$g^{(2)}(0) = 1 + \frac{(\Delta n)^2 - \langle \hat{n} \rangle}{\langle \hat{n} \rangle^2} = 1 \tag{1.14}$$

where we have exploited that $(\Delta n)^2 = \langle \hat{n} \rangle$, for a coherent state.

- Fock state $|n\rangle$

$$g^{(2)}(0) = 1 + \frac{(\Delta n)^2 - \langle \hat{n} \rangle}{\langle \hat{n} \rangle^2} = 1 - \frac{1}{\langle \hat{n} \rangle} \tag{1.15}$$

where we have exploited that $(\Delta n)^2 = 0$, for a Fock state. This state is clearly a nonclassical state of light since it gives $g^{(2)}(0) < 1$ for $n \geq 1$, while classically $1 < g^{(2)}(0) < \infty$. Moreover, it is worth noting that, for a single photon source, $g^{(2)}(0) = 0$.

Therefore the value of the second order autocorrelation function for $\tau = 0$ is a clear indicator of the kind of source under investigation (see e.g. Fig. 1.2a). The complete calculation of $g^{(2)}(\tau)$ can be performed for all the three different light states[54] and its most important properties are the following. For a *Poissonian* light state, i.e. a coherent state, $g^{(2)}(\tau) = 1$, hence the photons are completely uncorrelated. Instead, for a *Super Poissonian* light state, i.e. thermal light, $1 \leq g^{(2)}(\tau) \leq 2$ for $\tau < T$, where T is the coherence time of the source, with a maximum for $\tau = 0$. This phenomenon is called *photon bunching*. On the other hand, a Fock state follows a *sub-Poissonian* statistics[5], i.e. it satisfies $g^{(2)}(\tau) \leq 1$ with $\tau < T$ and with a minimum for $\tau = 0$. This phenomenon is called *photon antibuching*. In particular, an ideal SPE will have $g^{(2)}(0) = 0$.

So far all the calculations and the results are presented under a continuous wave excitation of the source. Under pulsed excitation conditions the second order autocorrelation function consists in a series of peaks separated by the source repetition period. If the source is a coherent source, all the peak areas will be identical. While, with a single photon source, the pulse centered at $\tau = 0$ will be absent, see Figs.1.2b) and c).

Regardless of the excitation type, the second order autocorrelation function can be measured using an Hanbury-Brown and Twiss interferometer. This interferometer consists in a 50/50 beam splitter combined with two identical detectors as shown in Fig. 1.3. The signals measured by the two detectors are correlated and plotted as a function of the time delay τ between them, thus resulting in a direct evaluation of the $g^{(2)}(\tau)$. As said before, if the source is a SPE the $g^{(2)}(\tau) \leq 1$ with a minimum for $\tau = 0$ and, in particular, $g^{(2)}(0) = 0$ for an ideal SPE. Indeed, an ideal SPE emits only a photon at a time, hence it is impossible

[5]Another example of a light state which follows the same statistics is a coherent squeezed states[57].

Table 1.1. Requirements to use the SPEs in different Quantum Information applications[1]

Application	**Photon purity,** $g^{(2)}(0)$	**Indistinguishability**	**Photons emission rate**
Quantum Key Distribution	< 0.1	Not strictly required	>GHz
Cluster-state Quantum Computing	< 0.001	> 0.99	Ideally GHz
All-optical quantum repeater	< 0.001	> 0.99	> GHz
Bell-state sources for memory-based repeaters	< 0.01	> 0.9	Ideally GHz

for the detectors to measure simultaneously a photon each. More in detail, the value of $g^{(2)}(0)$ represents the fraction of the emitted wavepackets containing more than one photon and thus it represents an indication of the single photon purity of the source. Therefore, not being ideal, the sources under investigations will inevitably show a $g^{(2)}(0)$ bigger than zero. To this end, when examining a source a threshold has been introduced to distinguished if it is a SPE or not, namely a source is a SPE if $g^{(2)}(0) < 0.5$, i.e. more than 50% of the emitted wavepackets contain a single photon.

In literature the single photon purity of SPE is reported or as a percentage (of the packages containing single photons) or, as in this work, simply as the value of the $g^{(2)}(0)$. It represents one of the most important properties used to determine if a SPE can be used in a specific application or not, as it will be explained shortly.

1.3 Optimal properties for single photon emitters

As previously said, an ideal SPE emits, on demand, one photon at a time, indistinguishable from all the other emitted photons, with an efficiency of 100%. This summarize the three most important properties of a SPE: the single photon purity, the indistinguishability of the photons, and the brightness of the source.

The single photon purity represents the ability of the source of emitting only one photon per pulse. As said before, it can be tested by measuring the second order autocorrelation function. In particular, different QIT require different degrees of single photon purity, i.e. a value of the $g^{(2)}(0)$ smaller than a certain threshold. In Table 1.1 are presented some of these application with the corresponding requirements. As it can be seen, a high single photon purity is always required (the higher the better) especially in quantum computing applications[58], where it reduce the amount of errors[59, 60], and in quantum communications, where the SPEs can be used as quantum repeaters[61].

Photons indistinguishability is an important requirement in many different applications, for example in single photon interferometry or in the realization of two-photon quantum logic gates[62]. Indeed, the two photons interaction can be obtained exploiting the quantum interference of two indistinguishable photons. The photon indistinguishability can be measured through the Hong-Ou-Mandel experiment[63], which is sketched in Fig. 1.4. Here, two indistinguishable photons, in the same pure quantum state, are sent to the two inputs of a beam splitter. If the photons arrive simultaneously in the beam splitter a quantum interference process takes place and the probabilities of having both photons reflected or transmitted interfere destructively. As a result, the two photons exit from the same output of

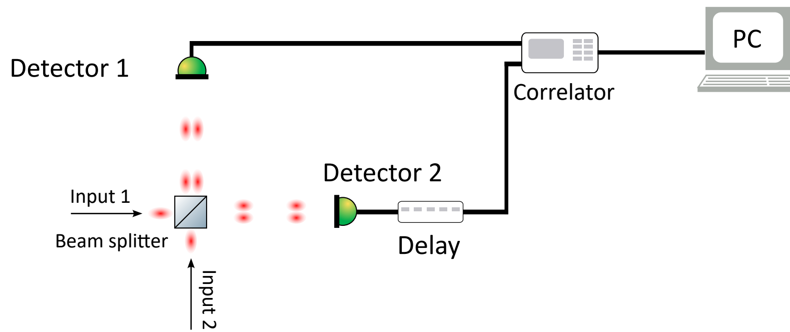

Figure 1.4. Sketch of the Hong-Ou-Mandel experiment.

the beam splitter. Of course, increasing the degree of distinguishability of the two photons will reduce the quantum interference leading to an increase in the probability of having them exiting from different outputs.

A parameter to measure the degree of indistinguishability is the visibility of the quantum interference V_{HOM}. To measure that, the signals from the two detectors are correlated and the second-order correlation function is obtained in two scenarios: when the two photons are maximally indistinguishable, and the resulting function is called $C_{||}$, and when the two are maximally distinguishable, obtaining a function called $C_{\perp}$. The latter measurement is performed, e.g., delaying the arrival time of one of the two photons or changing its polarization. The visibility normalized is then: $V_{HOM} = (C_{\perp} - C_{||})/C_{\perp}$[41]. The indistinguishability M is directly linked to V_{HOM} by: $M = V_{HOM}((R^2 + T^2)/2RT)$, where T and R are the beam splitter intensity transmission and reflectivity coefficients, respectively. Therefore, employing a 50/50 beam splitter leads to $M = V_{HOM}$. An ideal SPE will be characterized by $V_{HOM} = 1$ while a source with $g^{(2)}(0) > 0$ will have $V_{HOM} < 1$. Sometimes, instead of the indistinguishability M, M^* is reported, which is simply the indistinguishability corrected by the value of the $g^{(2)}(0)$. M^* characterizes the photons wavepackets overlap for all degrees of freedom other than the photon number, and it is given by: $M^* = M + g^{(2)}(0)$. However, for quantum optics and QIT applications M is the relevant parameter.

Similarly to single photon purity, a high indistinguishability is required in most applications, as schematized in Table 1.1. Indeed, increasing the indistinguishability leads to an optimization in the photon interference which is at the basis of those applications. Typically an indistinguishability bigger than 0.9 is required. However, for some applications such as QKD, this requirement can be relaxed. That said, obtaining truly indistinguishable photons remain one of the challenges concerning SPEs.

Lastly, there is the brightness of the SPEs to be taken into account. Up to now there is not an universally recognized definition of the SPEs brightness. In theory the definition should take into account the source internal and external efficiencies, the amount of photon emitted by the source per unit time and the probability of detect those photons. A good parameter that summarize all of this is the rate of photons emitted from the SPE impinging on the first lens or in general on the first collection element. This value can be calculated by measuring the source intensity on the detector and dividing it for the efficiency of the various optical elements in the setup.

An elevated photon rate give rise to faster and more reliable operations both in Quantum Cryptography[64] and Quantum Computing[65], to this end most QIT require a photon

Table 1.2. State of the art SPEs with some of their more relevant properties[7]. In the table there are some abbreviations: NW - nanowire, WG - waveguide, µC - micropillar cavity, DBR - distributed Bragg reflector, BG - Bragg grating, NPA - nano-patch antenna.

Emitter	Photon purity, $g^{(2)}(0)$	Indistinguishability	Photon emission rate on first lens
GaAs QD combined with BG[66]	0.001[1]	~ 0.9	~ 45 MHz
GaAs QD combined with DBR[67]	0.002[1]	0.93	~ 150 kHz
InGaAs QD in WG[68]	< 0.006[1]	0.94	~ 1 MHz
InAs QD in NW[45]	< 0.008	Not measured	~ 55 MHz
InGaAs QD in µC[42]	0.0028[1]	0.9956	~ 50 MHz
InGaAs QD in WG[69]	0.009[1]	0.975	~ 500 kHz
SPDC[70]	Not measured	0.962	~ 7.2 MHz/W
SPDC[24]	Not measured	0.91	~ 12 MHz/W
NV^- center combined with NPA[71]	0.41[2]	Not measured	~ 240 MHz
NV^- center combined with SIL[72]	0.16[2]	Not measured	~ 57 MHz

[1] Measured under quasi-resonant or resonant excitation
[2] Measured at room temperature

rate of the order of GHz to work properly (see Table 1.1)[6]. Unfortunately, the state of the art SPEs are not able to reach such emission rates. One of the aspects causing this issue is the reduced collection efficiency of the system. This problem is well known in the community and the researchers keep studying and developing new and more efficient techniques to maximize the emitted photon collection without affecting the purity or the indistinguishability of the sources. To this end, after presenting some of the state of the art SPEs, a description of these techniques will be presented, along with their advantages and disadvantages.

1.4 State of the art single photon emitters

In light of the three properties described before we now review some SPEs that represent the state of the art. These emitters are summarized in Table 1.2 along with their properties.

As we can see, the state of the art is mainly represented by solid-state SPEs in combination with different techniques to enhance the photon collection. In particular, self-assembled GaAs an InGaAs QDs represent the best solution in terms of the highest single photon purity and indistinguishability. The former are realized by droplet epitaxy on a substrate containing a low reflectivity back reflector. With this technique highly symmetric QDs are realized. The structural symmetry of the emitters leads to a reduced fine structure splitting of the exciton level thus resulting in a large degree of entanglement between photons emitted by the QDs[67]. Moreover, in order to increase the light collection and decrease the radiative decay time exploiting Purcell effect, on top of these QDs was realized a circular Bragg

[6] It is worth mentioning that, when employing a source with an elevated photon emission rate, a potential source of limitation could be the detector. Indeed, it has to be selected with the proper maximum rate count to not limit the system performances.

[7] It is worth mentioning that, along with the ones described in the table, other important properties of SPEs are their emission wavelength, their operating temperature, and the deterministic generation of such SPEs.

resonator[66]. These QDs have shown the best results in terms of photon purity and they show promising properties for future developments.

On the other hand, Stranksi-Krastanov InGaAs QDs represent the standard choice for QD photonics. Indeed, they are undoubtedly the most used and optimized QDs for quantum optics experiments. This appears clearly from the optimal quality of their emission. Indeed, they show a photon purity higher than 99% (i.e. $g^{(2)}(0) < 0.01$) with an indistinguishability above 0.94. The best results are achieved by InGaAs QDs embedded in a microcavity. The microcavity was realized with an advanced in situ lithography technique which consists in the following steps. A layer containing self-assembled QDs is grown by molecular beam epitaxy at the center of a vertical microcavity surrounded by two Bragg mirrors. Then, the planar cavity is spin-coated with a photoresist. After measuring the low temperature photoluminescence of the QDs to localize the best ones, the photoresist surrounding such dots was exposed with a laser beam and later removed to obtaining circular holes centered on the dots (for more detail on the working principle and steps of optical lithography processes see Chapter 3.1.3). As a final step, the microcavities were realized through chloride reactive ion etching. This process leads to a spatial precision in centering the QD of about 50 nm while the cavity resonance can be adjusted with a spectral accuracy of about 0.5 nm. In this configuration and under resonant excitation an indistinguishability of ~ 0.996 is measured, which represent, to our knowledge, the best result achieved so far. In addition to that, the presence of the microcavity leads to a measured brightness of about 50 MHz, which is an excellent value for QDs but it is far from the required brightness needed for QITs (see Table 1.1).

A part from QDs, an elevated single photon rate can be obtained from NV centers and Spontaneous Parametric Down-Conversion (SPDC). Regarding the latter sources, the brightness is directly connected to the laser power employed to achieve the down-conversion. However, there is an important drawback: increasing the laser power results in reducing the fidelity of the two photons entanglement and the indistinguishability due to the introduction of noise[24]. For example, the reported indistinguishability of 0.91 from Ref.[24] is obtained with a low power (44 mW) laser beam, while increasing the power to 1 W this value is reduced to 0.76.

On the other hand, NV^- centers in diamonds are bright sources that show a promising photon purity. However, their intense brightness is typically measured integrating over a broad energy range. Indeed, the PL of these defects is typically collected employing long and short pass filters to be able to collect both the zero phonon line (ZPL) and the phonon sidebands of the emission, cutting out the laser signal. Therefore, to use them in most QIT applications we would need to filter their emission, to not worsen the indistinguishability, thus leading to a drastic reduction of the brightness. However, it is worth mentioning that both NV^- centers and SPDC work at room temperature, drastically simplifying the setups employed and making their use in QIT a lot more appealing.

It results clear that the only thing withholding the state of the art SPEs to be actively employed in QIT is their brightness. Indeed, their photon purity and indistinguishability already surpass the minimum values required to actively use them. To this end, several solution have been proposed to increase the luminescence collection and some of them are already used (see Table 1). We will now describe a selection of such techniques, along with a novel technique that we have recently developed. However, it is worth mentioning that additional studies must be performed to fully implement QIT based on SPEs.

Table 1.3. State of the art techniques to enhance the luminescence collection of single photon emitters (mainly quantum dots) with their main characteristics. Several of these approaches include a back-reflector. Also in the microsphere approach the QW/air back interface acts as a non-optimal back-reflector. The value of the collection efficiency is reported considering a collection optical system with a numerical aperture (NA) of 0.7. The collection efficiency of the microspheres was calculated considering that the system without the microsphere has a nominal collection efficiency of 2%.

Technique	**Required spatial alignment**	**Required spectral matching**	**Collection efficiency** (NA = 0.7)	**Lithography required?**
Microspheres (this work)	Self-aligned	Broadband (≈ 200 nm)	≈ 14%	No
Fabry-Pérot microcavities [73]	Tunable	Broadband	8.6%	Yes
Photonic trumpets [50]	≈ 20 nm	Broadband	95%	Yes
Nanowires [45]	≈ 20 nm	Broadband (≈ 70 nm)	72%	Yes
3D printed microlenses [49]	34 nm	Broadband	23%	Yes
Gold rings [74]	≈ 50 nm	Broadband (≈ 70 nm)	≈ 15%	Yes
Photonic Crystal Cavities [44]	< 50 nm	≈ 2.5 nm	≈ 44%	Yes
3D printed Bragg gratings [75]	50 − 250 nm	≈ 70 nm	48%	Yes
Micropillar cavities [42]	50 nm	0.5 nm	64%	Yes

1.5 Techniques to maximize the photon collection efficiency

Table 1.2 clearly shows that solid-state SPEs are the most promising sources for the implementation of QIT. However they are held back by their limited emission intensity. As said in the introduction, this is mainly due to the presence of a solid-state environment, which has a large refractive index and thus strongly limits the extracted luminescence due to total internal reflection. Indeed, for example, the fraction of the total power emitted by a dipole, embedded in a planar material with refractive index $n = 3.5$, and transmitted in air is between the 0.06% and the 2.1%, depending on the dipole axis orientation[40]. Therefore, it is clear that even if a SPE would emit enough intensity to fulfill the requirements needed in most of the QIT ($\sim 10^9$ photons/s) only a minimal fraction of this intensity could be concretely used. Moreover, the numerical aperture (NA) of the collecting optics limits the collected luminescence even further. This issue not only affects the amount of light collected but can also lead to a change in the measured emission statistics. Indeed, even if the QD emits exactly one photon during each excitation cycle, the system is not really deterministic: the photon counts per second (N) will, in fact, follow a binomial distribution, $f(N; N_0, p)$, where N_0 is the number of excitations per second and p is the photon collection probability (Fano factor = $1 - p \approx 1$).

To do so, several solutions have been proposed throughout the years and the more relevant ones are summarized in Table 1.3 (see also Fig. 1.5). In the following we will briefly present them, focusing the attention on the ones involving QDs. It is worth noting that some of these techniques can be employed with other solid-state SPEs as well, as long as the proper materials are employed.

Among these solutions[35], the ones that give the best results rely on the enhance-

ment of the collected luminescence thanks to a coupling between the QDs emission and the mode of an external resonator. Therefore, to maximally exploit this effect a hardly achievable spatial and spectral coupling between the two is needed. The external resonator can be a microcavity[76, 73], a photonic crystal (PhC) cavity alone[44] or coupled with a waveguide[43], or a circular Bragg grating[75]. The spectral coupling problem have been partially solved thanks to the development of broadband alternatives such as gold rings[74], 3D printed microlenses[49, 77, 78], nanowires[45], nanorings alone[46, 74] or combined with other broadband solutions[47], and photonic trumpets (with 95% out-coupling record efficiency)[50]. Nevertheless, these devices still require an accurate positioning of the QDs. A successful attempt to solve both issues at the same time has been performed by the implementation of the highly advanced in situ lithographic technique described previously[79, 42]. However, this approach, and all the others presented so far, requiring complex nano-fabrications and/or nano-manipulations, are not suitable for the scalability of the process. Moreover, they are irreversible, expensive and subject to possible failure in the nanofabrication process.

A second kind of solutions, albeit characterized by generally lower performances, is largely exempt from these drawbacks, since the desired collection efficiency enhancement is obtained by placing a millimeter lens, a spherical cap, called *solid immersion lens* (SIL), on the sample, on top of the emitters[51, 80]. It is a spectrally and spatially tolerant tool, which can be easily and reversibly placed on the sample. Its main drawback is represented by the relatively small enhancement a SIL can achieve: indeed, it can only increase the NA of the system by a factor equals to its refractive index, n_{L}, and thus its collection enhancement is about n_{L}^2[81]. However, a SIL can also be combined with other broadband solutions to further increase the collection enhancement[82, 47], yet reintroducing the problem of realising complex nano-fabrications and/or nano-manipulations. Finally, other SIL drawbacks include their bulky nature (mm-size), which is not ideal for many applications, and their sensitivity to the air-gap which can arise between them and the sample surface[81].

In this work, we propose an innovative method for the hybrid integration of a dielectric antenna on top of a buried QD, which gives a broadband, reversible, and low-cost solution to the light collection problem, by exploiting dielectric microspheres for creating self-aligned QDs. Indeed, it is known that the presence of a microsphere near of an emitters helps the collection process[83, 84] due to an increase in the NA of the system, and lately this has been verified also for QDs[85]. The main drawback of this approach is the requirement of a precise positioning of the microsphere on top of the QD, with an accuracy one order of magnitude smaller than the microsphere size itself; plus, a QD position even slightly off-axis leads the luminescence to be directed at a non-normal angle with respect to the sample surface[85]. We circumvented this issue by exploiting the microspheres not only for the collection process, but also for the QD fabrication, as it will be described in details in Chapter 4. The presence of the microsphere leads to an enhancement in the collection efficiency of a factor 7.3 ± 0.7. This value is obtained from the ratio between the intensity of the photoluminescence of a QD at saturation before and after the removal of the microsphere on top of it (see Chapter 4 for more details). We also demonstrate that this enhancement is mostly connected to an increase of the directionality of the QD emission.

It is worth noting that, albeit working in a similar fashion as the SILs, the microspheres increase in the luminescence collection strongly exceed the predicted enhancement of n_L^2. Indeed, the microsphere employed were made of mere silica (SiO_2) which refractive index, at the QD emitting wavelength, is about $n_L = 1.45$, therefore the predicted collection

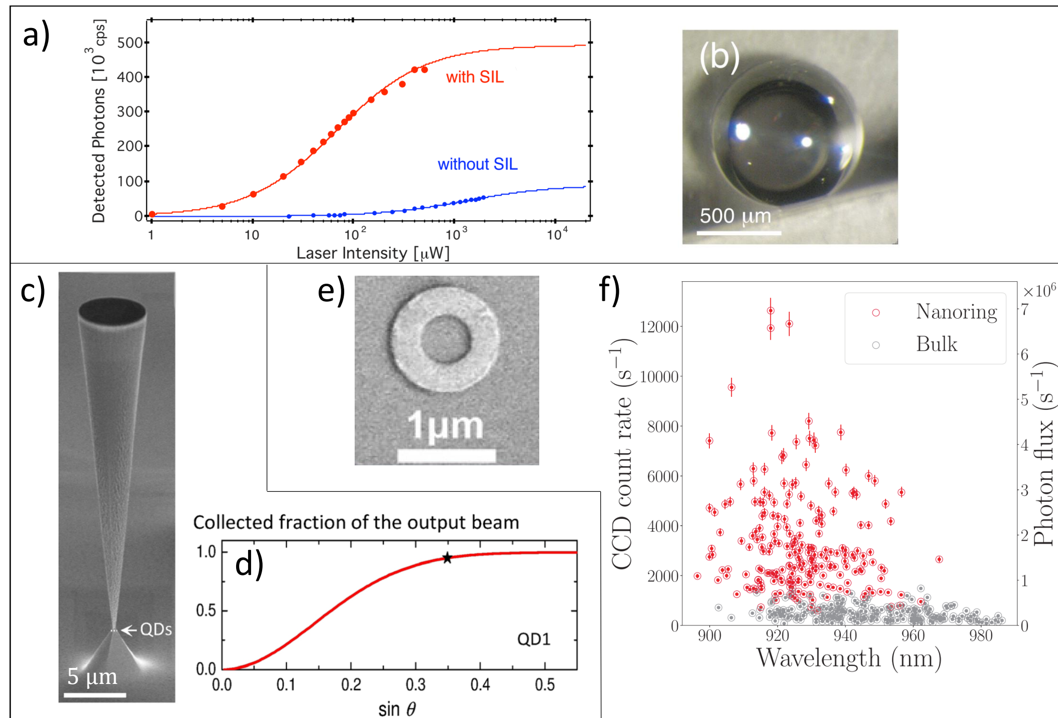

Figure 1.5. The three panels in which the Figure is divided represent three different collection enhancement techniques. a) PL intensity as a function of power of an NV center with and without a SIL on top of it. b) Photo of the the diamond SIL placed on top of the NV center[80]. c) SEM (Scanning Electron Microscope) image of a photonic trumpet. d) Plot of the collected fraction of the beam intensity as a function of NA (red curve), the star marks a collected fraction of 95%[50]. e) SEM image of a metallic nano-ring placed on top of a QD. f) PL intensity of various QDs within (red symbols) and outside (gray symbols) metallic nano-rings, plotted as a function of emission wavelength[74].

enhancement would have been about 2. The only other "geometrical" approach that shows similar (or sometimes better) results is the microlens. However, to do so, it is not enough to employ high refractive index materials (e.g. GaAs) but also to shape the microlens in particular geometries[78]. In addition to that there are all the fabrication issues previously described i.e. the need of nanolithography and a precise positioning of the microlens on top of the emitter. Therefore, the microsphere represent a cheap, broadband, and efficient solution to the luminescence collection issue which can be easily employed with many other SPEs.

Chapter 2

$GaAs_{1-x}N_x$ quantum dots and G-centers in silicon

In this chapter the main properties of the two single photon emitters studied will be presented. Firstly the more relevant characteristics of $GaAs_{1-x}N_x$ will be described, along with the effect that H has on this material. Then the state of the art of technologies based on $GaAs_{1-x}N_x$ will be shown. In the second part, the attention will focus on the G-centers, in particular on their structure, their relevant optical properties and their formation processes. Lastly, the state of the art technologies based on G-centers will be presented.

2.1 $GaAs_{1-x}N_x$

Dilute nitride semiconductors are alloys made from semiconductors of the *III* and *V* group in which a small percentage of N (usually less than 5%) is introduced in the *V*-group sublattice[52]. Even with such a small amount of N it is possible to strongly modify the properties of the materials[86]. For example, N introduction within GaAs reduce the band gap (E_g(GaAs) = 1.519 eV at 10 K) of about 0.15 eV every percent of N[87]. This is an unusual behaviour for a ternary alloy, which can be understood considering the empirical law that describes the energy gap of a ternary alloy $AB_{1-x}C_x$, as a function of the concentration of element C, x:

$$E_g = E_g^{AC}(1-x) + E_g^{BC}x - b(1-x)x \tag{2.1}$$

where E_g^{AC} and E_g^{BC} are the energy gaps of the compounds AC and BC, respectively, and b is the so called *optical bowing* parameter. This parameter embodies the unusual behaviour of dilute nitrides in terms of energy gap. Indeed, for alloys containing elements from the *III* and *V* group b has a constant value of the order of 1 eV[88], while in $GaAs_{1-x}N_x$ it is extraordinary large (up to tens of eV) and composition dependent[88, 89, 90]. This unusual behaviour can be exploited to realize high quality emitters in the telecom O-band (1260 − 1360 nm) by simply controlling the N percentage within $GaAs_{1-x}N_x$[91]. This is one of the properties that makes $GaAs_{1-x}N_x$ one of the most promising and extensively studied dilute nitride.

Despite the clear experimental evidences, the researchers struggled at first to find a clear theoretical explanation to $GaAs_{1-x}N_x$ energetic behaviour. However, after some years

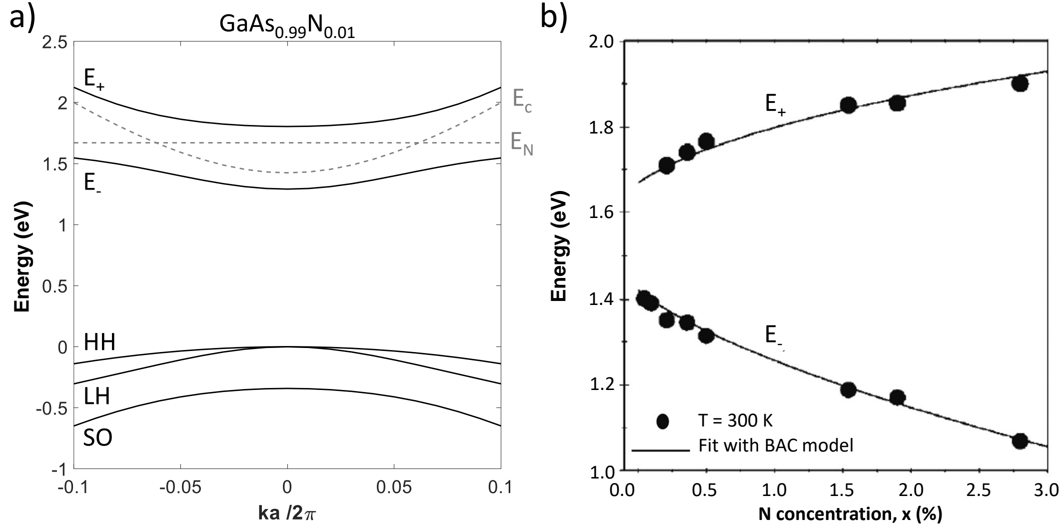

Figure 2.1. a) Electronic band structure for $GaAs_{0.99}N_{0.01}$, obtained with a $k \cdot p$ model[93] and considering the results of Eq.2.3 using the values: $E_N = 1.67\,\text{eV}$ and $V_{Nc} = 2.5\sqrt{x}$, with x representing the fraction of N atoms. b) E_+ and E_- data obtained by fitting photoreflectance spectra of $GaAs_{1-x}N_x$. The solid lines are the fit to the BAC model adapted form Ref.[92].

they successfully developed a simple model, called the Band-Anticrossing (BAC) model, to schematize this behaviour. The BAC model consists in describing the effects linked to the presence of N atoms in $GaAs_{1-x}N_x$ as the results of the interaction between two energy levels: one at energy E_N, which is the energy level introduced by the presence of a susbtitutional N defect in GaAs, and the other one at energy E_c, which is the energy of the extended conduction band of GaAs. Considering the interaction between the two states as a perturbation, it is possible to obtain the following eigenvalues problem:

$$\begin{vmatrix} E_N - E & V_{Nc} \\ V_{Nc} & E_c - E \end{vmatrix} = 0 \tag{2.2}$$

where V_{Nc} is the matrix element describing the interaction, and it is possible to show that it is connected to the N concentration, x, by the equation: $V_{Nc} = \beta\sqrt{x}$. From the resolution of equation 2.2 it is possible to obtain two different eigenvalues, E_- and E_+:

$$E_\pm = \frac{E_c + E_N}{2} \pm \sqrt{\left(\frac{E_N - E_c}{2}\right)^2 + V_{Nc}^2} \tag{2.3}$$

where the lower one, E_-, represents the conduction band dispersion curve of $GaAs_{1-x}N_x$, while the second eigenvalue, E_+, gives a resonant energy level that can be observed in photoreflectance measurements[92]. Indeed, in Fig. 2.1b are reported the results of such measurements fitted with Eq. 2.2 (as a function of the N concentration) with a very good agreement. Moreover in Fig. 2.1a is represented the theoretical band structure accordingly to the BAC model.

Despite the good agreement between the BAC model and some experimental results (e.g. the refractive index[94]), the model fails to explain others, e.g. the composition dependence of the effective mass of the conduction band edge[95] or the behaviour of the electron gyromagnetic ratio[96]. The inconsistencies between the model and the measurements arise

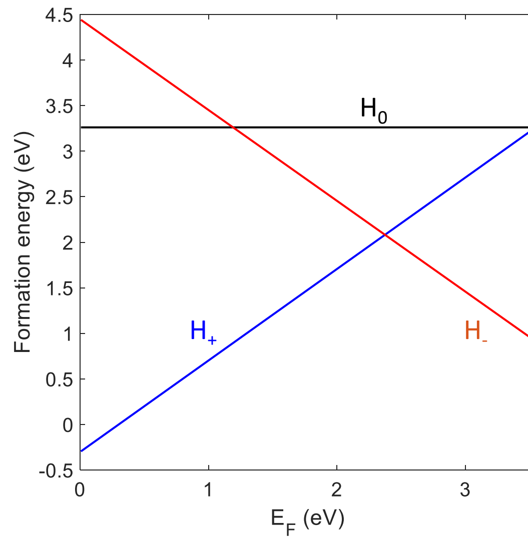

Figure 2.2. Theoretical formation energies of interstitial H in GaN in different charge states, referenced to the energy of a H_2 molecule. The zero of the Fermi energy is at the valence band minimum[98].

from considering only isolated N atoms within $GaAs_{1-x}N_x$. Indeed, several simulations show that increasing the nitrogen concentration in $GaAs_{1-x}N_x$ results in the formation of couples and even clusters of atoms, whose energy levels are necessarily different from the one of isolated N. Moreover, these energy levels become progressively more relevant as the N concentration increases. Therefore, knowing the proper statistical distribution of N within $GaAs_{1-x}N_x$ is of the utmost importance to adapt the model to a real scenario. This yields to a modification of the interacting term V_{Nc}, to take into account all the possible interactions between the GaAs conduction band and the newly formed energy levels, weighted by their intensity. This optimization of the model fill the gaps in the BAC model leading to a very good agreement between theory and experiments, see e.g. Fig. 5 of Ref. [97].

2.1.1 H effect on $GaAs_{1-x}N_x$

Hydrogen (H) is one of most diffused element on the Earth and the most diffused one in the Universe[99], hence H is an extremely common impurity during the growth and processing of semiconductor materials. Therefore, H in semiconductors has been extensively studied among the years. From these studies, interstitial H is predicted to be amphoteric, which means that it can act either as a donor or an acceptor in most semiconductors[98]. Moreover, it typically counteracts the prevailing conductivity, acting a donor in *p*-type semiconductors and as acceptor in *n*-type semiconductors. This behaviour is well described by the calculations performed on the formation energies of interstitial H, an example of which is reported in Fig. 2.2, where is shown that in a *p*-type GaN the H^+ formation is energetically favored and the same goes for the H^- in the *n*-type GaN, as expected. In addition to that, thanks to its high chemical reactivity and its diffusivity, H tends to bind to dangling bonds associated with point and extended defects (see e.g. Ref. [100]), thus mitigating their detrimental effects in the material, e.g. canceling the energy levels introduced in the band gap of the semiconductor. A famous example of this is amorphous silicon, which

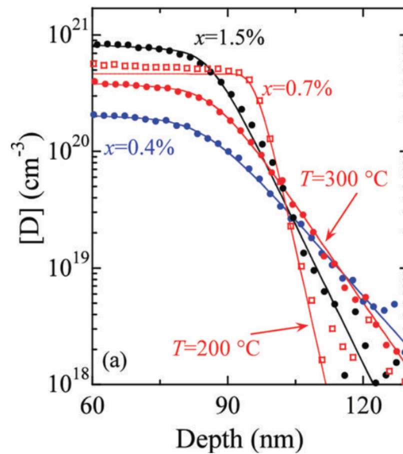

Figure 2.3. Secondary Ions Mass Spectroscopy (SIMS) depth profiles of deuterium for $GaAs_{1-x}N_x$ samples with different x (each color refers to the labeled concentration), along with the simulated profiles (solid lines). For $x = 0.7\%$ the two depth profiles refers to two different irradiation temperatures.[52]

started to be employed as an active material for silicon solar cells after the development of its defects passivation process via hydrogen[101, 102].

The introduction of hydrogen into $GaAs_{1-x}N_x$ has some interesting and unusual effects. H tends to bond with N to form two stable (up until 315℃ and 235℃, respectively) complexes , N-2H and N-2H-H[52, 103], leading to the elimination of all nitrogen effects. Indeed, increasing H concentration results in the gradual restoring of the bandgap, effective mass, spin properties, refractive index, lattice constant, and ordering of the N-free material[52, 104]. Therefore, once fully hydrogenated, $GaAs_{1-x}N_x$ shows strong similarities with GaAs, to the point that for some aspects they can be considered equal. For the sake of simplicity, from now the term $GaAs_{1-x}N_x$:H will be used when referring to the fully hydrogenated $GaAs_{1-x}N_x$.

Once discover the interesting effect of H in $GaAs_{1-x}N_x$, the next step was to try to control it. To achieve this, H diffusion process in $GaAs_{1-x}N_x$ was studied both from a theoretical and experimental point of view[52, 104, 105]. The results of these studies can be resumed in two main points: i) H diffusion mechanism is mediated by multiple trapping processes, which lead to the formation of the stable complexes described before, and ii) H depth profile is characterized by a plateau followed by a steep exponential decay (see Fig. 2.3). While the first result is not a novelty, the second one is quite interesting. Indeed, the exceptionally sharp H forefront (up to 5 nm/decade with $x = 0.7\%$ and $T = 200$ ℃) suggests that the H penetration depth can accurately control, hence H can be used to tailor the optical properties of $GaAs_{1-x}N_x$ on a scale of few of nanometers. It is worth mentioning that the SIMS measurements have been performed using H_2, which has a lower diffusion coefficient respect to H, and thus it results in a sharper profile. Nevertheless, this have only a limited effect thus still guaranteeing a submicrometer control over the hydrogenated areas.

Once verified the possibility to selectively hydrogenate $GaAs_{1-x}N_x$, the following question might be if is it possible to selectively remove it. A viable way could be with thermal annealing[52], however it is quite difficult to carefully control it, especially at the nanoscale. Alternatively, it was find out that these bonds can also be broken by shining

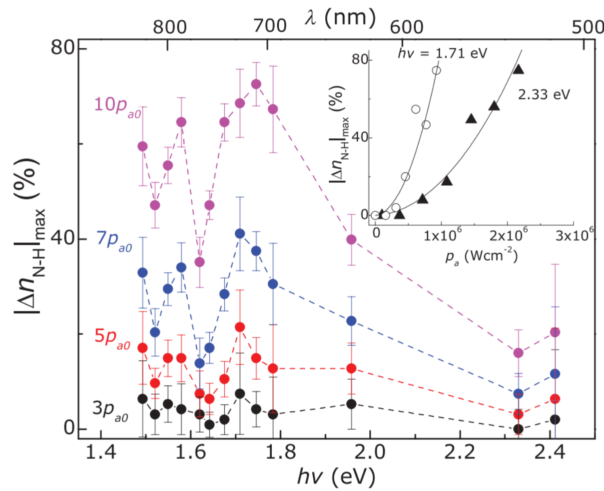

Figure 2.4. Dependence of the maximum percentage of N-H bonds broken ($|\Delta n_{\mathrm{N-H}}|_{\mathrm{max}}$) on the photon energy $h\nu$ and laser wavelength λ for various power densities, p_a ($p_{a0} = 10^5$ Wcm^{-2}). The inset shows the dependence of $|\Delta n_{\mathrm{N-H}}|_{\mathrm{max}}$ on p_a at $h\nu = 1.71$ and 2.33 eV ($\lambda = 725$ and 532 nm).

the $GaAs_{1-x}N_x$:H with a laser light of proper wavelength[106]. In Fig. 2.4 is reported the percentage of N-H bonds broken as a function of the energy. Looking at the curves in the plot, it is clear that there are two energies around which the effect is more intense: 1.77 eV and 1.57 eV. They are connected to the dissociation energy of the N-H compounds where the first one is perfectly coherent with the reported value [107], while the second one suggests the presence of a lower energy bound for the dissociation of the N-2H complex by the formation of a closely related complex state with a lower activation energy [108]. Despite matching these energies will result in breaking the N-H bonds in the most efficient way, the process is quite broadband (around 900 meV), therefore a different energy can be employed provided that a higher power is employed. Indeed, from the inset of Fig. 2.4 it is clear that, by simply increasing the power of a factor 2, out of resonance excitation leads to similar result of in resonance excitation. Moreover, increasing the power can be of advantage since, to properly recover $GaAs_{1-x}N_x$ from $GaAs_{1-x}N_x$:H, breaking the N-H bonds is not enough, H atoms must be taken away to prevent the reformation of the complexes. This can be achieved by locally increasing the temperature above the H outgassing value ($T_a > 250$ °C)[106]. Therefore, an increase in the excitation power will result in an increase in the local temperature facilitating the H outgassing.

These two approaches to locally control the H concentration within $GaAs_{1-x}N_x$, along with the striking effects linked to H, represent excellent tools to tailor the material optical properties at the nanoscale.

2.1.2 $GaAs_{1-x}N_x$ QDs as single photon emitters

Among the years several techniques have been realized to fabricate $GaAs_{1-x}N_x$ QDs, in order to exploit them as SPEs in QIT. In this section we will review the most important ones.

The first technique concerns the fabrication of site-controlled $GaAs_{1-x}N_x$ QDs[109] (top panel of Fig. 2.5) by locally control the hydrogen diffusion. The realization process is

based on the fact that $GaAs_{1-x}N_x$:H has the same energy gap of GaAs, as previously said. Therefore, having a small volume of $GaAs_{1-x}N_x$ surrounded by GaAs and/or $GaAs_{1-x}N_x$:H would results in having a 3D energy confinement for the charges and thus a QD. This is achieved by depositing circular titanium masks on top of a GaAs/$GaAs_{1-x}N_x$ QW which is then hydrogenated. The masks presence prevents H to fully hydrogenate all the $GaAs_{1-x}N_x$ area below it thus resulting in having small $GaAs_{1-x}N_x$ regions (in axis with the masks) surrounded by higher energy gap materials ($GaAs_{1-x}N_x$:H on the sides and GaAs on top and below) and hence a QD (see Fig. 2.5b). The QDs fabricated with this technique show good optical properties and their single photon emission nature was successfully tested. This approach represents a reliable way to fabricate site-controlled QDs, which can be employed for the fabrication of highly uniform arrays of QDs (see Fig. 2.5d). Moreover, thanks to the high alignment precision of the electron beam lithography (EBL) system used to realize the titanium masks (about 20 nm), this technique can be used to fabricate $GaAs_{1-x}N_x$ within a photonic structure to enhance the PL efficiency. An example of this is reported in the bottom panel of Fig. 2.5, where the PL characterization of a QD realized with this technique and embedded in a photonic crystal (PhC) cavity is shown[110, 111]. The fabricated QD shows a $g^{(2)}(0) < 0.5$ proving the SPE nature of the emitter. Moreover, it exhibits a promising weak coupling with the cavity leading to an enhancement in the PL intensity. These preliminary results can be used as a starting point for future developments, e.g. aiming to obtain a strong coupling between the QD and the cavity.

Other fabrication techniques are based on locally removing of H from $GaAs_{1-x}N_x$:H by shining the material with a laser light of proper wavelength. This effect can be exploited to fabricate $GaAs_{1-x}N_x$ QDs with a similar approach to the one just described. The idea is to start from a GaAs/$GaAs_{1-x}N_x$ QW, to fully hydrogenate it and then shine some areas to break the N-H bonds and remove the hydrogen atoms, thus obtaining the $GaAs_{1-x}N_x$ QDs. However, the formation of a QDs requires that the H removal process takes place only in limited areas, hence it is of utmost importance to minimize and control the illumination spot size. To this purpose several techniques have been developed among the years and the most recent one is part of this work and will be described in details in Chapter 4. We will now briefly review two of those techniques employed to reduce and control the laser spot size, thus obtaining $GaAs_{1-x}N_x$ QDs.

The first technique relies on the ability of bowtie nanoapertures to localize the electromagnetic field on a sub-wavelength scale thanks to a surface plasmon resonance. In particular, these nanoapertures were obtained by EBL in an aluminum thin layer deposited on top of a GaAs/$GaAs_{1-x}N_x$:H QW[112, 113]. The geometrical properties of these apertures were carefully chosen to present: a plasmonic resonance at around 700 nm, i.e. the best wavelength to break the N-H bonds; to obtain a strong field enhancement, to remove H atoms; and to obtain a reduced spot waist at the center of the QW. It is worth mentioning that in the best configuration the spot waist is about 80 nm, well below the diffraction limit. Once fabricated the nanoapertures with the optimal characteristics, they were shined with a laser light with $\lambda_l = 700$ nm with different powers. To do a comparison, some unpatterned areas were also shined. Then, the PL of the sample was measured both at room and low temperature (T= 300 K and 5 K, respectively). From the spectra at room temperature showed in Fig. 2.6b, it is clear that outside the apertures the light had no effects while within them the H removal process was successful. Moreover, the low temperature spectra show some narrow lines (linewidth ≈ 1 nm) which are undoubtedly evidence of quantum confinement and strongly suggests the presence of a $GaAs_{1-x}N_x$ QDs below the aperture. Therefore,

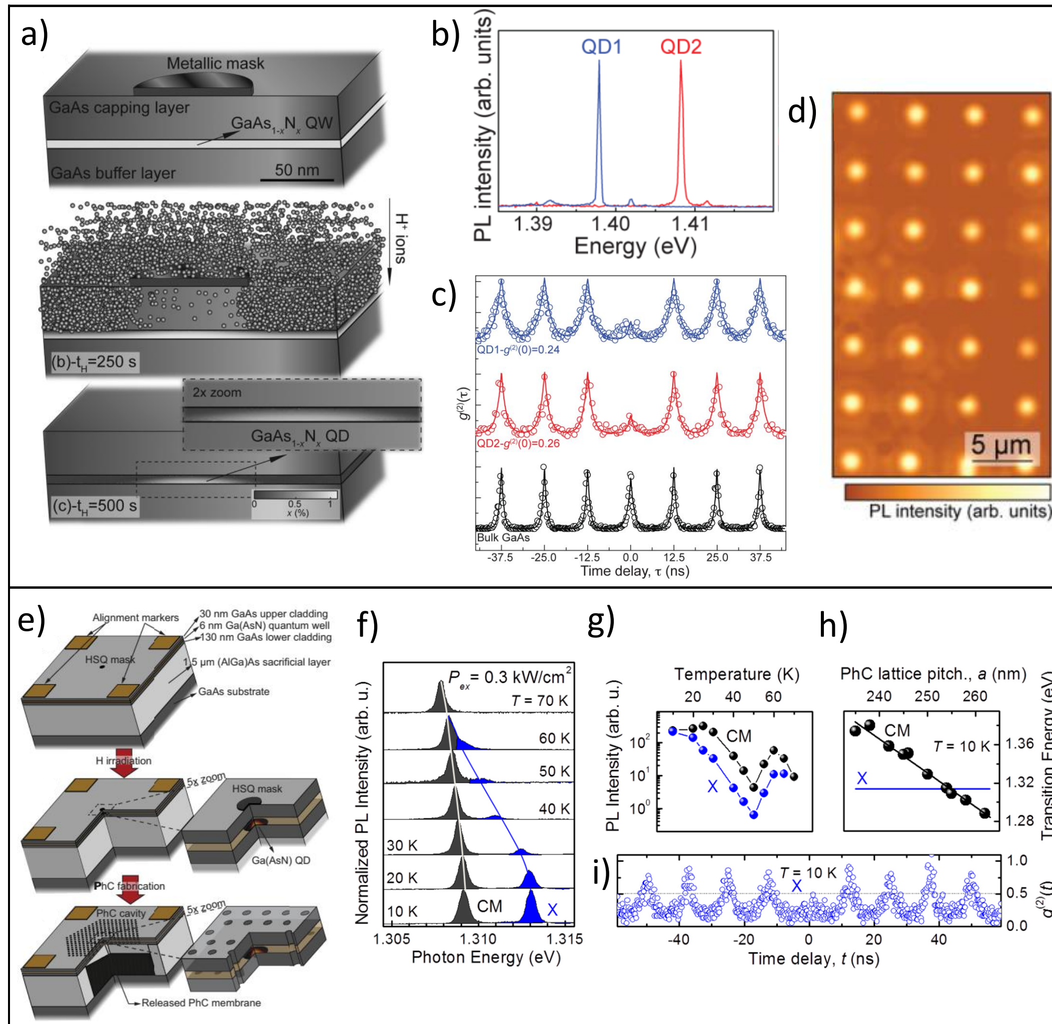

Figure 2.5. The two panels contains the results of the QD fabrication technique that relies on the controlled hydrogenation of $GaAs_{1-x}N_x$, as described in the text, and its implementation in combination with a PhC cavity. a) Steps of the $GaAs_{1-x}N_x$ QDs fabrication process. b) Low temperature micro photoluminescence (micro-PL) spectra of two fabricated $GaAs_{1-x}N_x$ QDs. c) Normalized second-order autocorrelation function for the emission of two different QDs along with the one from GaAs, plotted as a reference. Both the QDs exhibit a value of the $g^{(2)}(\tau) < 0.5$ showing their single-photon emitter nature[109]. d) Low temperature intensity map of a QD array, acquired by using a long pass filter to reject emission from GaAs, $GaAs_{1-x}N_x$:H and laser reflection. e) Sketch of the fabrication steps required for the deterministic integration of a single $GaAs_{1-x}N_x$ QD with a PhC cavity. The presence of the alignemenet markers ensure a near-perfect alignemenet (~ 20 nm) between the QD and the center of the cavity. f) Normalized micro-PL measurements of the exciton transition of the QD (X) and the cavity mode (CM) at different temperatures. g) Temperature dependence of the integrated PL intensity of the CM (black dots) and of the X peak (blue dots). The intensity increase observed for temperatures above 50 K is a result of the Purcell effect, due to the QD coming into resonance with the CM. h) Lithographic tuning of the CM energy of a PhC L3 defect cavity (r/a = 0.29) by varying the PhC lattice pitch value, *a*. i) Second-order autocorrelation of the X peak for a site-controlled QD embedded in a PhC cavity. Note the $g^{(2)}(0) < 0.5$, providing evidence of the SPE nature of the QD integrated in the PhC cavity[110, 111].

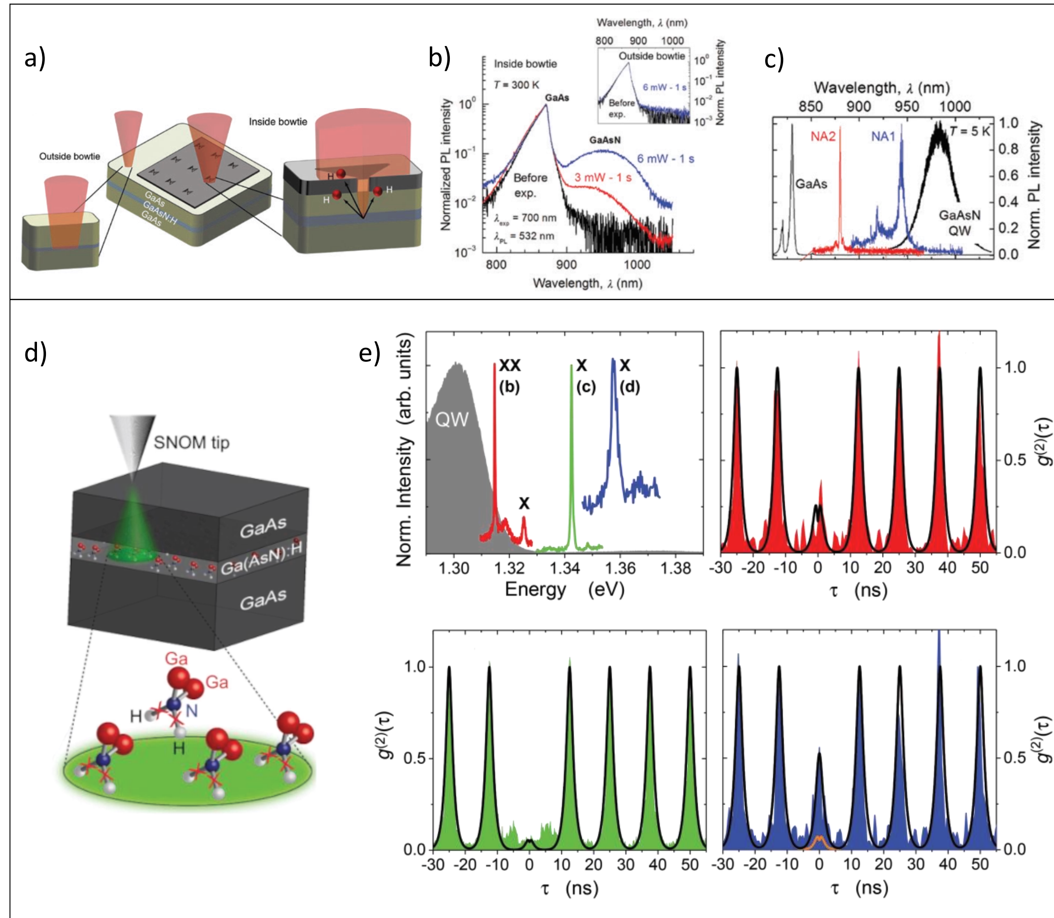

Figure 2.6. Each panel contains the plots associated with one of the two different techniques for the controlled removal of H in $GaAs_{1-x}N_x$:H discussed in the text. a) Sketch of the plasmon-assisted H removal in a GaAs/$GaAs_{1-x}N_x$:H QW exploiting the bowtie nanoapertures. b) Room temperature micro-PL spectra measured before and after illuminating a bowtie aperture with a laser light with power 3 mW (red) and 6 mW (blue). Inset: room temperature micro-PL spectra pre and post illuminating an unpatterned area. c) Low temperature micro-PL spectra measured in two different nanoapertures (NA1 and NA2), after treating them with two different laser powers (6 mW and 3 mW, respectively). The GaAs and the QW spectra are also reported for comparison. d) Sketch of the H removal process employing the SNOM system. e) Low temperature micro-PL spectra of three different QDs, distinguished by colour, along with the corresponding second-order correlation measurements, coloured accordingly. The labels X and XX indicate the exciton and biexciton emission, respectively. The black curves in the $g^{(2)}(\tau)$ plots corresponds to the fit of the curves, the orange curve in the last plot represents the fit of the $g^{(2)}(\tau)$ measurements taking into account a classically correlated background.

these bowtie nanoapertures can successfully be used to fabricate site-controlled $GaAs_{1-x}N_x$ QDs with the only positioning limit represented by the spatial resolution of the EBL (20 nm).

A different approach to localize the electromagnetic field is with the use of a Scanning Near-field Optical Microscopy (SNOM) system[114]. A SNOM system employs an etched optical fiber tip to collect the samples PL. Moreover, coupling the fiber with a laser it can be used in an excitation-collection configuration. Thanks to an electrical feedback system, the tip is held at about 10 nm from the sample surface. This short distance allows to collect the evanescent waves of the emitted electromagnetic field, thus resulting in a spatial resolution limited only by the diameter of the fiber aperture[115]. Therefore, employing an etched tip results in strongly limiting the excited area. Due to this it is possible to fabricate $GaAs_{1-x}N_x$ QDs by simply shining a GaAs/$GaAs_{1-x}N_x$:H QW with a laser light through the SNOM tip[116]. The main results of this approach are presented in Fig. 2.6e, where the low temperature PL of the fabricated QDs is presented, along with the $g^{(2)}(\tau)$ measurement to verify their single-photon emitter nature. The different PL spectra are obtained from QDs of different sizes realized by simply changing the laser power. As the previous approach, the SNOM system can be used to fabricate site-controlled $GaAs_{1-x}N_x$ QDs. Indeed, the SNOM tip can be moved within the sample with a spatial resolution of about 50 nm. The main drawback of this technique is that the SNOM system is a complex and expensive setup, therefore a large scale fabrication of QDs with this approach is not feasible. However, it leads to the fabrication of QDs of almost arbitrary size with good optical properties and without the need of any lithographic processing of the material.

In conclusions, several fabrication techniques have been developed to fabricate $GaAs_{1-x}N_x$ QDs, all based on the striking effect that H has on this material. Some of these techniques lead also to the fabrication of site-controlled QDs with promising optical properties. Relying on a similar approach, we have developed a novel technique to fabricate $GaAs_{1-x}N_x$ QDs that will be described later on in this work. All these efforts show promising results that will potentially lead to an active implementation of such QDs in QIT. Moreover, it is worth noting they all these techniques can be potentially applied to all those material that show similarities with $GaAs_{1-x}N_x$ and $GaAs_{1-x}N_x$:H.

2.1.3 Strain control in $GaAs_{1-x}N_x$

As a final remark we present an interesting technology, based on the properties of $GaAs_{1-x}N_x$, which leads to the control of light polarization through the realization of $GaAs_{1-x}N_x$/-$GaAs_{1-x}N_x$:H heterostructures[117, 113], see Fig. 2.7. These structures are obtained as follows. Firstly, a 50 nm thick titanium layer is deposited on top of a sample containing a 200 nm thick layer of $GaAs_{1-x}N_x$ (x = 0.4% and 0.9%) on a GaAs substrate. Then, the titanium layer is patterned by electron beam lithography to obtain wires of different lateral sizes (0.5, 1, 2, 5 and 10 µm, 5 µm apart). After, the sample is fully hydrogenated. Lastly, the titanium masks are removed. Thanks to the H diffusion behaviour (see previous section), the presence of the masks grants steep $GaAs_{1-x}N_x$/$GaAs_{1-x}N_x$:H interfaces, thus forming the heterostructures.

The presence of $GaAs_{1-x}N_x$ wires can be clearly observed measuring the PL of the samples employing a long pass filter to cut out the $GaAs_{1-x}N_x$:H and GaAs signals, see Fig. 2.7). Moreover, we can observe that the PL signal is polarized (up to 40%) along the direction perpendicular to the wires, see Fig. 2.7a. Therefore, changing the wires orientation would lead to a change in the polarization direction. This control is achieved thanks to

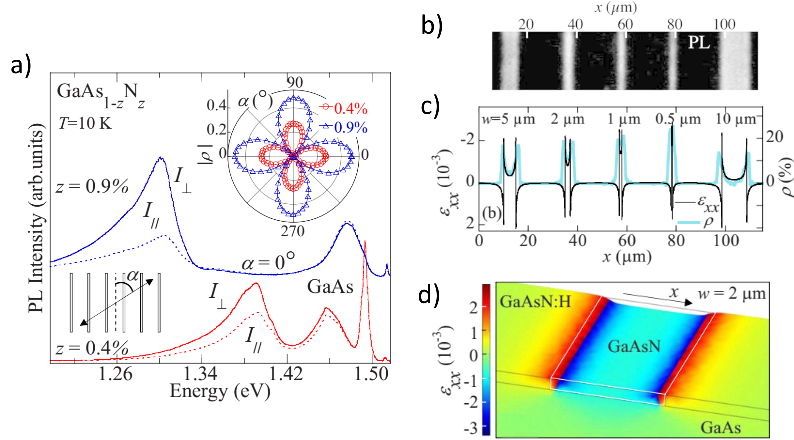

Figure 2.7. a) Low temperature micro-PL spectra on the wires. The blue (red) curves are for the $GaAs_{1-x}N_x$ wires with $x = 0.9\%$ ($x = 0.4\%$), where the continuous (dashed) one is the spectrum for a polarization orthogonal (parallel) to the wires. Bottom inset: scheme of the sample pattering where α is the angle between the polarizer and the wire axis. Top inset: polarization measurements results, where the degree of polarization $\rho = I_{\perp}/I_{\parallel}$ is reported as a function of α. b) Low temperature PL map of the wires, where the signal from $GaAs_{1-x}N_x$:H is rejected using a long pass filter. c) Polarization plot (cyan curve) and simulated strain plot (black curve), calculated along the direction perpendicular to the wires axis, across the wires. Note that the axis of the strain is reversed since in the $GaAs_{1-x}N_x$ are a tensile strain is present and hence the strain assumes negative values. A clear correlation between the two is present. d) Strain map calculated along the direction perpendicular to the axis of a $GaAs_{0.991}N_{0.009}$ wire with width= 2 μm embedded in fully hydrogenated $GaAs_{0.991}N_{0.009}$[117, 113].

the difference in the lattice parameter between $GaAs_{1-x}N_x$ and $GaAs_{1-x}N_x$:H. Indeed, $GaAs_{1-x}N_x$ is characterized by an intrinsic tensile strain, connected to the introduction of N in the GaAs matrix, which is then relaxed by the introduction of H (see Figs. 2.5c) and d)). This difference leads to a modulation in the strain within the heterostructure and thus to the emission of polarized light.

The local control over the hydrogen diffusion leads to a strongly localized manipulation of the strain fields. Strain control is a powerful and versatile tool that can be employed to tune the optical material properties in a non invasive way (see e.g. Ref.[118]), as we will also see related to G-centers later on in this thesis work (Chapter 5).

2.2 G-centers in silicon

2.2.1 Luminescent point defects

Silicon is the cornerstone element for electronics and photovoltaic industries, which usage keeps increasing every year, for example in 2020 the global silicon production amounted of about $8 \cdot 10^6$ metric tons[1]. Together with the spreading of silicon-based technologies, the refinement processes is steadily optimized, indeed the purity of electronic grade silicon can reach 99.9999999%, with a residual concentration of impurities of about $\rho_I \approx 5 \cdot 10^{13}\ \mathrm{cm}^{-3}$.

[1]Data based on the United States Geological Survey 2021 `https://pubs.usgs.gov/periodicals/mcs2021/mcs2021-silicon.pdf`.

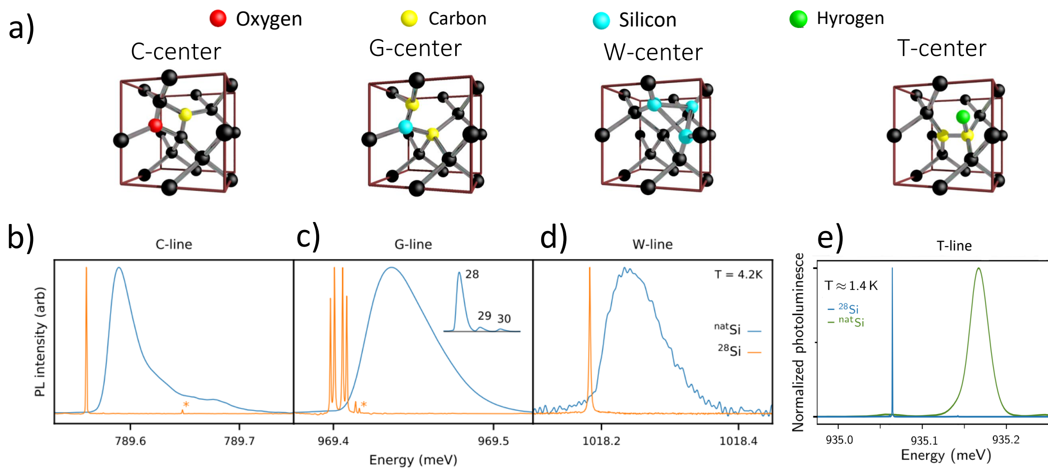

Figure 2.8. a) Crystalline structure of some point defects. From left to right: C-center, G-center, W-center and T-center. b)-e) Low temperature PL spectra of the corresponding point defects both in natural Si and in isotopically purified ^{28}Si[127, 130].

In addition to that, the realization of photonic devices based on Si is a well-established technology[119]. All these aspects made the use of silicon in QIT highly entrancing. To this end, remarkable advances in the field of silicon Quantum Computing have been made: from the demonstration of two-qubit gate fidelity above 99%[120, 121, 122], to the CMOS-based cryogenic control of quantum circuit[123] and to the fabrication of silicon qubits in a 300 mm semiconductor manufacturing facility using all-optical lithography and fully industrial processing[124]. However, the silicon is strongly limited to the non optical-based QITs, since it has the major drawback of having an indirect bandgap (E_g = 1.12 eV at room temperature), thus it is not characterized by an efficient photoluminescence. This issue can be circumvented by exploiting extrinsic and intrinsic emitting impurities that originates form rare-earth atoms[125], hydrogen[126], oxygen[127], carbon[29] etc.[128], embedded within the silicon matrix. These emitters are commonly known as radiation-damage centers as they are usually created via high-energy electron irradiation or directly by ion implant. They can be created in bulk Si as well as in silicon on insulator (SOI), another attractive platform for the fabrication of electronic and photonic devices (such as integrated photonic circuits). The list of the light emitting centers in silicon is extremely long[129] and most of them are well known, however most studies were focused on ways of eliminating them in order to achieve high purity silicon. Despite this, some of them have drew the attention of the researchers for their interesting properties.

In Fig. 2.8 the crystalline structure of the more interesting point defects in silicon is shown, along with a low temperature PL spectrum of their emission. As it is expected, their emission energy is below the energy gap of silicon (E_g = 1.12 eV at room temperature) and indeed, they all emit in the near infrared spectrum range. For example, the W-center, a defect formed by a cluster of three self-interstitial silicon atoms[131], emits at around 1215 nm. The C-center, on the other hand, is formed by an interstitial carbon atom and an interstitial oxygen atom[132] and its emission is centered at around 1570 nm, slightly outside one of the most used transmission band for the optical fibers, the C-band (1530 – 1565 nm). While the emission of the T-center, composed of two substitutional carbon atoms[133], is centered within the so called original band or O-band (1260 – 1360 nm). All these defects

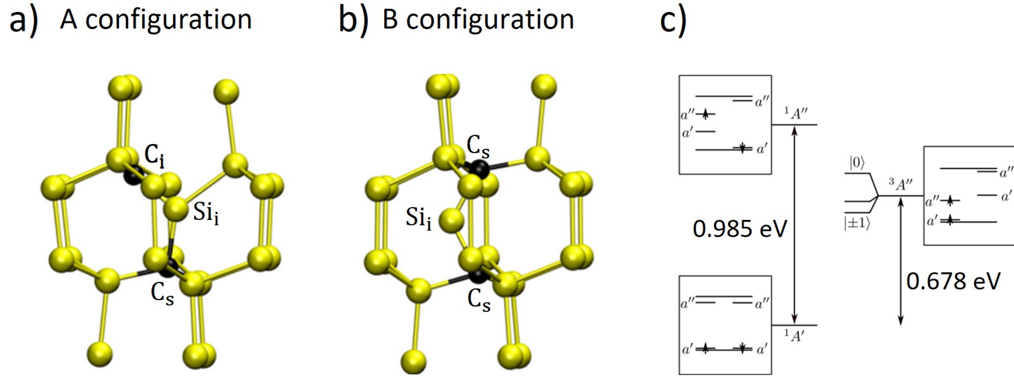

Figure 2.9. a) Structure of the stable A configuration $C_iSi_i{-}C_s$. b) Structure of the stable B configuration $C_s{-}Si_i{-}C_s$. c) Scheme of the electronic levels in the configuration B[134].

are promising sources for single photons to be employed in QIT. However the emission energy is basically the sole information we have on these luminescent defects in silicon, with few notable exception, one of which is G-centers.

2.2.2 Properties of the G-centers

The G-center is a bistable point defect formed by two carbon atoms and an interstitial silicon atom. The fact that it is a bistable defect means that it can exist in two stable atomic configurations, referred to as A and B. In configuration A the G-center consists of a carbon-silicon split-interstitial pair (meaning that they share the same lattice site) and a neighboring substitutional carbon atom. Using the common nomenclature for defects, configuration A is described as C_iSi_i-C_s. While in configuration B, the two carbon atoms are substitutional and the silicon atom is in interstitial position between them (C_s-Si_i-C_s)[134]. Configuration A is the stable configuration when the defect is charged (±1), while configuration B is the stable one when the defect is neutral. A sketch of these configuration is shown in Fig. 2.9. Despite both configuration are stable, only in configuration B the G-center is optically active and it is able to emits, with a ZPL centered at about 0.969 eV (see Fig. 2.8c). This is theoretically confirmed by density functional theory calculations which provide the expected electronic levels configuration. As sketched in Fig. 2.9c, the ground state is $^1A'$ with two possible excited states $^1A''$ and $^3A''$. The energy difference of the two transitions $^1A'' \longrightarrow {}^1A'$ and $^3A'' \longrightarrow {}^1A'$ are 0.985 eV and 0.678 eV, respectively. Therefore the former transition is in good agreement with what is observed in photoluminescence experiments.

Knowing the structure of the defects let us theorize if and how the photoluminescence signal of the G-centers is polarized. Indeed, taking into account configuration B and the possible atomic bonds, there are 12 different orientation of the G-centers, meaning that their emission is polarized along 12 different directions. However, typically the photoluminescence is collected along a specific crystalline direction, therefore the measurable polarizations are only the ones perpendicular to that direction, e.g. [100] and [010] if the luminescence is observed along the [001] direction.

From the experimental measurements performed on these emitters some other information can be extracted. First of all, there is the second-order autocorrelation function, which has been measured independently by three different groups[136, 29, 137, 138]. The

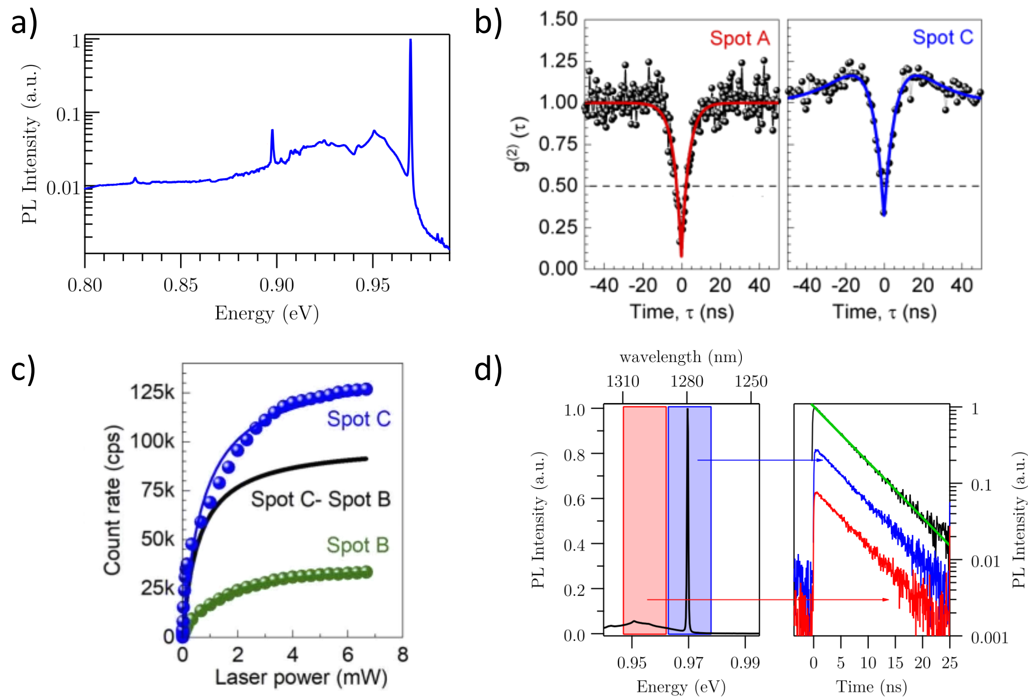

Figure 2.10. a) Low temperature spectrum of an ensemble of G-centers[135]. b) $g^{(2)}(\tau)$ measurements of two different G-center (scatter plots) along with the corresponding fit (continuous curves). From the fit of the left one results: $g^{(2)}(0) = (0.07 \pm 0.04)$[136]. c) Intensity measurements as a function of power of a G-center (blue circles) and of the background (green circles). The blue and green continuous curves are the fit of the data while the black curve is obtained as the difference between them[136]. d) On the left, low temperature spectrum of an ensemble of G-centers. The coloured areas represent the spectral width of the two bandpass filters used for spectrally selective time-resolved measurements of the ZPL and phonon sideband. On the right, the time-resolved PL signal intensity for the whole spectrum (black line), the ZPL only (blue line), and the phonon sideband only (red line). The green line indicates an exponential decay with a time constant of 5.9 ns[135].

smallest reported value for $g^{(2)}(0)$ is 0.07 ± 0.04 (see Fig. 2.10b), which is likely limited by the presence of spurious emission within the detection spot and by intrinsic dark counts of the detector. Therefore, the SPE nature of the G-centers has been successfully measured, showing a good single photon purity of the emission. It is worth mentioning that, to achieve the maximum photon purity, it would be optimal to create the G-centers within ^{28}Si which leads to the elimination of the inhomogeneous broadening resulting from the mixture of the three stable Si isotopes (^{28}Si,^{29}Si,^{30}Si) present in natural silicon. Moreover, ^{28}Si has a null isospin leading to the removal of any hyperfine interaction. As a consequence, luminescence measurements of defect within this material have shown sharp lines, with a full width at half maximum of less than 1 μeV (see Fig. 2.8), thus leading to a negligible contribution of the homogeneous broadening to the photon purity.

Another interesting properties that can be extracted from photoluminescence measurement is the Debye-Waller factor (DW), which is the fraction of power emitted in the ZPL respect to the total emitted power. This factor provides information on the electron-photon coupling, i.e. a higher DW implies a smaller coupling and vice versa [139]. In G-centers the measured DW is between 11% and 18%[135, 29, 136]. This factor can also be used to evaluate the brightness of this SPE. Indeed, all the measurements performed so far rely on the use of long-pass filters, hence the measured intensity comes from both the ZPL and the phonon sidebands. However, since most of the QIT require a high photon purity and indistinguishability, to successfully employ G-centers as SPEs we would need to select only the ZPL emission. To this end, the brightness of the source (in the ZPL) can be easily obtained multiplying the measured intensity for the DW. The brightest G-center measured was characterized by about 10^5 counts per second at the detector (as it can be seen in Fig. 2.10c) with a DW of 11%, thus the brightness of the source was about 10^4 count per second (i.e. a photon rate of about 10 kHz). Albeit being less intense than required to be employed in QIT (see Table1.1), G-centers show a good brightness if we take into account that: 1) the value shown is the one measured at the detector, hence to be compared with the other SPEs in Table 1.2 must be rescaled for the efficiencies of all the optics in the setup; 2) no effort have been made to increase the luminescence collection, therefore this value is, at best, only the 2% of the total emitted light[40]. This is confirmed by the measured radiative decay time. Indeed, independent groups have observed decay time between 4 and 10 ns[138, 135, 136] (see e.g. the one shown in Fig. 2.10d), therefore the achievable emission intensity is of the order of a hundred MHz. It is worth noting that embedding the G-center in a microcavity or in a photonic crystal cavity could greatly decrease the radiative lifetime, thanks to the Purcell effect, and thus drastically increase the emitter brightness.

2.2.3 Fabrication of G-centers

G-centers can be formed in several different ways. They can be obtained by bombarding silicon or SOI with gamma rays, electrons, neutrons and ions[140, 135, 141] or by exposing the samples to CF_4 plasma[142] or even by nanopattering them[143, 144]. G-centers can be realized also by laser annealing, after treating the surface properly[145].

Regardless of the technique employed, the formation of G-centers strongly depend on the amount of carbon atoms, and in particular substitutional carbons. The standard procedure for creating G-centers relies on implanting them in high quality silicon or SOI, in this way a better control over their density is obtained, combined with a minimal presence of defects of other nature. The process of realizing a G-center starts with the creation of an interstitial

silicon atom Si_i, e.g. bombarding the silicon lattice. The Si_i formed is highly mobile and can replace one of the substitutional carbon atoms already present in the crystal. The resulting interstitial carbon migrates until it binds to another substitutional carbon atom and to an interstitial silicon thus forming the G-center. This dependence results clear when comparing the photoluminescence intensity of samples containing different concentrations of carbon atoms[146, 147]. As expected, an higher amount of carbons will result in more G-centers formed and thus in an increase in the luminescence intensity. However, this trend does not go on indefinitely but there is a optimal concentration above which the luminescence starts to degrade[146]. This is likely due to the introduction of non radiative defects that worsen the signal.

The G-centers studied in this work are all formed within a SOI sample and they are all obtained in the same fashion. The SOI is firstly implanted with carbon atoms with an optimal dose to maximize the amount of centers formed. The implantation energy was instead changed to locate the carbon atoms at different depth within the silicon layer. After the implantation, the samples were annealed at high temperature to cure the unwanted radiation damages. Lastly the G-centers were formed by bombarding the samples with protons. The specifics of the fabrication processes are described in detail in Chapter 3.1.9.

2.2.4 G-centers as single photon emitters

In order to exploit G-centers in QIT we need to be able to fabricate and detect single and isolated defects to be employed as SPEs. The studies on isolated G-centers and their implementation in photonic devices are still few, however there are some promising results that paves the way for interesting future developments.

The first studies on isolated G-centers relies on the implantation of carbon atoms in SOI sample employing low doses, $\leq 10^{13}$ ions/cm^2. The results of the first measurements performed on a single G-centers are reported in Fig. 2.11. From the PL map we can clearly see that, despite the reduced carbon dose, a vast amount of G-centers are observed. Therefore, in order to focus on a single G-center at a time a high numerical optics must be employed (for example, the objective used in this work was characterized by $NA = 0.85$). Once identified the isolated ones their second-order autocorrelation function was measured finding a value of $g^{(2)}(0) \approx 0.3$ clearly showing their SPEs nature. The PL intensity of such defects displayed a saturation power of about 6 μW (measured before the objective). In addition to that, the defect PL intensity at saturation power is stable over time up to 30 minutes. These are promising results showing the potentiality of employing G-centers as SPEs. To this end, newer studies on isolated G-centers have shown even better results in terms of higher photon purity and brightness of the G-centers[136], as showed in Fig. 2.10.

Employing a similar fabrication approach, a single G-center embedded in a waveguide was recently realized[138], as shown in Fig. 2.11f. The waveguide, designed for single mode operations at 1278 nm, was fabricated by EBL in a SOI sample implanted with a low carbon dose (10^{13} ions/cm^2). An isolated G-center is then observed in the waveguide, see inset of Fig. 2.11f. This defect was optically characterized and showed an intensity at saturation and on the first lens was about 1 MHz. Moreover, the second order autocorrelation measurement results in $g^{(2)}(0) = 0.38 \pm 0.08$ proving the SPE nature of the defect. The reason behind this non-optimal photon purity is connected to the poor signal to noise ratio of the emission due to the limited coupling between the G-center and the waveguide (maximum $\approx 8.25\%$). However, this is only a first attempt and there is room for further improvements. Indeed, by

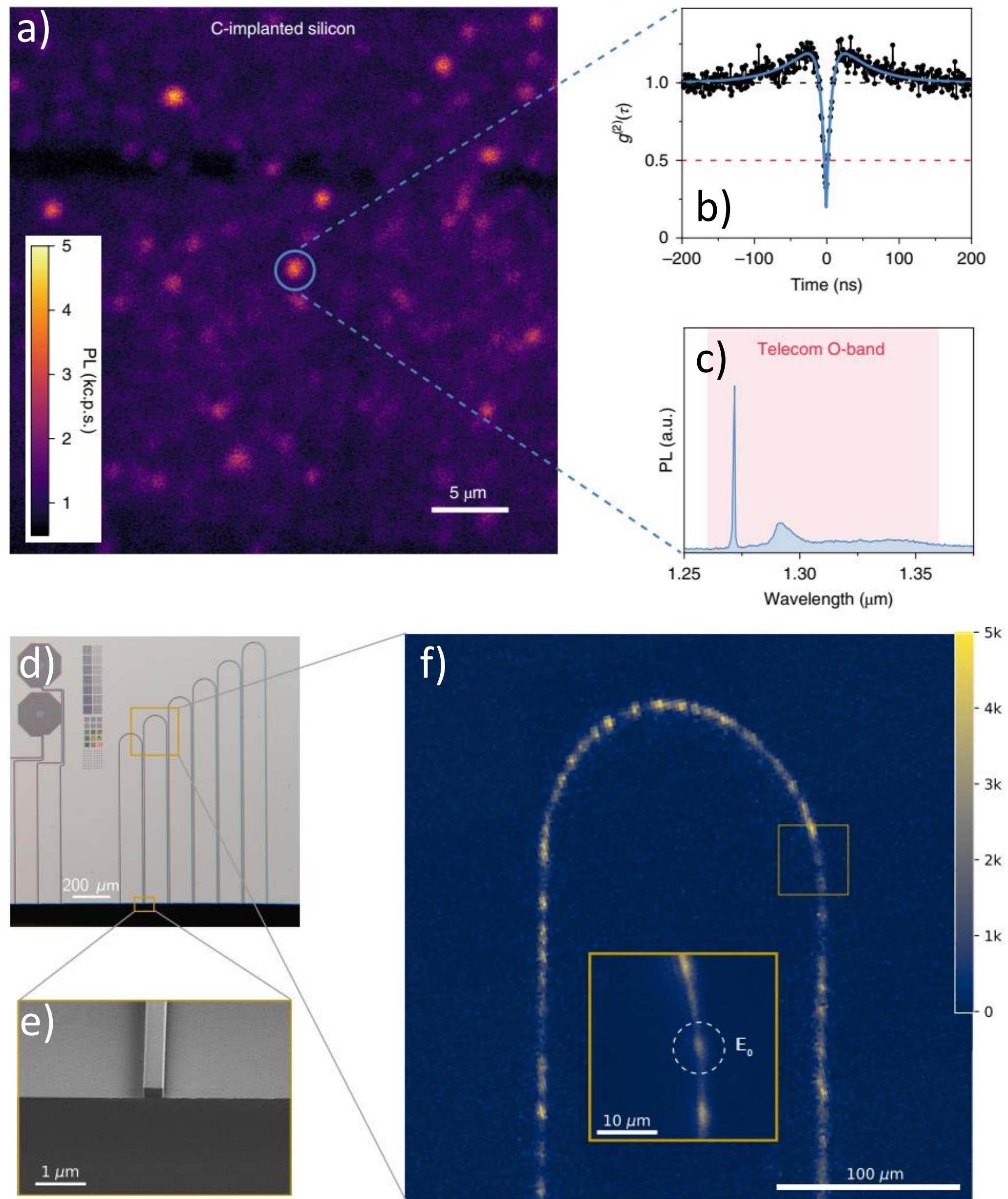

Figure 2.11. a) Low temperature (10 K) raster PL map. b) Second-order autocorrelation function $g^{(2)}(\tau)$ recorded on the isolated PL spot marked with the circle in a). The $g^{(2)}(0) < 0.5$ clearly show the SPE nature of the G-center under study. It is worth mentioning that the measured is performed without background correction. The solid line is data fitting with a three-level model describing the dynamics of optical cycles. c) PL spectrum of the studied G-center, showing emission in the telecom O-band (shaded red area)[137]. d) Microscope image of the sample showing the presence of different waveguides and structures. e) SEM image of the facet of the waveguide containing the G-center under study. f) Raster PL map of the emission. In the inset the single G-center studied[138].

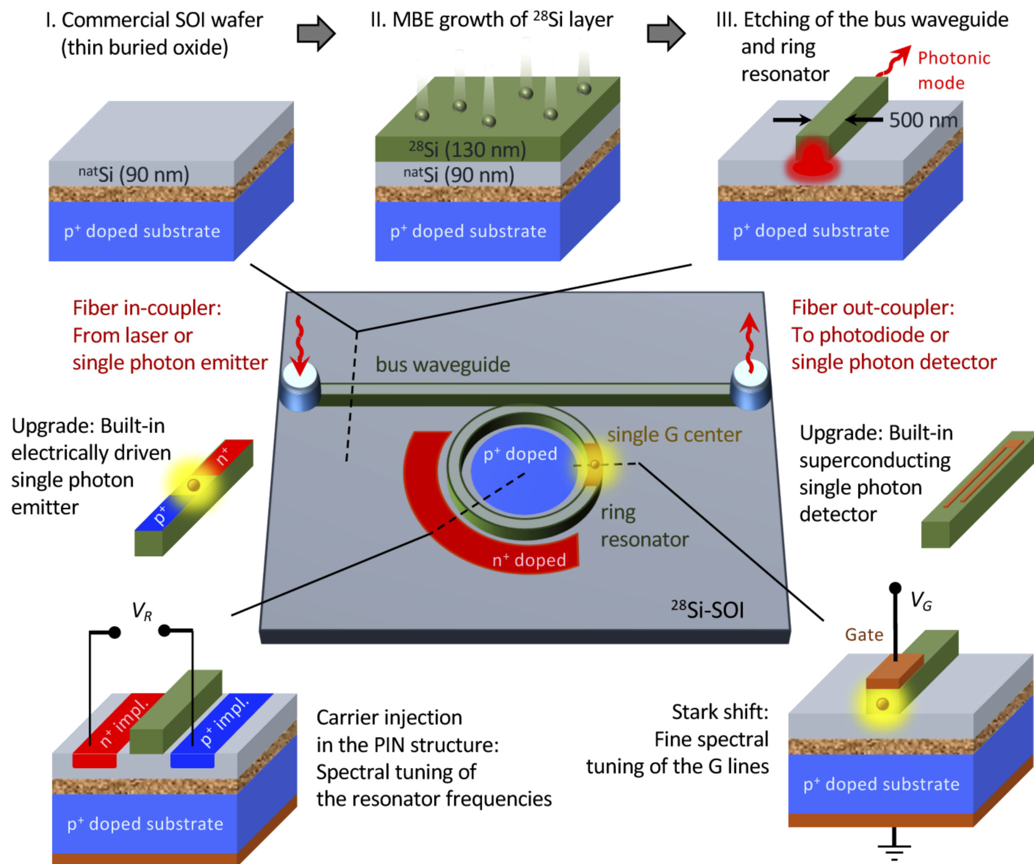

Figure 2.12. Sketch of the road map to realize a scalable Si-based chip with a single G-center as SPE [136].

simply employing spot-size converters or grating couplers, a coupling efficiency of about 80% is achievable.

These promising results suggest that all the tools developed for silicon based integrated photonic circuits could be exploited to manipulate single photons on a Si-based chip which can be easily scaled. A proposal in this direction has been made by Hollenbach et al.[136] and it is sketched in Fig. 2.12. They theorize the realization of a chip realized by growing ^{28}Si on conventional SOI and implant it with emitting impurities, e.g. G-centers. Then, top-down etching will be used to define photonic devices such as waveguides, resonators, logic gates, modulators, and light couplers. Finally, direct single photon detectors using superconductive wires[148, 149] will be the last step to fully operate quantum bits of light on a Si-based chip toward scaling.

2.2.5 Other technologies related to G-centers

QIT requires the use of SPEs, however ensembles of G-centers can be employed in many other applications. We will now briefly review two of them.

The first application regards the successful realization of a light emitting diode (LED) based on G-centers[150, 145] (see Fig. 2.13b). In this device, the defects are formed by boron implant or by laser annealing a carbon rich $n-$type silicon substrate. Then, the carriers

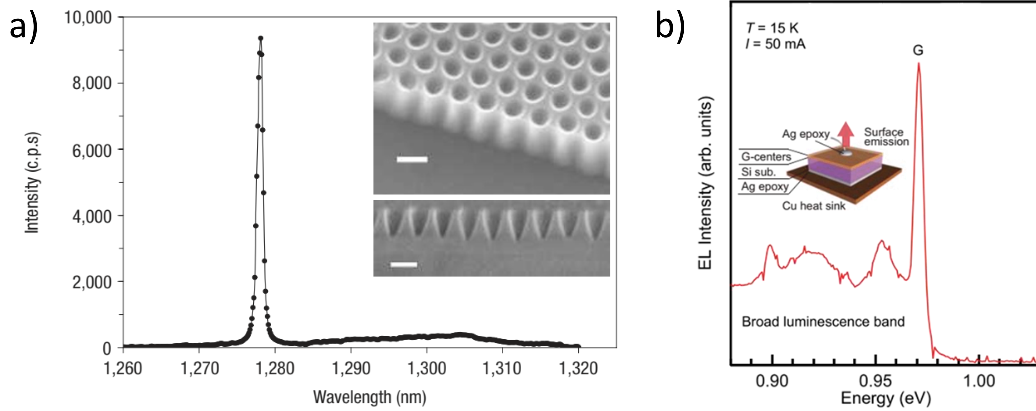

Figure 2.13. a) Low temperature edge-emission spectrum from the nanopatterned SOI. In the insets SEM images of the patterned structure, the scale bars represent 100 nm[143]. b) Low temperature electroluminescence (EL) spectrum of the G-centers, taken with a constant current of 50 mA. The inset shows a sketch of the measurement setup[145].

were electrically injected in G-centers exploiting the realization of a $p-n$ junction. Despite showing good optical properties, G-centers based LEDs are strongly limited by the need to operate at cryogenic temperatures (at least 77 K) to show a proper electroluminescence signal. However, the interesting result of these work is the ability to electrically control and induce the G-centers luminescence. Indeed, this would lead to the realization of an electrically-driven SPE, which could be of interest for several QITs applications.

A second application of ensembles of G-centers relies on their use to realize a laser[143, 151]. To do so, the emitters were integrated in photonic device formed by patterning a SOI sample, containing only native carbon atoms, with nanoholes (see Fig. 2.13a). The reactive ion etching process needed to realize the nanoholes was responsible for the formation of the G-centers within the sample. Observing the edge emission at low temperature, a strong photoluminescence signal is observed. Comparing this signal with respect to the one from an unpatterned sample a increase up to 40 times is observed. Moreover, the signal presented some characteristics in common with a laser emission: the presence of stimulated emission, a significant optical gain, a threshold transition and a collimated emission in the far-field. However, further studies are required to successfully implement a laser based on G-centers, moreover there is still the drawback of needing cryogenic temperature for it to work.

All these results show the potentialities of G-centers that could be employed both as SPEs for QIT and for the development of LEDs and lasers at telecom wavelength.

Chapter 3

Experimental details

In this chapter the fabrication and characterization setups and techniques will be described, along with the software employed for the simulations. Moreover, the fabrication processes and structures of the samples employed in this thesis work will be described.

3.1 Fabrication techniques and setups

3.1.1 Molecular Beam Epitaxy

Molecular Beam Epitaxy (MBE) is a growth technique employed to fabricate thin films of single crystals. It is one of the cleanest and most precise growth technique, that grants control over single atomic layers.

The MBE experimental setup is sketched in Fig. 3.1. It consists in several effusion cells in which the elements are heated until sublimation. Then, the gaseous elements moves thanks to their thermal energy and condensate over a substrate, which is kept in rotation and heated to maximize the homogeneity of the deposition. To limit the contamination from spurious elements, the MBE growth process takes place in ultra high vacuum (UHV, down to 10^{-11} mbar). The term "beam" refers to the long mean free path of the elements within the MBE, which leads them to reach the substrate without interacting with each other along the way. Once on the substrate, the different elements can react and form the crystalline layer. Therefore, by introducing the elements in a controlled way within the chamber, MBE grants the possibility to grow crystalline alloys.

The properties of the growth layers can be finely tuned changing the cells parameters, e.g. the opening time intervals or the temperature, or changing the substrate temperature or rotation speed.

The growth process is monitored using RHEED, Reflection High-Energy Electron Diffraction. This is a non destructive in-situ technique that consists in bombarding the sample surface with high energy electrons (typical energies are between 15 and 30 keV) produced with an electron gun. The diffracted electrons interfere constructively only at specific angles according to the crystal lattice parameters and the electron wavelength. Within the RHEED energy range, the electrons interact only with the upmost atomic layer giving us information on the layer growth process. Moreover, observing the electrons pattern during the whole process, several additional information can be obtained: the surface roughness, the growth rate, the crystal orientation and the presence of strain.

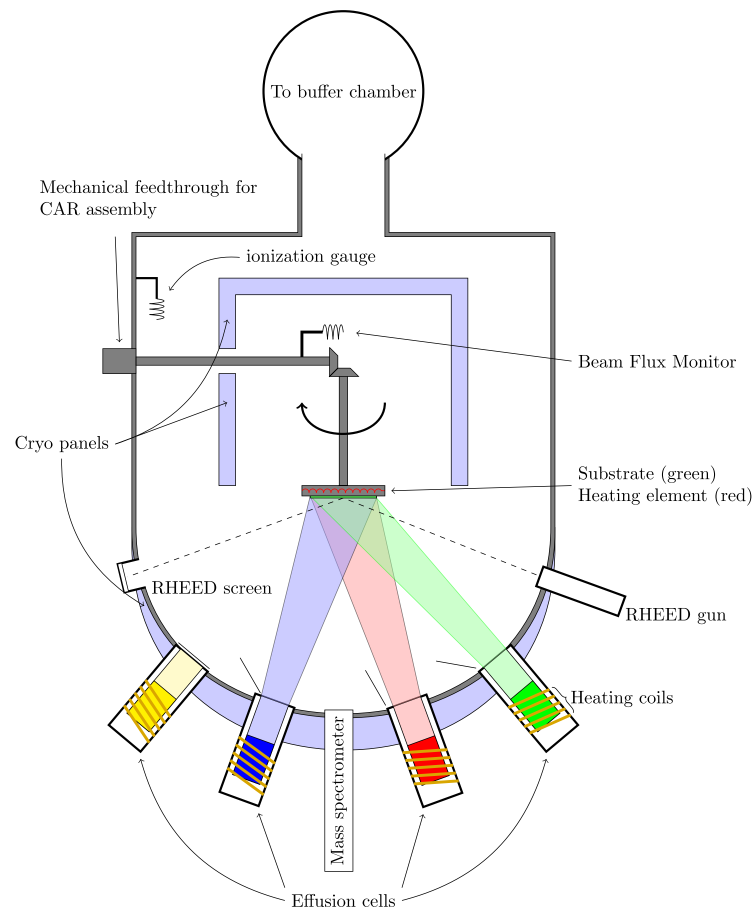

Figure 3.1. Sketch of the main chamber of a MBE machine.

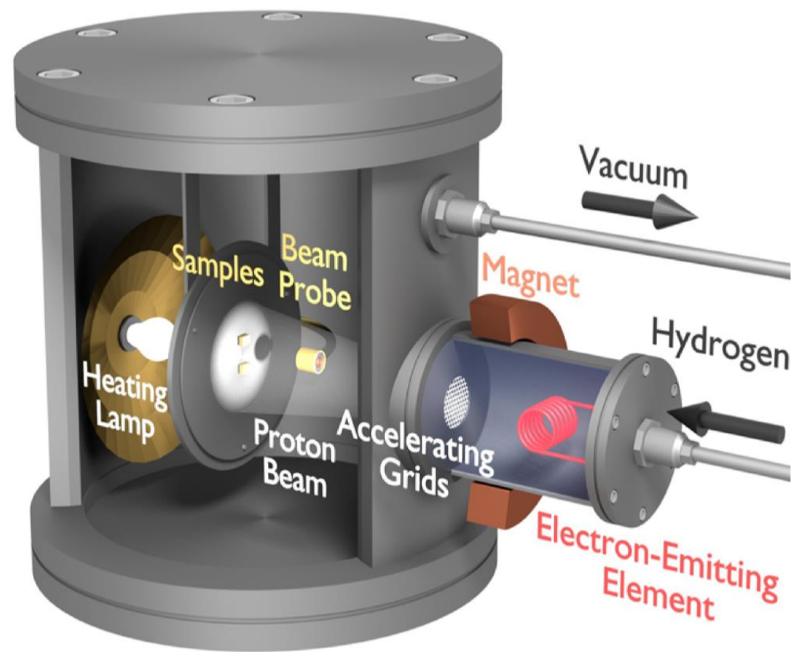

Figure 3.2. Sketch of a Kaufmann source employed to hydrogenate samples.

In this work MBE was employed to grow the sample employed in the $GaAs_{1-x}N_x$ QDs fabrication. In particular, the sample consisted in a multilayer structure formed by: a GaAs buffer (130 nm) deposited on a (001) GaAs substrate, followed by a sacrificial layer of $Al_{0.7}Ga_{0.3}As$ (1500 nm), a GaAs lower cladding (130 nm), a $GaAs_{0.989}N_{0.011}$ layer (6 nm), and a GaAs upper cladding (30 nm)[152].

The QW fabrication process was performed by the group of Prof. Mark Hokinson from the University of Sheffield (UK).

3.1.2 Ions implantation

Ion implantation is a process by which ions of one elements are accelerated into a target to change its physical, chemical, or electrical properties. In semiconductor technologies ion implantation is typically used to dope the targets using non isovalent elements. In this work, instead, it was used for introducing carbon atoms within SOI samples and to hydrogenate both the SOI samples and a $GaAs_{1-x}N_x$/GaAs QW. However, the ion implants were performed with two different setups. The SOI samples are treated using a ion beam implanter (VIISta 80) while the hydrogenation of the $GaAs_{1-x}N_x$/GaAs was performed with a Kaufman source.

A conventional ion implanter consists in a ion source, where the desired ions are produced, an accelerator, where the ions are accelerated to the desired energy, a mass spectrometer, that allows us to select the correct isotope and ion (if spurious atoms are present), and a target chamber, where the ions impinge on the target. Typical ion energies are in the range of 10 to 500 keV, while the dosage, i.e. the amount of ions per cm^2, can be controlled changing the beam size, e.g. with the use of metal masks, and the implant time. A control over the ions energy is of utmost importance to tune the ions depth within the target.

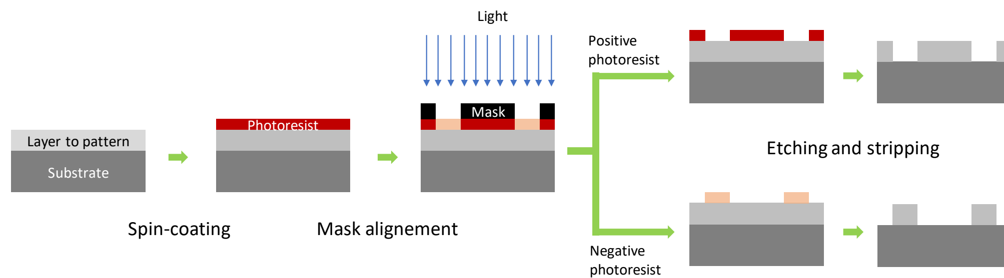

Figure 3.3. Scheme of a typical optical lithography process.

The expected depth can be calculated using simulation software such as SRIM (see below).

The SOI samples employed in this work were implanted with carbon atoms in two different runs, in order to have two different implant depth. Moreover, after patterning the samples, they were implanted with protons to form the G-centers. The exact energies and fabrication process will be described in a following section.

The carbon implantation in SOI samples was carried out by Ion Beam Service at Aix-en-Provence (FR), while the hydrogen implantation by the group of Tobias Herzig from the University of Leipzig (DE).

A scheme of a Kaufman source is shown in Fig. 3.2. As we can see, it consists in a heated cathode that emits thermionic electrons which are accelerated by the presence of a potential difference between the cathode and a positively biased anode. Due to the presence of a magnetic field the electrons drift in a cycloidial path during which they impact to the gas molecules previously injected in the system, resulting in their ionization. The ions are then extracted employing negatively biased accelerating grids that attract them. The extracted ions flow through the grids apertures forming an ion beam that is directed to samples. To increase the ions diffusion within the samples they are heated employing a heating lamp.

In this work the Kaufman source was employed to fully hydrogenate the $GaAs_{1-x}N_x$/-GaAs QW in the sample used for the QDs fabrication.

The hydrogenation process was performed by the group of Prof. Marco Felici at Sapienza-University of Rome (IT).

3.1.3 Optical lithography

Optical lithography is a lithographic technique that involves the use of visible and ultraviolet light (10-400 nm) to realize patterns within a material. Thanks to the high resolution achievable ($\sim$ 10 nm) [153], optical lithography is widely diffused for the fabrication of microelectronic circuits.

The main elements of the technique are: a photoresist, a developer, a light source and an etching system. The photoresist is a photo-sensitive material that changes its solubility when exposed to light. In particular, positive photoresists become more soluble in the developer after being exposed to light, while the negative ones become less soluble. The developer is an aqueous substance used to develop the pattern by dissolving the shined (not shined) areas of the positive (negative) resist. The light source employed to shine the photoresist is a LED or a laser. Finally, the etching system is employed to transfer the pattern from the photoresist into the material, as explained in the following.

A typical optical lithography process is schematize in Fig. 3.3. First, the photoresist is spin-coated on top of the material to pattern. The spin-coating approach is used to homogeneously spread the resist, which thickness is controlled by changing the spinning velocity, and to facilitate the evaporation of the solvent contained in it. Then, the solubility of the resist is locally modified. This can be done placing a patterned mask on top of the resist and illuminating it or by locally shining the resist with a laser[154]. After this process, the sample is immersed in the developer to dissolved the non illuminated resist (or vice versa with negative photoresist), thus obtaining a patterned resist. Then, the pattern is transferred to the material by etching the areas of the sample not covered by the resist. The etching process can be done by chemical attack [155], by ion bombardment [156, 157] or, as was done in this work, by plasma etching. In particular, we used a tetrafluoromethane (CF_4) plasma to etch the Si layer on top of SOI samples. As a last step, the resist is stripped away using acetone.

In this work the lithographic system employed is the Dilase 250 by Kloé. The Dilase 250 is a laser-based lithography system equipped with a laser source emitting at 375 nm and characterized by a maximum power density of about 2.7 mW/cm^2. The spatial resolution achievable with this instrument is around 2 μm. The Dilase working principle consists in direct laser writing the desired pattern into the photoresist, thus avoiding the need of a patterned mask. The writing process is done by mounting the sample on an $x-y$ translation stage, which moves the sample with a precision of about 100 nm, and controlling the laser power and the sample movements via software. Therefore, with the Dilase there is the possibility to create arbitrary shaped patterns, however this process requires much longer processing time respect to mask based lithography processes.

Lithography was employed to pattern SOI samples containing G-centers in order to create silicon suspended membranes.

3.1.4 Electron beam lithography

Similar to optical lithography, electron beam lithography (EBL) is a technique to realize patterns and structure within a material. It is based on the same working principles however, in EBL a focused beam of electrons is used to change the solubility properties of the resists, thus leading to a sub-10 nm resolution[158]. To achieve this resolution the beams are formed by field electron emission sources which have a lower energy spread respect to thermionic sources. The electrons extracted are then accelerated and their trajectory is controlled by means of electrostatic and magnetic lenses. In this way custom patterns are realized in the resist and then transferred to the sample by means of dry or wet etching.

In this work EBL (Vistec EPBG 5HR working at 100 kV) was employed to realized arrays of annular apertures within the sample containing the $GaAs_{1-x}N_x$:H/GaAs QW employed to fabricate the QDs. These apertures were then exploited to realize suspended circular membranes.

The EBL patterning process and the membrane realization was performed by the group of Dr. Giorgio Pettinary from the CNR-IFN Rome (IT).

3.1.5 $GaAs_{1-x}N_x$ QDs fabrication setup

The QDs fabrication process will be described in detail in a following section. However, in few words, it consists in the illumination of dielectric microspheres deposited on top

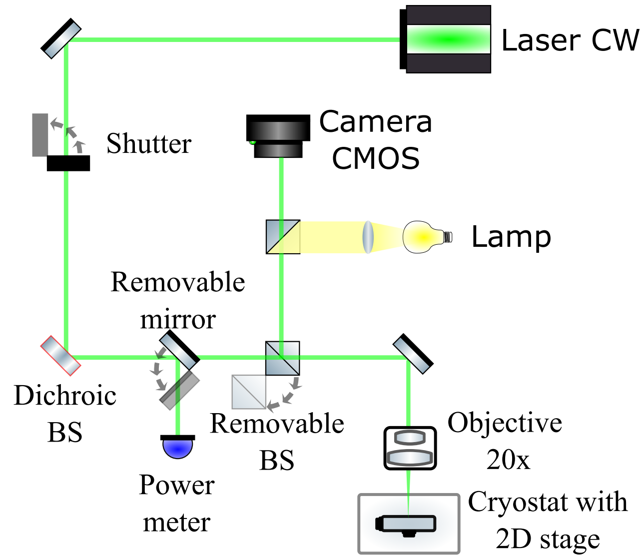

Figure 3.4. Sketch of the fabrication setup.

of the GaAs$_{1-x}$N$_x$:H/GaAs QW with a laser light. To do so, we have employed a setup that consists in a home-made confocal microscope setup in backscattering configuration. A scheme of the setup is shown in Fig. 3.4.

The sample is placed on the sample holder of a low-vibration Janis ST-500 continuous He-flow cryostat, which, in turn, is mounted on a Physik Instrumente $x-y$ translation stage to move the sample with a fine control on the position of about 250 nm. The light source used to illuminate the microsphere is a CW diode-pumped solid state laser emitting at 532 nm (CNI MLL-III-532) which is focused on the sample through a 10× objective with NA = 0.2. This objective was selected to grant a homogeneous illumination of the microspheres. For all the fabricated QDs, the microsphere were illuminated for 1 s. The exposure time was controlled via an automatic shutter (ThorLabs SH05) connected to a controller (Thorlabs KSC101) that grants a temporal reproducibility of about 0.2%. To realize QDs of different sizes, different laser powers were used. The laser power is measured immediately before the objective with a power meter (ThorLabs PM120VA). An imaging system formed by a CMOS camera and a white lamp was used to scan the sample surface and to align the objective with the microspheres. The system is connected to the excitation-collection path through a removable 30/70 beam-splitter.

3.1.6 Plasma-enhanced chemical vapor deposition

Plasma-Enhanced Chemical Vapor Deposition (PECVD) is a technique used to deposit thin layers onto a substrate. Like in others Chemical Vapor Deposition (CVD) techniques, the substrate is exposed to one or more gaseous precursors which react and/or decompose on the substrate surface to produce the desired deposit. Typically, the substrate is heated to facilitate the deposition process and increase the homogeneity of the layers. The peculiarity of PECVD is that the gaseous precursors, before entering in the deposition chamber, are heated and ionised to form a plasma (see Fig. 3.5). The plasma can be formed by a direct current discharge between one electrode and the substrate or by applying an alternating

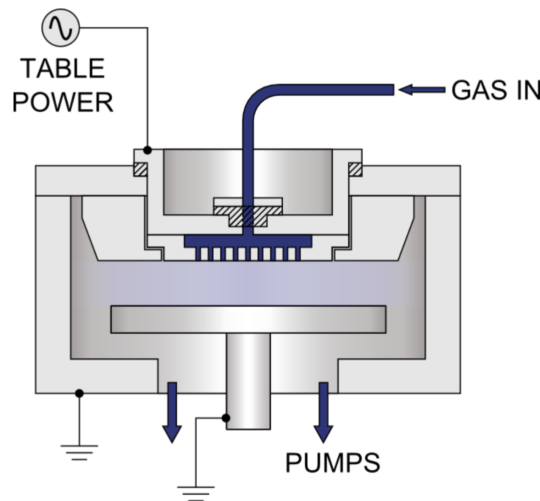

Figure 3.5. Sketch of a PECVD machine.

current discharge between two electrodes (on top of one of which there is the substrate) at low or high frequency (LF and HF, respectively). It is worth noting that the former process require a conductive substrate while this condition in relaxed in the latter. When realising the plasma using alternate current, its frequency has an important role in the deposited layer properties. An example of this is silicon nitride (SiN_x), where the plasma frequency is directly connected to the deposited film strain. Indeed, if only LF is employed the resulting film will be characterized by a compressive strain, while if only HF is employed the stress will be tensile [159]. Therefore, with a proper combination of HF and LF it is possible to deposit a SiN_x film of arbitrary strain. The combination is performed alternating one cycle of pure HF with one cycle of LF and by controlling the pulse duration of the two cycles we can achieve strain control[159].

The PECVD employed in this work is the PlasmaPro 8o PECVD from OXFORD and it was employed to etch the SOI samples during the fabrication of the suspended membranes and to strain them depositing SiN_x layers on top of them. In detail, for the former process the gas used is CF_4, while heating the substrate at 50°, instead, for the deposition a mixture of SiH_4 (silane) and NH_3 (ammonia) is used, while heating the substrate at 300°. The theoretical stochiometric chemical reaction that leads to the formation of silicon nitride is the following:

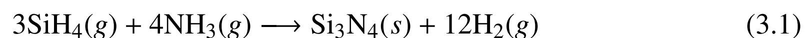

$$3SiH_4(g) + 4NH_3(g) \longrightarrow Si_3N_4(s) + 12H_2(g) \tag{3.1}$$

however, the silicon nitride produce by PECVD is rarely stochiometric and might be highly hydrogenated, therefore we will refer to it with the more general formula SiN_x. Both the depth of the CF_4 etching and the thickness of the deposited SiN_x layers were controlled changing the processing time.

3.1.7 Rapid Thermal Processing

Rapid thermal processing (RTP) is a technique that exploit infrared halogen lamps to subject samples to extremely fast annealing (heating ramps up to 50° C/s). The RTP machine can work in air, in vacuum (down to 10^{-6} mbar), or can be injected with gasses such as N_2 and

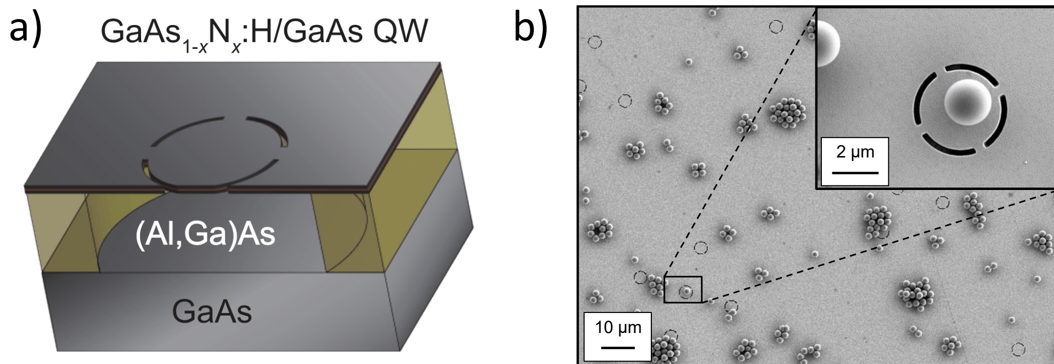

Figure 3.6. a) Sketch of the sample employed to fabricate the $GaAs_{1-x}N_x$ QDs. b) SEM image of the sample after the microspheres deposition. In the inset: magnification of a single microsphere on top of a suspended membrane.

O_2. The use of N_2 is connected to reduce contamination within the processed samples while O_2 can be used to oxide the surface of the samples. In the latter scenario we refer to the process as rapid thermal oxidation (RTO). RTO relies on heating of the wafer to increase the diffusion coefficient of oxygen. For example, SiO_2 is naturally formed on top of Si, however its formation rate is quite small[160], therefore to speed-up the process it is necessary to increase the wafer temperature. This oxidation process can be used also to thin the topmost silicon layer in SOI samples. Indeed, the SiO_2 that is formed after the RTO process can be easily removed using HF thus reducing the thickness of the silicon layer. This process can be repeated until the desired thickness is achieved.

In this work all the rapid thermal processes are performed using the JetFirst 100 from Jipelec. In particular, RTP in nitrogen atmosphere was done to recrystallize SOI samples after being implanted by carbon atoms.

3.1.8 $GaAs_{1-x}N_x$ QDs sample structure

The sample employed for the fabrication of $GaAs_{1-x}N_x$ QDs consists of a $GaAs_{1-x}N_x$/GaAs ($x = 0.011$) quantum well (QW), which was grown by MBE with the following structure: a GaAs buffer (130 nm) was deposited on a (001) GaAs substrate, followed by a sacrificial layer of $Al_{0.7}Ga_{0.3}As$ (1500 nm), a GaAs lower cladding (130 nm), a $GaAs_{0.989}N_{0.011}$ layer (6 nm), and a GaAs upper cladding (30 nm)[152]. The sample was then moved to a vacuum chamber, where it was kept at a constant temperature of 190 °C and exposed to a flux of hydrogen ions generated by a low energy Kaufman source (beam energy 100 eV, beam size about 3 cm) with an ion current density of 25 $\mu A/cm^2$ for about 500 s. The total dose of H was 8×10^{16} $ions/cm^2$, sufficient for a complete passivation of the nitrogen atoms. An excess of hydrogen has the only effect to favour the formation of N-2H-H complexes with respect to the N-2H ones, thus introducing a moderate compressive strain in the sample[103, 52].

Subsequent to the hydrogenation process, the sacrificial layer between the QW and the substrate was removed to obtain an array of well-separated circular suspended membranes with a diameter of few µm[161].

In order to achieve this goal, an array of annular apertures of 4 µm in diameter and 200 nm in width is patterned by EBL (Vistec EPBG 5HR working at 100 kV) into a positive-tone resist (ZEP 520 A) spun on the sample's surface and developed in a mixture of MIBK:IPA

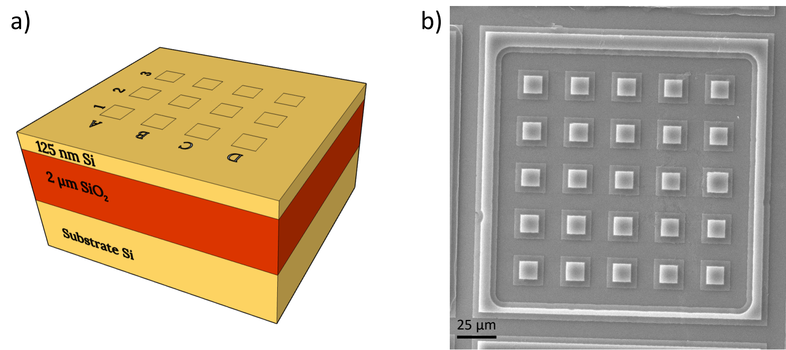

Figure 3.7. a) Sketch of the sample employed to realized the silicon suspended membranes. The 12 squares on top of the sample represent the 12 fields. b) SEM image of one of the fields after the realization of the suspended membranes. The whiter coloured parts are the silicon dioxide areas that support the suspended membranes, which are the transparent squares around the supports.

(1:1). Then, the apertures are transferred into the sample, down to the AlGaAs layer, by means of a chlorine-based Reactive Ion Etching (with a Cl_2:BCl_3:Ar gas mixture). Finally, the residual masking resist is removed with anisole, and the GaAs membranes are released by a wet etching in HF (5%) of the AlGaAs sacrificial layer (see Fig. 3.6a) for a sketch of the sample). These suspended membranes have two functions: one, creating a low refractive back reflector due to the mismatch of refractive index between GaAs and air, thus helping the luminescence collection, and two, prepare the sample to the future realization of photonic crystal cavities to be coupled with the fabricated QDs. The membrane thickness (166 nm) was chosen to exclude the presence of any slab waveguide modes of order higher than the fundamental ones (TE_0 and TM_0) in the wavelength range of interest (about 900 nm).

Lastly, a series of dielectric microspheres were randomly deposited on top of the sample (see Fig. 3.6b). The microspheres are composed of silicon dioxide and are characterized by a mean diameter of 2.06 μm with standard deviation of 0.05 μm (Microparticles GmbH). They come in aqueous suspension making up 5% of the weight/volume percentage. The spheres were deposited with an airbrush (Point Zero PZ-270) with 0.2 mm nozzle diameter. The sample was placed at large distance from the airbrush, in order to ensure the complete evaporation of the liquid contained in the sphere solution, thus leaving only the spheres before hitting the sample. Additionally, a high air pressure was used for the airbrush; as a result, small droplets similar to a mist were formed, which also aids the evaporation process.

3.1.9 G-centers sample structure

All the samples employed in this work were made from a commercial SOI, Silicon On Insulator, wafer made by Soitec. In particular, the samples contained: a silicon substrate, a 2 μm thick SiO_2 layer and 125 nm thick silicon layer. They were divided in two groups and implanted with carbon atoms following a well-established procedure[146] in two different runs. Sample 1.3 and 1.4 were implanted with a nominal carbon doses of $5.5 \cdot 10^{14}$ ions/cm^2 and with a beam energy of 6 keV, resulting in an implant depth of (24 ± 11) nm (from SRIM simulation). Sample 7.3 was implanted with a nominal doses of $6.5 \cdot 10^{14}$ ions/cm^2 and with a beam energy of 30 keV, resulting in an implant depth of (99 ± 40) nm (from SRIM simulation). After the implant, all the samples were flash annealed in N_2 atmosphere for 20 s at 1000° C to cure the radiation damages.

Table 3.1. SiN_x deposition parameters for the three samples studied.

Sample	HF_P (W)	LF_P (W)	HF_t (%)	Strain
1.3	0	100	0	Compressive
1.4	300	0	100	Tensile
7.3	20	80	70	Unstrained/Slightly Tensile

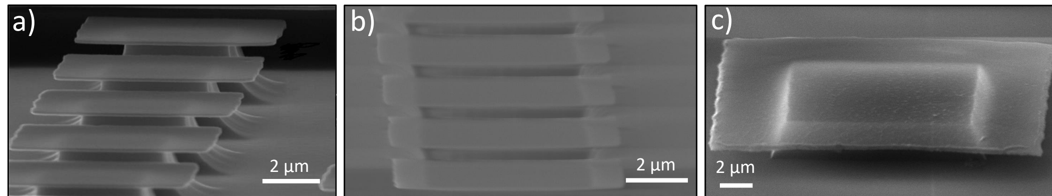

Figure 3.8. Tilted SEM images of the suspended membranes. a) Image of membranes before the deposition of the SiN_x layer. The membranes are flat and parallel to the substrate. b) Image of membranes with a tensile strained SiN_x layer on top. The membranes are bent upwards. c) Image of a membrane with a compressive strained SiN_x layer on top. The membrane is bent downwards.

The sample were then patterned using an optical lithography process described as follows. Firstly, each sample was cleaned in a sonic bath with acetone and after with ethanol. Then the sample was mounted in a spin-coater and a drop of positive photoresist (MICROPOSIT S1813) was deposited on top of it. By rotating the sample at 3000 rpm the phtoresist was homogeneously deposited on the sample surface, forming a layer of about 1.5 um. The sample was then inserted in the photolithography system (Dilase 250) and a predetermined pattern was laser-written into the resist. The pattern consists in 12 square fields divided in three rows, labeled with numbers, and four columns, labeled with letters (see Fig. 3.7a). Each field is 200 um×200 um and contains 25 nominally identical squares which size depends on which column the field is in. Moving from column A to column D the nominal squares size is 10, 12, 15 and 20 um. After this, the sample was immersed in the developer (MICROPOSIT MF-319) to remove the resist which was not laser-written. The pattern was then transferred to the sample by etching it with CF_4 plasma. After, the remaining resist was stripped away using acetone. The etching process lead to exposing the SiO_2 layer which was partially chemically etched to realized the suspended membranes. To do so the sample was immersed in an aqueous solution containing the 10% of Buffered oxide etch (BOE 10:1). The immersion time was controlled to maximize the suspended part of the membranes. An example of a patterned field containing the suspended membrane is shown in Fig. 3.7b.

Then, a ~ 100 nm thick SiN_x layer is deposited on top of each samples with PECVD. The three depositions are performed using different parameters which are summarized in Table 3.1. Where HF_P and LF_P represent the high and low frequency power, respectively, while the HF_t, represents the fraction of time in which the high frequency pulse is turned on respect to the the total pulse time (20 s) expressed as a percentage (for more details see Chapter 3.1.6). The former parameters define the SiN_x deposition rate, while the latter determine the amount an kind of strain of the layer. In particular, changing HF_t results in obtaining a compressive ($HF_t < 60\%$), tensile ($HF_t > 65\%$) or almost unstrained ($60\% < HF_t < 65\%$)

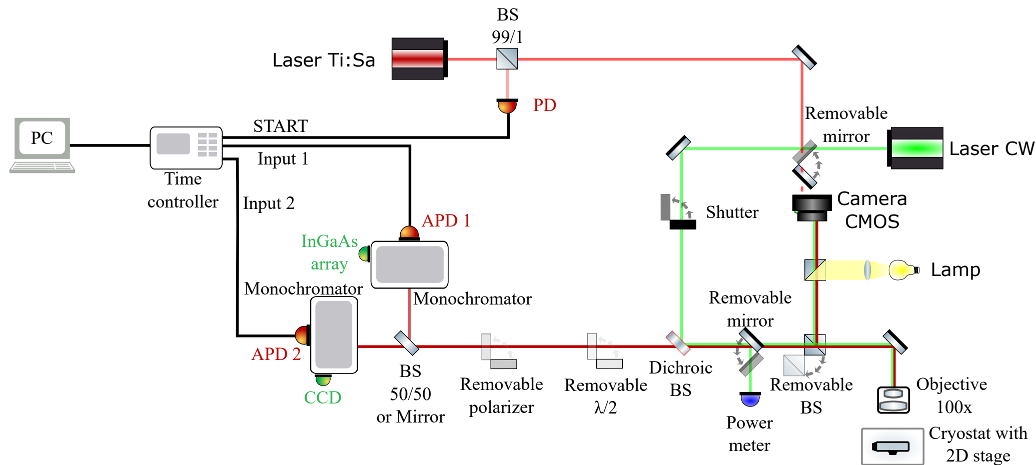

Figure 3.9. Scheme of the micro-PL setup.

SiN_x layer[159]. As a consequence, the strained SiN_x affects the silicon suspended layer thus resulting into a bent membrane, upwards (tensile strain) or downwards (compressive strain), as we can see in Fig. 3.8.

As a final step, each sample was implanted with protons, to form the G-centers (see Chapter 2.2.3 for more details), using a fluence of $1 \cdot 10^{14}$ ions/cm^2 and an implantation energy of 90 keV (proton range $\approx$ 830 nm).

3.2 Characterization techniques and setups

3.2.1 Micro-photoluminescence setup

The micro-photoluminescence (micro-PL) spectra showed in this work are measured with a home-made confocal microscope setup in backscattering configuration. A scheme of the setup is shown in Fig. 3.9.

The samples are placed in a low-vibration Janis ST-500 continuous He-flow cryostat, which, in turn, is mounted on a Physik Instrumente $x-y$ translation stage to scan the sample surface with a fine control on the position of about 250 nm. The liquid He flow thanks to a pressure difference thus avoiding the need of a pump, drastically reducing the vibrations of the system. The samples temperature can be fixed within a range of $10-300$ K and it is kept stable thanks to an electrical heater connected to the sample holder, which has a sensitivity of 0.01 K. Inside the cryostat a vacuum atmosphere (down to $\sim 10^{-7}$ mbar) is created by means of a sequence of turbomolecular and rotative pump.

As schematize in Fig. 3.9 the excitation sources are a CW diode-pumped solid state laser emitting at 532 nm (CNI MLL-III-532) and a mode-locked Ti:Sapphire tunable laser (Spectra Physics Tsunami, 700-900 nm spectral range, 200 fs pulse duration, 12.2 ns pulse period), pumped by a frequency doubled Nd-YAG laser. Along the excitation line of the setup an automatic shutter (ThorLabs SH05) connected to a controller (Thorlabs KSC101) is placed. The excitation power is measured with a power meter (ThorLabs PM120VA) immediately before the objective thanks to a removable mirror on the excitation path.

The PL from the samples is collected by one of the two infinity corrected Mitutoyo

100x objectives available (NIR, NA = 0.7, 378-864-5; VIS, NA = 0.7, 378-806-3). The luminescence, separated from the excitation by a dichroic mirror, is spectrally dispersed by two Acton SP2300i spectrographs in Czerny-Turner configuration, both mounting a 600 gr/mm grating and a 1200 gr/mm grating (blazed at 1000 nm and 750 nm, respectively). The two spectrographs are used simultaneously, combined with a 50/50 beamsplitter, only to create a Hanbury Brown and Twiss interferometer to perform second-order autocorrelation ($g^{(2)}(\tau)$) measurements. For all the other measurements only one of the two is employed, to maximize the collected PL intensity. The spectrograph is chosen accordingly to the wavelength range of the PL emission since one of them is equipped with a Si CCD (Acton Pixis 100F), used for the PL emission in the near UV-visible region, the other one is an InGaAs array (Princeton Instruments OMA V-512), used for the PL emission in the near-infrared-infrared region. Both the detectors are cooled to minimize the dark current and other sources of noise. In particular, the CCD is kept at $-70°$ C by a double stage Peltier module, while the array is kept at $-100°$ C by a cold finger immersed in liquid nitrogen. The spatial resolution of the system is less than 1000 nm and the spectral resolution change accordingly to the combination grating-detector: it is about 400 μeV with the 600 gr/mm grating and the CCD, about 250 μeV with the 1200 gr/mm grating and the CCD and about 350 μeV with the 600 gr/mm and the InGaAs array. In Tables 3.2 and 3.3 are reported the efficiencies of all the optical component in the setup at 930 nm and 1280 nm. These value are obtained from the tabulated data reported by the manufacturers.

Time-resolved PL (TR-PL) measurements were performed using the time correlated single photon counting (TCSPC) technique. The spectrally dispersed luminescence was selected using the exit slit of the spectrograph and sent to one of the three different APD available. Two of them are used for signals in the visible and near-infrared spectral range (350 − 1050 nm) and the third one for near-infrared and infrared signals (950 − 1700 nm). The former, employed to measure the TR-PL of the $GaAs_{1-x}N_x$ QDs, are two identical single photon counting Si APDs made by PerkinElmer (SPCM-AQR-16). While the latter, employed to measure the TR-PL of G-centers, is a single photon counting InGaAs/InP APD made by ID Quantique (ID230). The two Si APDs are also used as detectors in the Hanbury Brown and Twiss interferometer for the measurements of the $g^{(2)}(\tau)$. In this configuration the signals from the two APDs were processed with proper fast electronics (Tennelec TAC, Canberra MCA) interfaced with a computer. While when the InGaAs/InP APD was employed the signal was processed with a time controlled (ID Quantique ID900) interfaced with the PC. The time resolution of the system depends on the APD used, with the Si APDs is about 400 ps while with the InGaAs/InP APD is about 200 ps.

Polarization measurements are performed by placing a rotatable half-wave plate and a polarizer along the collection path. The latter is necessary to perform measurements without being affected by the dependence of the monochromator efficiency on the polarization of the signal.

The angle-resolved PL measurements are obtained using a pinhole, mounted on two programmable stages, introduced along the collection path. The pinhole act as an angular (or k-momentum) filter and thus, by scanning the collimated beam exiting from the objective it is possible to perform the angle resolved measurements. This is done by performing a 2D raster map where, for each position of the pinhole a PL spectrum is collected and then integrated to obtain the map. The conversion between the (x, y) coordinates of the pinhole and the corresponding (k_x, k_y) (in units of $2\pi/\lambda$) of the emitter under study is performed by simply dividing the real space coordinates by the focal length of the objective (2 mm).

An imaging system formed by a CMOS camera and a white lamp can be used to scan and photograph the samples surface. The system is connected to the excitation-collection path through a removable 30/70 beam-splitter.

Table 3.2. Tabulated efficiencies of all the components of the micro-PL setup at 930 nm.

Object	Efficiency at 930 nm
Cryostat JANIS ST-500 uncoated quartz window	0.93
Objective Mitutoyo 378-806-3[1]	0.35
Mirror Thorlabs PF10-03-P01P (×3)	$0.97 \times 0.97 \times 0.97$
Dichroic mirror Semrock FF560-FDi01-25x36	0.98
Focusing lens Thorlabs AC127-019-B-ML	0.99
Grating Princeton Instr. 600 gr/mm, BLZ 1 μm	0.80
Silver mirrors inside spectrograph SP2300i (×3)	$0.97 \times 0.97 \times 0.97$
CCD Princeton Instr. PIXIS 100F (1340 × 100)	0.19
TOTAL SETUP	**0.04**

Table 3.3. Tabulated efficiencies of all the components of the micro-PL setup at 1280 nm.

Object	Efficiency at 1280 nm
Cryostat JANIS ST-500 uncoated quartz window	0.85
Objective Mitutoyo 378-864-5	0.56
Mirror Thorlabs PF10-03-P01P (×3)	$0.97 \times 0.97 \times 0.97$
Dichroic mirror Semrock FF875-FDi01-25x36	0.97
Focusing lens Thorlabs AC127-019-C-ML	0.99
Grating Princeton Instr. 600 gr/mm, BLZ 1 μm	0.67
Silver mirrors inside spectrograph SP2300i (×3)	$0.97 \times 0.97 \times 0.97$
InGaAs Array Princeton Instr. OMA V-512 (512 × 1)	0.86
TOTAL SETUP	**0.22**

3.2.2 Ellipsometry

Ellipsometry is a very sensitive technique for investigating the dielectric properties of thin films, such as refractive index, extinction coefficient and thickness (up to several tens of micrometers).

Ellipsometry works by measuring the change in the polarization of a light beam upon reflection or transmission from the sample under study and comparing it to a theoretical model[162]. In a reflection ellipsometry, for example, a white light beam is linearly polarized and shined on to the sample and the reflected light is collected (see Fig. 3.10). By decomposing both the measured and the incident polarization in s and p component it is possible to measure the complex reflectance coefficients r_s and r_p. Ellipsometry measure the complex reflectance ratio ρ which is defined as follows:

[1]We have employed this objective, optimized for the visible spectral range, for the PL measurements of the $GaAs_{1-x}N_x$ QDs because the objective 378-864-5, optimized for the NIR spectral range, was purchased after the QDs measurements.

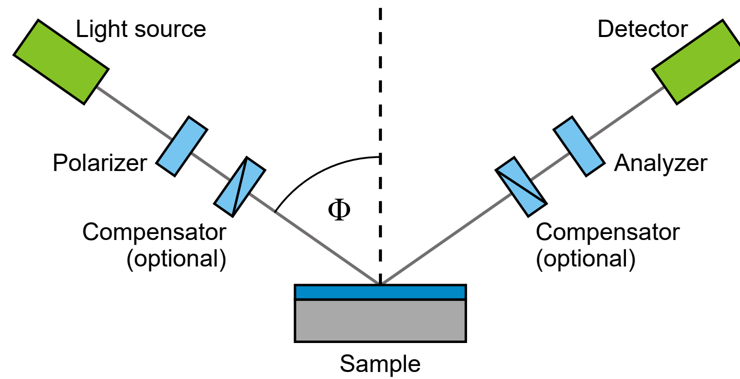

Figure 3.10. Schematic setup of an ellipsometry experiment.

$$\rho = \frac{r_p}{r_s} = \tan(\Psi)e^{i\Delta} \tag{3.2}$$

were Ψ is the amplitude ratio and Δ is the phase difference. These two parameters contain all the information of the sample studied however, to convert them into optical constants, a theoretical model of the system is needed. This can be obtained knowing the structure of the sample and/or the optical properties of the materials composing it. Despite this drawback, ellipsometry has the advantages of being a non-destructive, accurate and reproducible technique.

In this work, ellipsometry (ESM-300 by J.A. Wollam CO., Inc.) was used to measure the thickness of the SiN_x layers on top of the SOI membranes.

3.2.3 Micro-Raman setup

Raman spectroscopy is a multi-purpose spectroscopic technique which relies on the inelastic scattering of photons from the material under study. In solid state physics it is used to characterize materials, measure their temperatures and the eventual presence of strain [163, 164, 165]. It is precisely for this reason that micro-Raman measurements were carried out within this thesis work.

The setup employed is schematize in Fig. 3.11. It consists in a Horiba-Jobin Yvon HR800-UV Raman spectrometer associated with a 1800 lines/mm grating. The system is characterized by a spectral resolution of about 0.5 cm^{-1}. The dispersed signal is then collected with a Jobin Yvon Synapse CCD. The sample are placed on a platform equipped with a $x - y$ translation stage to scan the sample surface and characterized by a spatial precision of about 250 nm. The samples are excited by a He:Ne laser ($\lambda = 632.8$ nm) through a 50× Olympus objective (SLMPLN50X) with NA= 0.35 mounted on an Olympus metallographic microscope. The Raman signal from the sample is collected via the same objective in a back scattering configuration. Thanks to a removable beam splitter it is possible to observe the sample surface with a CMOS camera. With the help of software it is possible to collect raster micro-Raman maps of the sample by synchronizing the movement of the sample with the spectra acquisition. To calibrate the system, before each measurement, a monocrystalline silicon sample is measured.

In this work micro-Raman spectroscopy is used to measure the presence of strain within the flat areas of the samples containing G-centers.

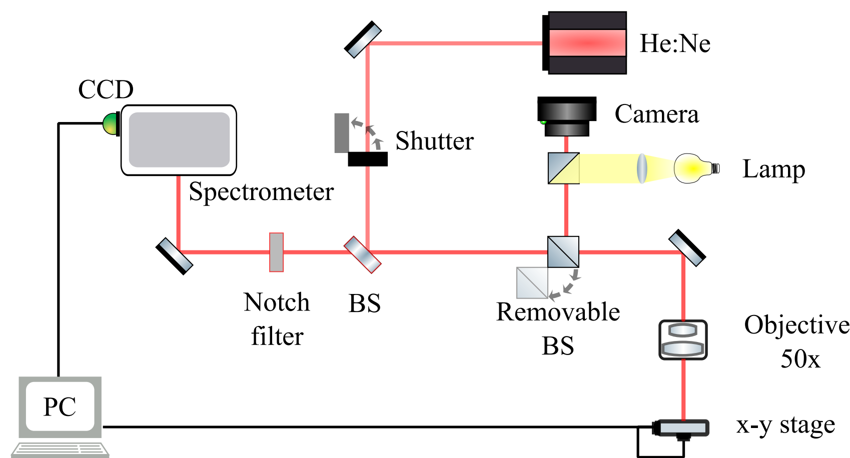

Figure 3.11. Scheme of the micro-Raman setup.

3.3 Simulation techniques and software

3.3.1 Finite-Difference Time Domain simulations

The Finite-Difference Time Domain (FDTD) method is a numerical analysis technique used to evaluate the electromagnetic field in a given region[166]. In the FDTD method the simulated volume is divided in small cubic cells (with a size of the order of several nm^3) and the time-dependent Maxwell's equations are solved within those cells. In detail, the simulation process proceeds as follows: at a given instant in time the electric field vector components are solved within a cell, then the magnetic field components are solved within the same cell but at the next time instant and so on until the end of the simulation time or the reaching of a steady state. However, to properly simulate the fields, their time and space partial derivatives must be evaluated in each time instant and in every cell and this is done using the central-difference approximation.

The FDTD method is a powerful tool which can cover a wide frequency range, being a time-domain method, with a single simulation. Moreover, thanks to its iterative approach it is possible to follow the evolution of the electric and magnetic field instant by instant. However, the discretization of the simulated volume must be fine enough to resolve the smallest geometrical feature of the system thus resulting in long computational times. Moreover, the boundary conditions at the border of the simulated region must be chosen carefully to avoid unwanted artifacts. Despite these problems, FDTD is a robust and accurate method that is widely diffuse and universally accepted as a reliable simulation tool.

In this work the FDTD method was employed using the FDTD 3D Electromagnetic Simulator (version 2020R2.4) from Lumerical Inc. In particular, we exploited it to simulate the formation and the properties of a photonic jet, obtained on the shadow side of a dielectric microsphere illuminated by a plane wave, and to simulate the collection efficiency of the sample containing $GaAs_{1-x}N_x$ QDs as a function of the NA and the emitting wavelength. The latter is calculated simulating an emitting dipole buried in the sample (for further information see Chapter4.2.4). The spectrum of the dipole is selected to be broad enough to cover all the wavelengths of interest. For NA$=1$, the collection efficiency was simply obtained as the ratio between the power emitted in air and the total power emitted by the dipole. While, for NA<1, only a fraction of the total power emitted in air by the dipole

must be consider, i.e. the power emitted in a cone with semiaperture $\theta = \sin^{-1}(\mathrm{NA})$. This value can be easily calculated exploiting a Lumerical function and then, dividing it by the total power emitted by the dipole, we obtain the collection efficiency for a selected NA.

3.3.2 SMUTHI

SMUTHI stands for *Scattering by MUltiple particles in THIn films systems* and it is a Python package for the efficient and accurate simulation of electromagnetic scattering by one or multiple wavelength-scale objects in a planarly layered medium [167]. In detail, SMUTHI exploits the T-matrix method to solve Maxwell's equations in the frequency domain (i.e. one wavelength per simulation). Indeed, once known the T-matrix of each scattering particle in the system all the other quantities can directly computed. This is explained in details in Ref.[167], however the general idea of the process can be easily explained. In a system containing a single scattering particle, the total electric field can be written as the sum between the incident field on the particle, $\mathbf{E}_{inc}$, and the scattered field, $\mathbf{E}_{scat}$. Both fields can be expanded into spherical vector wave functions (SVWF) in particular, the incident field can be expanded in terms of regular SVWF, $\psi_n^{(1)}(\mathbf{r})$, while the scattered field in terms of outgoing SVWF, $\psi_n^{(3)}(\mathbf{r})$. These functions are the two linearly independent set of solutions of the vector Helmholtz equation in spherical coordinates. The two fields can be then written as:

$$
\begin{aligned}
\mathbf{E}_{inc}(\mathbf{r}) &= \sum_n a_n \psi_n^{(1)}(\mathbf{r}) \\
\mathbf{E}_{scat}(\mathbf{r}) &= \sum_n b_n \psi_n^{(3)}(\mathbf{r})
\end{aligned}
\tag{3.3}
$$

where n subsumes the spherical polarization, the multipole degree and order. The T-matrix relates the coefficients of the scattered field to those of the incident field:

$$\mathbf{a} = \mathbf{T}\mathbf{b} \tag{3.4}$$

Therefore, by knowing the incident field and the T-matrix the total electric field is easily computed. SMUTHI computes the total electric and magnetic fields by generalizing this approach to the case of multiple particles in a planarly layered medium.

Thanks to its working principle, SMUTHI has the clear advantage of requiring a fraction of the computational power compared to the mesh-based approach. Indeed, there is no need to define a simulated volume to be subdivided in cells. However, there are some drawbacks such as the limited shapes of scattering particles available and the constriction of having only planarly layered media.

In this work SMUTHI was employed to simulate the properties of the PJs formed illuminating with a plane wave a dielectric microsphere on top of a layered system, to mimic the GaAsN QDs fabrication process. In particular, the PJs properties were studied as a function of the illumination wavelength and the microsphere radius (see Chapter 4.3.1).

3.3.3 Finite Element Method simulations

Finite Element Method (FEM) is an analysis technique for numerically solving partial differential equations (PDE) or integral equations in two or three dimensions. This approach,

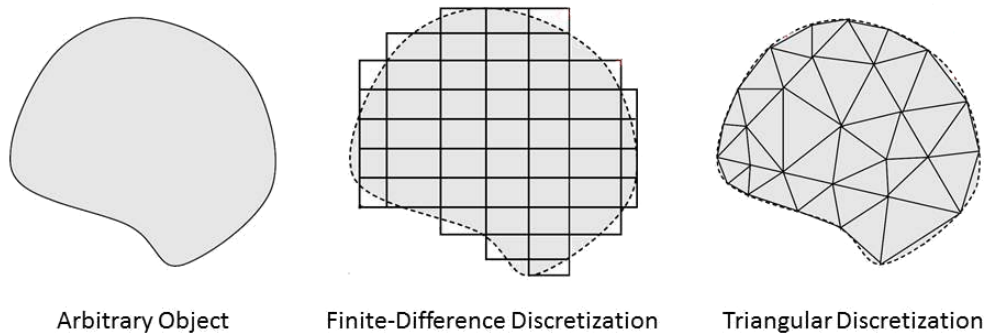

Figure 3.12. Discretization of an arbitrary object in the FDTD and FEM approaches. It is clear that the FEM approach results in smaller errors, without the needing of an excessive fine mesh.

similarly to FDTD, relies on the division of the simulated volume in smaller volumes, called *elements*. However, there are some differences respect to FDTD. First of all, the elements shapes are triangular (in 2D) or tetrahedral (in 3D), which leads to a smaller error in shaping irregular or circular objects to be simulated, as can be seen in Fig. 3.12. Within the elements the equations that locally approximate the PDE are solved and then, recombining all sets of local equations into a global system of equation, the final calculation is performed. The approximation is based on minimizing the errors obtained by locally fitting trial functions into the PDE. This process leads to the elimination of all the spatial derivatives from the PDE, locally approximating them to a set of algebraic equations for steady state problems or a set of ordinary differential equation for transient problems. These sets of equation are then numerically solved to obtain the local solutions. Therefore, FEM can be employed only one for one specific frequency or in steady state conditions.

FEM is a versatile instrument that is used in many different fields from electromagnetism, to heat transfer, to fluid dynamics and to strain studies. Indeed, the approach is always the same, only the equations employed change. In this work FEM was employed to study the strain behaviour within the suspended membranes. In particular, using the commercial software COMSOL Multiphysics® (v. 6.0, `www.comsol.com`, COMSOL AB, Stockholm) we modeled a membrane with a strained silicon nitride layer on top to evaluate the resulting strain within the silicon layer containing the G-centers.

3.3.4 SRIM

SRIM stands for *Stopping and Range of Ions in Matter* and consists in a group of programs which calculate the interaction of ions with matter [168]. The core of SRIM is TRIM, which stands for *TRansport of Ions in Matter*. TRIM is a Monte Carlo simulation software that calculates the interaction of energetic ions with amorphous targets. It relies on some approximations to reduce the computational load while maintaining accuracy. SRIM is used to compute a huge number of parameters relevant to ion beam implantation and ion beam processing of materials.

In this work SRIM was exploited to calculate C^+ and H^+ penetration depths in SOI samples. The former was needed to estimate the G-centers position within the top layer of Si in SOI. Indeed, as previously described in Chapter 2.2, the G-centers are formed by two C atoms and an interstitial Si, therefore knowing the C position translates into knowing the G-centers positions. On the other hand, to realize the G-centers we implanted the samples

with proton (H^+). In this case the only requirement for the implant is that they stop within the SiO_2 layer, to not activate intrinsically formed G-center within the Si substrate. Therefore, SRIM was exploited to simply have an estimation of the energy range for that to happen.

Chapter 4

$GaAs_{1-x}N_x$ Quantum Dots

In this chapter an innovative technique for the fabrication of $GaAs_{1-x}N_x$ QDs will be presented. The technique consists in laser-writing the QDs exploiting the photonic jets realized illuminating dielectric microspheres. The fabricated emitters are then optically characterized and the results of such characterization are thoroughly discussed. In addition, a new set of simulation to further optimize the aforementioned technique will be described.

4.1 The role of photonic jets in the QDs fabrication process

A photonic jet (PJ) consists of a highly intense electromagnetic beam with sub-wavelength lateral extent, which is obtained illuminating a micrometer-sized object with a plane or Gaussian wave. PJs have been observed with a multitude of microparticle shapes, including microcylinders [169, 170], microspheres [171, 172, 48], micro-ellipsoids [173, 174], micro-cubes [175], core-shell microspheres [176, 177] and others [178, 179, 180, 181, 182]. The lateral size of a PJ is typically smaller than the wavelength employed for its formation, down to $\lambda/3$[171]. Moreover, it can propagate for several wavelengths in the surrounding medium in an elongated shape with little divergence.

In this thesis work PJs are used in combination with $GaAs_{1-x}N_x$:H properties to realize QDs. Indeed, as explained in Chapter 2.1, the N-H bonds within $GaAs_{1-x}N_x$:H can be

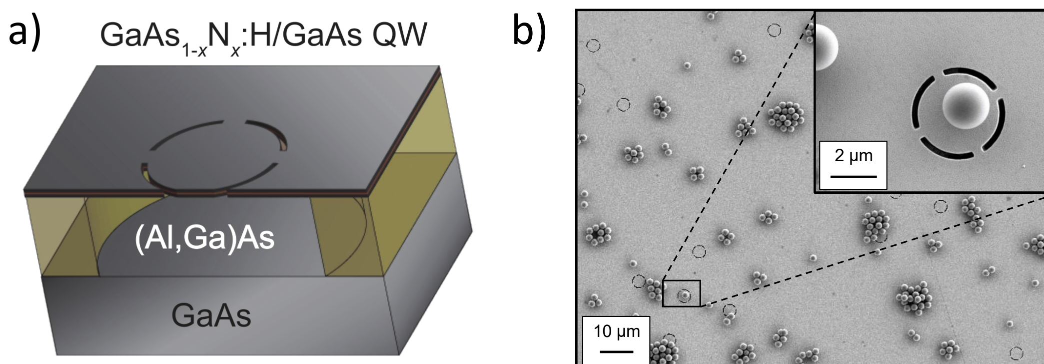

Figure 4.1. a) Sketch of the sample employed to fabricate the $GaAs_{1-x}N_x$ QDs. b) SEM image of the sample after the microspheres deposition. In the inset: magnification of a single microsphere on top of a suspended membrane.

broken, and the H removed, by shining the material with a laser light of proper wavelength. However, to fabricate a QD is needed that the H removal process takes place only in a limited volume of material, to achieve the quantum confinement of the carriers, hence PJs were employed. The idea behind this novel fabrication technique is pretty straightforward: once the microspheres are deposited on the $GaAs_{1-x}N_x$:H/GaAs QW, it is enough to shine them with a laser light to form a PJ beneath them, to break the N-H bonds and remove the H, thus forming the $GaAs_{1-x}N_x$ QDs.

The sample employed for the fabrication of $GaAs_{1-x}N_x$ QDs is described in detail in Chapter 3.1.8. It consists in a fully hydrogenated $GaAs_{1-x}N_x$/GaAs ($x = 0.11$) QW formed by a GaAs upper cladding (30 nm[152]), a 6 nm layer of $GaAs_{1-x}N_x$ and a GaAs lower cladding (130 nm). The QW is realized on top of a $Al_{0.7}Ga_{0.3}As$ sacrificial layer (1300 nm), a GaAs buffer layer (130 nm) and a GaAs substrate. The sacrificial layer was selectively removed to obtain an array of well-separated circular suspended membranes with diameter of 4 µm. As said previously, these suspended membranes have two functions: one, creating a low refractive back reflector due to the mismatch of refractive index between GaAs and air, thus helping the luminescence collection, and two, prepare the sample to the future realization of photonic crystal cavities to be coupled with the fabricated QDs. The membrane thickness (166 nm) was chosen to exclude the presence of any slab waveguide modes of order higher than the fundamental ones (TE0 and TM0) in the wavelength range of interest (about 900 nm). Lastly, a series of SiO2 microspheres (diameter of 2.06 µm) were randomly deposited on top of the sample (see Fig. 4.1). A scheme of the sample is reported in Fig. 4.1, along with a SEM image of the sample surface where we can see the dielectric microsphere randomly placed on top of it. These microspheres are essential for the fabrication technique since they are used to produce the PJ which are then exploited to realize the $GaAs_{1-x}N_x$ QDs in the suspended membranes.

To predict if a PJ with the proper characteristics would form in our sample, we performed 2D simulations with the FDTD method, using Lumerical (see Chapter 3.3.1 for more details). In particular, we simulated the propagation of a plane wave with $\lambda = 532$ nm over our sample, wherein a microsphere was placed on top of a membrane. The selected value of λ should results in a proper photonic jet for the diameter of our microspheres, characterized by a subwavelength profile width. The results of the simulation are shown in Fig. 4.2, which displays the magnitude of the Poynting vector in false colors. As we can see, a nanometric beam of light is indeed created below the microsphere, with an extension of about 266 nm at its FWHM, $\approx \lambda/2$ (see the ×3 magnification and its profile in the insets). The width of the PJ is comparable with the laser spot size of the SNOM system employed to successfully fabricate $GaAs_{1-x}N_x$ QDs in a similar fashion (see Chapter 2.1), hence we proceed to realize the QDs.

The fabrication process proceeds as follows. The sample was mounted on the sample holder of the cryostat to prevent it from unwanted movements. The sample was kept at room temperature and in air (i.e. no vacuum was realized in the cyostat). Then, by scanning the sample surface, we identified the isolated microspheres placed on top of suspended membranes (see e.g. the inset of Fig. 3.6 b). Finally, we centered the microsphere below the objective of our setup (see Chapter 3 for more details) and we shined them using a CW diode-pumped solid state laser at 532 nm for 1 s.

To guarantee the complete illumination of the microsphere, and to best mimic the simulations, the laser light was focused on the sample with a 10× objective with NA = 0.2. The uncertainty in aligning the system was given by the $x-y$ stages and it was about 250 nm.

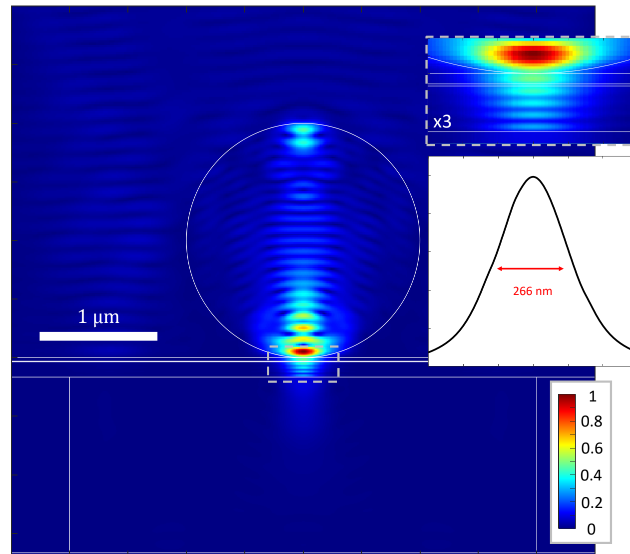

Figure 4.2. Poynting vector magnitude (normalized to the maximum) obtained by an FDTD simulation of our sample with one microsphere on top of a suspended $GaAs_{1-x}N_x$:H/GaAs QW, under illumination with a plane wave (λ = 532 nm). The white lines represent the contour of our sample and the microsphere. The insets show a ×3 magnification of the photonic jet area and its profile.

The illumination time was controlled with an automatic shutter. For more details on the setup employed see Chapter 3.

In order to realize QDs of different sizes we changed the excitation power, ranging from 70 mW to 58 mW in 4 mW steps. Indeed, e.g., employing an higher power would result in breaking the N-H bonds in a wider volume[106] and thus in bigger QDs. The upper power limit was chosen to prevent sample deformations, i.e. membrane collapse, which started to show above 72 mW. That said, it is worth mentioning that the absolute value of the fabrication power depends on the optical system, wavelength, microsphere material and diameter, sample characteristics, etc. Therefore, this power must be calibrated on a sample-to-sample basis, by carrying out a few tests for each QDs fabrication run.

4.2 The characterization of the emitters

Once fabricated, the QDs were characterized by their PL (see Chapter 3 for further details) at low temperature (T = 10 K). Indeed, the carrier confinement in these QDs is not very high and their PL can be observed only up to about 100 K [111, 104] (see Appendix A for more detail). This value varies on the material quality and composition: the QDs fabricated in our material, containing a typical value of 1.1% of nitrogen, show a barrier of about 200 meV in the conduction band and of about 7 meV in the valence band [116, 104].

The measured PL spectra of a series of QDs, fabricated with different fabrication power, are reported in Fig. 4.3a. Clear sharp emissions are observed. The PL spectrum of the QW before hydrogenation is also reported for comparison, as the QW emission energy (about 1.30 eV in our case) represents the lower limit for the QD emission energy. Indeed, if hydrogen is removed from an area large enough to make the quantum confinement effect

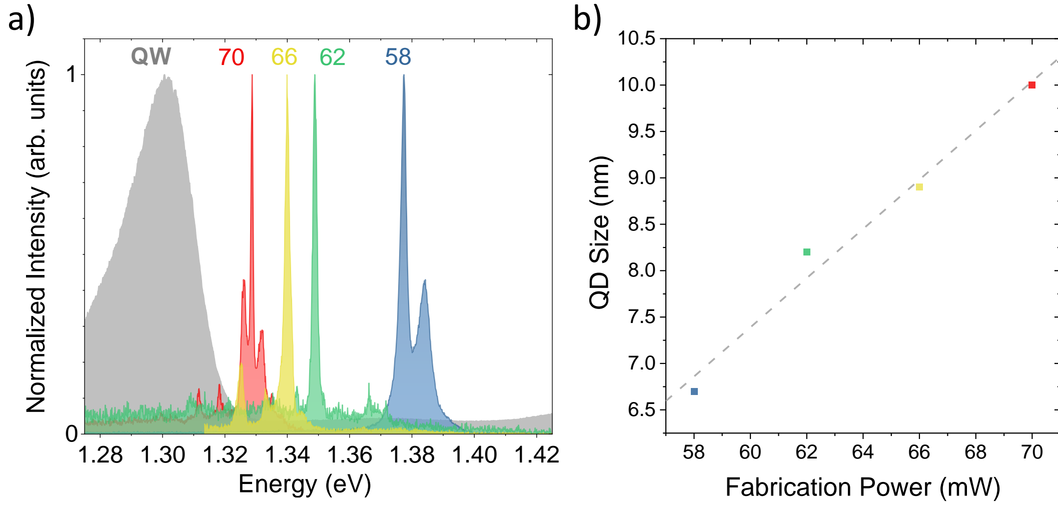

Figure 4.3. a) Micro-PL spectra, measured at 10 K and with an CW excitation power (λ_L = 532 nm) of P_{exc} = 300 nW, of four different QDs fabricated at different fabrication powers, distinguished by colors. The fabrication powers, in units of mW, are provided as labels. The shaded spectrum correspond to the PL spectrum of the $GaAs_{1-x}N_x$/GaAs QW before hydrogenation. b) Size of the QDs (calculated with the model from Appendix B) whose PL is showed in panel a), coloured accordingly. The dashed grey line is only a guide for the eye.

negligible in the horizontal direction, the fabricated QDs approach the QW's behaviour. The upper limit is reached instead when the fabrication power creates a dot so small that its first excitonic energy level is comparable, within few $k_B T$, to the barrier excitonic level. However, it is impossible to directly observe this limit by optical measurements, since the smaller the dot, the lower the PL emitted by it.

The size of the QDs can be estimated, after reasonable assumptions, by using the measured QD emission energy[116]. According to a simple model (see Appendix B for the details of the model), the QD diameters span the range between 10 nm and 6.8 nm, obtained with fabrication powers between 70 mW and 58 mW, respectively (see Fig. 4.3b). While this determination of the QD sizes should only be taken as a rough estimate, the observation of pronounced lateral quantum confinement effects confirms that the diameter of the fabricated QDs must be at least of the order of the size of free exciton, which in $GaAs_{1-x}N_x$ is less than 10 nm [52]. This proves our ability to remove hydrogen from an area much smaller than the diffraction limit by employing PJs. It seems surprising that the QD diameter ($\approx$ 10 nm) is much smaller than the FWHM of the photonic jet ($\approx$ 250 nm) and that only one QD is formed within the jet. However, the power profile of the photonic jet is Gaussian, and H is only removed from the central portion of the beam, where the power density is above a certain threshold. Outside of this region, which can be considerably narrower than the beam's FWHM, there is a much lower probability of forming QDs.

For each fabrication power, we measured several nominally identical QDs obtaining a spread of the central QD-emissions with a FWHM value of about 40 meV. This inhomogeneous broadening is related to many factors: fluctuations in the optical properties of the individual microspheres and of the sample surface give rise to variations in the photonic jet shape; since the H removal process has also a thermal component[106], local variations in the heat dissipation efficiency of the material (due, for example, to the positioning of

the microsphere with respect to the circular apertures opened in the suspended membranes, see Fig. 3.6b) influence the H removal; finally, fluctuations of thickness, and N and H concentrations in the starting QW put a lower limit for the inhomogeneous broadening of the QDs. Considering that the QW emission shows a 30 meV broadening (see Fig. 4.3), this factor is likely to predominate over the others, leading to the conclusion that an improvement of the quality of the QW would be crucial to significantly lower the QD inhomogeneous broadening.

It is interesting to calculate the minimum inhomogeneous broadening of an ensemble of nominally identical QDs. Assuming a perfectly flat QW and a perfect fabrication process, the minimum inhomogeneous broadening is due to N concentration fluctuations. Given a generic volume V, since the fluctuations of the nitrogen atom number are expected to be Poissonian, the expected standard deviation of x is $\sigma_x = \sqrt{xM/(\rho V N_\mathrm{A})}$ where ρ is the mass density of the material, M is the molar mass, and N_A is the Avogadro constant. Considering a typical QD volume of about 600 nm^3, we obtain $0.0093 < x < 0.0111$, which gives a variation of the $GaAs_{1-x}N_x$ band gap[183] of about ±7 meV. Therefore, at least at the leading order, the minimum QD inhomogeneous broadening corresponds to a FWHM of about 16 meV.

The intensity of the main line of our QDs shows a large range of variation. An upper limit for the overall efficiency of our system can be given using the tabulated data for all the elements of our setup (see Chapter 3). According to the reported data, the efficiency can be estimated to be about 4% at 930 nm. Using this value, we can estimate the lower limit for the rate of emitted photons impinging on the first lens, i.e. the brightness of our emitters. The reported value is obtained integrating over the emission line of the QD. At the saturation power, under CW excitation, and in presence of the microsphere, the brightness ranges between $0.2 \times 10^6\,\mathrm{s}^{-1}$ and $5 \times 10^6\,\mathrm{s}^{-1}$. This large variation is likely mainly due to the different concentration of non-radiative defects in proximity of the QD. It is interesting to note also a trend of the luminosity with emission energy: the higher the emission energy, the smaller the dot, the lower the luminosity. This phenomenon is compatible with our hypothesis: due to the higher surface to volume ratio for smaller QDs, the influence of non-radiative defects surrounding the QD is larger.

4.2.1 Identification of the QD emission lines

In order to identify the origin of the different transitions observed in the PL spectra of each QD, we studied the evolution of their integrated intensity as a function of the CW excitation power. Indeed, according to a Poissonian model for the level occupation probability[184], the integrated intensity, I_PL, of the exciton (X) and biexciton (XX) PL line is described by:

$$I_\mathrm{PL} = C(aP^b)^n e^{-aP^b} \tag{4.1}$$

where, to take into account the different filling dynamics, $n = 1$ for X and $n = 2$ for XX, P is the excitation power, and a, b and C are three constants. The average number of excitons present in the QD at a given power, $\langle n \rangle$, is given by aP^b. It has been proved experimentally [184] that Eq. (4.1) can also describe the behaviour of a charged exciton (X^*), provided that $n = 1.5$.

Fig. 4.4 summarizes the power dependence of the PL spectra of two QDs, whose main emissions are at 1.336 eV (QD1) and at 1.386 eV (QD4), respectively. Three selected spectra

are reported for each QD in Figs. 4.4a and 4.4c, whereas Figs. 4.4b and 4.4d include the integrated intensity of the main peak as a function of the excitation power (black dots)

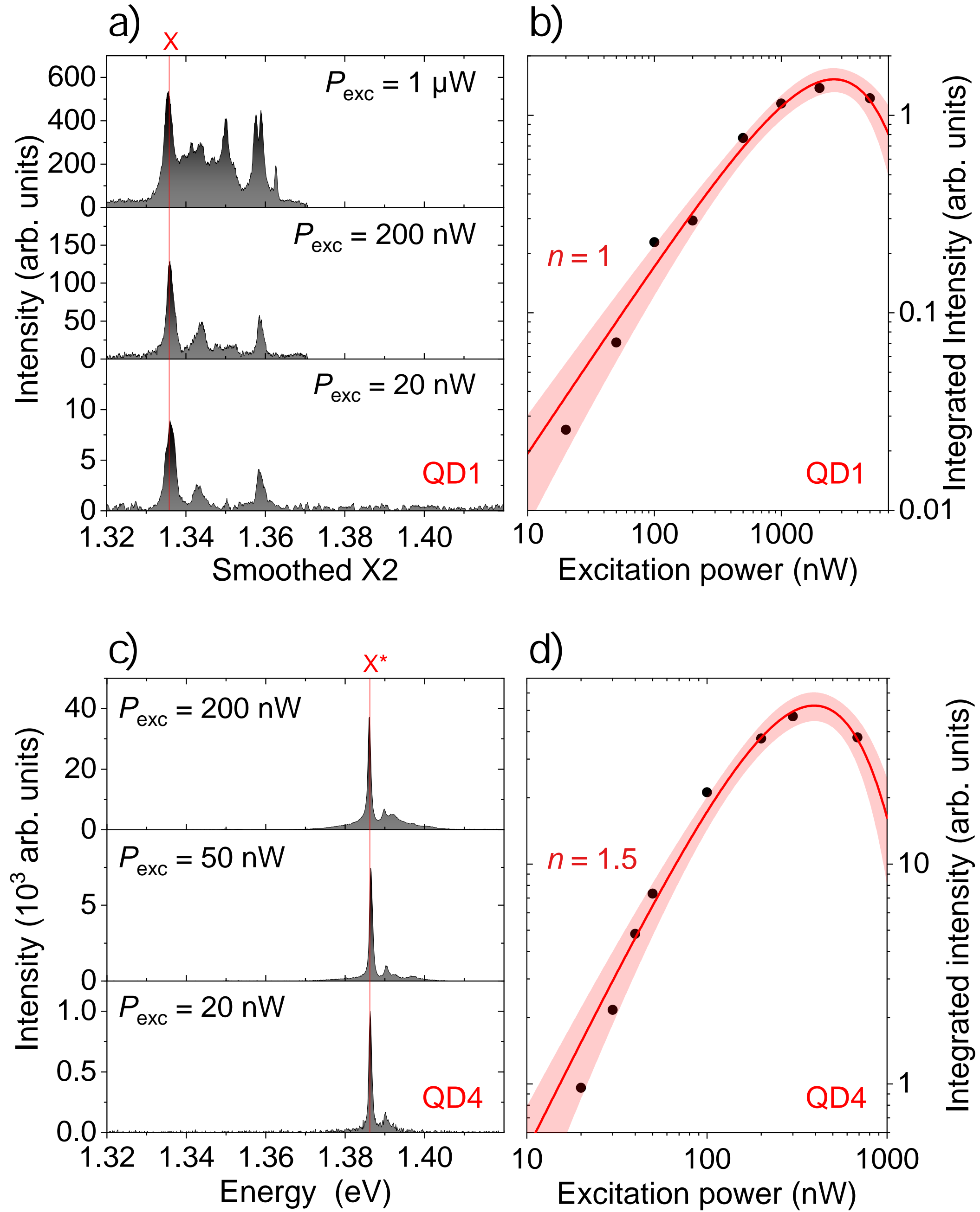

Figure 4.4. a) and c) display selected PL spectra acquired at 10 K on two different QDs, labeled QD1 and QD4, at different CW excitation powers. b) and d) show the integrated intensity of the main transition of the two QDs, highlighted with a semitransparent red line in panels a) and c), as a function of the excitation power. Eq. (4.1) is used to fit the experimental data (black dots), yielding the red lines shown in the figure (the filled areas represent the 95% confidence bands). These fits allow us to identify the main transitions of QD1 and QD2 as an exciton (X, n = 1) and as a trion (X^*, n = 1.5), respectively.

and the fits (red lines) obtained with Eq. (4.1). The parameter n is fixed before the fitting procedure, it can assume only the value 1, 1.5, 2 and it is chosen in order to obtain b as close as possible to 1.

The results of the fit show that the main QD1 peak can be associated with an exciton (X), and the QD2 peak with a charged exciton (X^*). The fitting parameters for the two QDs are: $n = 1$, $a = (5.1 \pm 1.9) \times 10^{-4}\,\mathrm{nW}^{-b}$, $b = (0.96 \pm 0.05)$, and $n = 1.5$, $a = (2.0 \pm 0.6) \times 10^{-3}\,\mathrm{nW}^{-b}$, $b = (1.11 \pm 0.05)$, respectively. As speculated in similar III-V QDs [185], a possible explanation to the narrower linewidth of the X* ($\approx 900\,\mu$eV compared with the ≈ 2 meV of the X) cold be the reduction in the quantum confined Stark effect resulting from the presence of the spectator charge, which screens the QD from the fluctuations of the external field that surrounds it.

From the fitting results it is also possible to evaluate the saturation power, P_s, for both QDs. Indeed, Eq.4.1 has a maximum for $\langle n \rangle = aP_s^b = n$ and thus: $P_s = 2689$ nW for QD1 and $P_s = 389$ nW for QD4.

The saturation power under CW excitation multiplied by the ratio between the exciton lifetime and the laser repetition rate gives an estimate of the saturation power under pulsed excitation regime.

Knowing the nature of the emission and its saturation power, the capture volume (V_c) of the QDs, a good proxy for their quality, can be estimated. $\langle n \rangle = V_c G \tau$, where G is the e-h pair generation term and τ is the e-h pairs lifetime, which in our case is about 2 ns. At saturation the capture volume results $V_c = n/(G_s \tau)$.

Considering the GaAs absorption coefficient at 532 nm, $\alpha = 7 \times 10^4\,\mathrm{cm}^{-1}$, a spot area $A = 1\,\mu\mathrm{m}^2$ (with NA = 0.7 the photonic jet is very broad[85]), and the photon energy at $E_{ph} = 2.33$ eV (corresponding to a wavelength of 532 nm), we can estimate $G_s = \alpha P_s/(A E_{ph})$. Substituting the saturation powers for QD1 and QD4, we finally obtain $V_c = 15 \times 10^3\,\mathrm{nm}^3$ and $V_c = 102 \times 10^3\,\mathrm{nm}^3$ for QD1 and QD4, respectively.

Assuming a cylindrical geometry for the QDs, with a height $L = 6$ nm and a diameter $2R = 10$ nm and $2R = 7$ nm for QD1 and QD4, respectively, we can estimate the capture length, L_c, considered constant all around the nanostructure. We find $L_c = 10$ nm and $L_c = 25$ nm for QD1 and QD4, respectively, values similar to (or larger than) the QD size, indicating the good quality of the material. In particular, the larger value obtained for QD4 indicates its better quality with respect to QD1, probably due to a different environment with smaller defects concentration, which explains also the different linewidths of the emissions.

4.2.2 Time-resolved PL measurements

We have then performed time-resolved PL (TRPL) measurements on the emissions of our QDs. As an example, Fig. 4.5 shows the TRPL measurement of QD1 emission. The fits (blue and red curves) were performed with a single (blue curve) and a double (red curve) exponential, respectively, convoluted with a Gaussian. The Gaussian curve models the impulse response function of our system (FWHM = 400 ps).

The double exponential perfectly fits the data, consistently with other cases reported in the literature for GaAsN QDs (see, e.g. Ref. [109], although for the sake of completeness we must mention that a second QD, correctly described by a single exponential, is also reported in that work). The time constants of the double exponential obtained from the fit are: $\tau_1 = (3.08 \pm 0.06)$ ns and $\tau_2 = (0.67 \pm 0.03)$ ns. While, the single exponential provides an average time constant, which results in a value of $\tau = (2.00 \pm 0.05)$ ns.

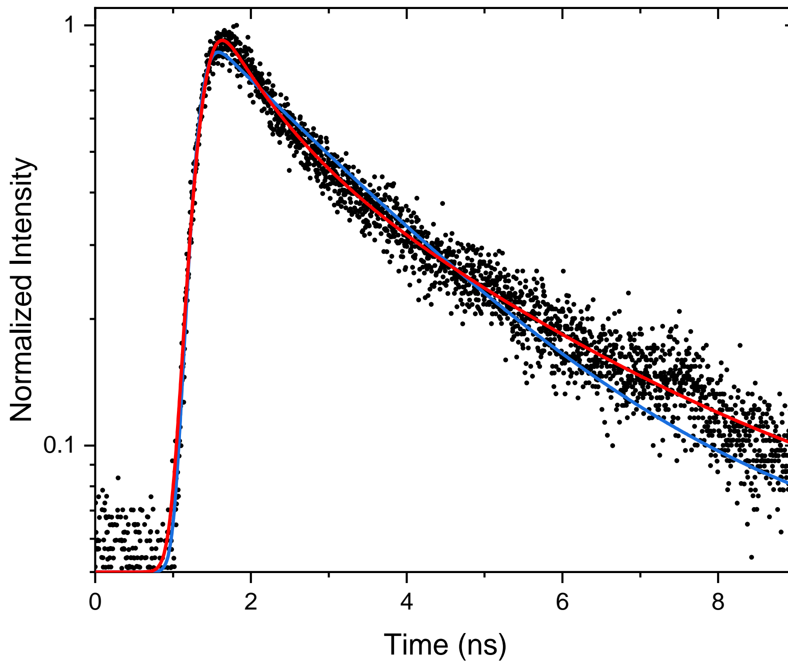

Figure 4.5. Time-resolved micro-PL measurements of the QD excitonic emission (black dots). The blue (red) curve represents the fit of the experimental with a function formed by a single (double) exponential convoluted with a Gaussian (system impulse response). The single exponential fit gives a value of the exponential time constant of $\tau = (2.00 \pm 0.05)$ ns, while the one with a double exponential gives $\tau_1 = (3.08 \pm 0.06)$ ns and $\tau_2 = (0.67 \pm 0.03)$ ns.

The same measurement were performed on several other QDs. Each one was fitted either with a single o double exponential accordingly to which function would better approximate the data. The values of the decay constants obtained range between 0.5 and 3 ns. These values can be used to have a rough estimate of the maximum brightness achievable by our QDs. Indeed, the decay constant is directly related to the radiative recombination time and thus to the rate of the photons emitted by the QD. Therefore, the brightness achievable by our QDs can easily reach hundreds of MHz. It is worth noting that embedding the QDs within a photonic crystal cavity could greatly decrease the radiative lifetime, thanks to the Purcell effect, and thus increase the maximum achievable brightness.

4.2.3 The second order autocorrelation function

In order to test the ability of these QDs to emit single photons, we measured their second-order autocorrelation function, $g^{(2)}(\tau)$. In Fig. 4.6a we report the CW PL spectrum of QD1, while in Fig. 4.6b we display the $g^{(2)}(\tau)$ relative to the exciton (X) emission line of the same QD, under pulsed excitation regime. It is to be noted that, in order to improve the signal to noise ratio, a relatively high power (400 nW, about 90% of the saturation power in pulsed excitation regime) was employed for these measurements (PL spectra could be acquired for excitation powers as low as 20 nW, as shown before). Even though this certainly worsens the single-photon purity, the raw value of $g^{(2)}(\tau)$ at zero delay ($\tau = 0$) is about 0.25, much lower than 0.5, showing the single-photon emitter nature of the QD.

The $g^{(2)}(\tau)$ was fitted with a curve (reported as a solid red line in Fig. 4.6b) based on the

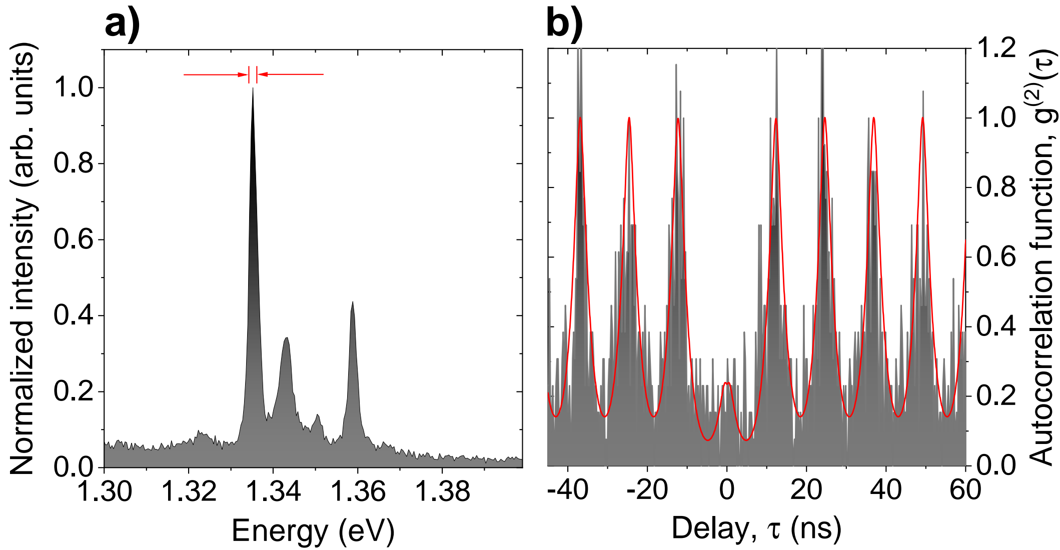

Figure 4.6. a) PL spectrum of QD1 acquired at 10 K and with a CW excitation power of 100 nW. The interval indicated by two red arrows represent the spectral range ($\sim$ 2 meV) used for the measurement of the second order autocorrelation function, $g^{(2)}(\tau)$. At the saturation power, with the microsphere on top, and under CW excitation, the photons per second impinging on the first lens are about $0.3 \times 10^6\ s^{-1}$. b) $g^{(2)}(\tau)$ acquired at $T = 10$ K and with a pulsed excitation power of 400 nW, just below the saturation power, (dark histogram), and its fit (red line) with the model described in Appendix C. It is clear that the $g^{(2)}(0) < 0.5$, confirming the single photon emitter nature of this QD.

solution of a system of rate equations developed by taking into account the main processes leading to the capture, relaxation and recombination of carriers in and out of the QD (for a more detailed description of the model see Appendix C[111]). Moreover, a term describing an uncorrelated background can be added to the model. The fit yields a carrier capture time $\tau_{cap} \approx 0.3$ ns, for both electron and hole, and a recombination time $\tau_{rec} \approx 1.84$ ns, in agreement with $\tau_{rec} \approx 2$ ns obtained through time-resolved PL measurements considering a single exponential decay. Indeed, the model describes the decay of the QD with a single exponential and adding another free parameter would clearly give an overfitting of the curve, considering the noise present in the autocorrelation data. Indeed, the resulting value of the uncorrelated background results to be about ~ 20 % of the measured coincidences, consistent with the broad emission overlapping with the QD line under consideration. Finally, the value of $g^{(2)}(0)$, obtained by the fit and due only to the QD line without the uncorrelated background, is less than 0.1.

Once the measure of $g^{(2)}(0)$ for a QD is available, it is also possible to correct the number of emitted photons per second by the factor $\sqrt{1 - g^{(2)}(0)}$ in order to eliminate the counts originated from multiple photon emissions[186]. For example, the QD1 generates, in pulsed excitation regime at saturation power, 0.6×10^6 photons/s impinging on the first lens. Correcting for the factor above, we obtain 0.5×10^6 single-photons/s. By dividing this number for the laser repetition rate (82 MHz), we obtain that QD1, when coupled with a microsphere, sends towards the collection optics 1 single photon every 164 laser pulses (0.6% of the total). This value is far from the ideal scenario where a relation 1 on 1 exists between laser pulses and single photons emitted. Several factors contribute to keep this

value low: the detection efficiency of 4% is an upper limit estimate; the probability of having multi-photon emission from the QD (see above) has been considered; theoretical predictions are very sensible to small variations of the model; and especially many other non-radiative, as well as radiative (e.g. the free-exciton recombination from bulk GaAs, other excitonic species in the QD), recombination channels are present in our system and therefore not every laser pulse results in the emission of a single photon from the QD.

4.2.4 Evaluation of the collection enhancement

After demonstrating the possibility to "laser write" $GaAs_{1-x}N_x$ QDs, we verified another "optical advantage" that the presence of the microspheres brings to the table, i.e. the collection enhancement.

The best way to compare different approaches used to out-couple the radiation from an emitter is to give the percentage of the radiation extracted into the air and the shape of the emission pattern (see e.g. Table1.3). Simply giving the percentage of collected luminescence is useful to set a world record but not to properly give the information about the potentiality of a technology, without considering the fact that sometimes is reported the percentage of collected luminescence with respect to that extracted into the air, not with respect to the total emitted. The collection enhancement, instead, is a useful number to compare technologies consisting in objects that can be inserted between the collection optics and the emitting objects (SILs, microspheres). It is defined as the ratio between the collected power with the microsphere over the collected power without the microsphere.

Using FDTD simulations, both the collection efficiency and the collection enhancement of our sample were estimated for several values of NA (see Chapter 3.3.1 for further details). We considered a dipole buried 33 nm below the surface of our sample (corresponding to the center of the $GaAs_{1-x}N_x$:H/GaAs QW) and with the polarization axis parallel to the sample surface. Our QDs can be approximated as cylinders with diameter larger than their height, which implies a larger probability of having the dipole axis parallel to the sample surface[187]. This condition gives higher collection efficiencies, as well as a higher collection enhancement (simulations not shown). As the one shown in Fig. 4.2, the simulations were performed considering the geometry and the optical properties of our sample. The results of our simulations as it concerns the estimated collection efficiency and enhancement are shown in Fig. 4.7a and 4.7b. As shown in Fig. 4.7a, the percentage of light emitted in air (towards the collecting optics) by the dipole is higher with respect to the simple case of semi-infinite substrate (2%[40]), even without the microsphere. This is easily explained by the small thickness of the membrane with respect to the emitter wavelength and by the back reflection due to the GaAs/air interface. By simply doing the ratio between the collection efficiency with and without the microsphere on top, the collection enhancement is obtained, and it is reported in Fig. 4.7b. This enhancement is the result of the combination of three different physical phenomena[85]: a small Purcell effect (≈ 1, negligible in our case); the reduction of light lost by total internal refraction (TIR) due to near-field coupling between the GaAs and the microsphere (red curve); an increase in the directionality of the emission. The Purcell factor and the near field coupling are NA-independent and their combined effect can be observed looking at the NA = 1 curve. While the increase in the directionality of the emission can be observed for NA < 1 and its contribution becomes more important reducing the NA, for NA = 0.1, in particular, resonances are observed with a corresponding collection enhancement surpassing 90 times.

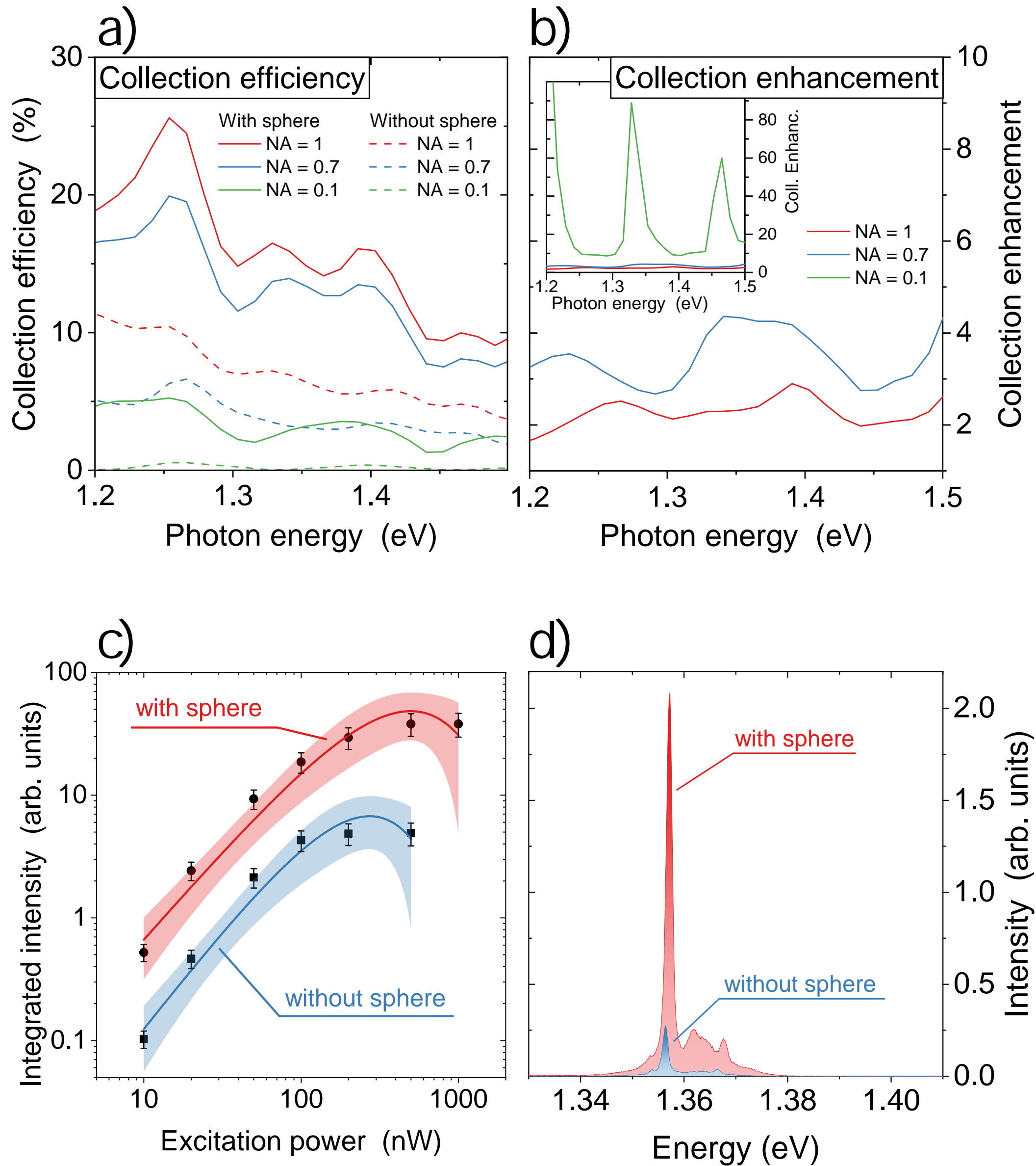

Figure 4.7. a,b) FDTD simulations of the luminescence collection efficiency and luminescence collection enhancement associated with the presence of a dielectric microsphere for different NAs. The inset in b) has a different scale on the vertical axis in order to show the NA = 0.1 curve. c) Integrated intensity at 10 K of the main transition (X) of a QD (labeled QD2) with a sphere on top (circles) and after sphere removal (squares), as a function of the excitation power. At the saturation power, with the microsphere on top, and under CW excitation, the photons per second impinging on the first lens are about $4 \times 10^6\ \mathrm{s}^{-1}$. The solid lines are the best fits with Eq. (4.1) (the filled areas represent the 95% confidence bands). The CW spectra at $P = 500\,\mathrm{nW}$ are reported in panel d) for comparison. It is worth noting that, as shown in panel b), the predicted collection enhancement for NA = 0.7 at 1.357 eV is 4.3 while the experimental value obtained from the ratio of the intensities of the two fitting curves at their saturation power is 7.3. The difference is attributed to sensitivity of the simulation results to the initial conditions (see text).

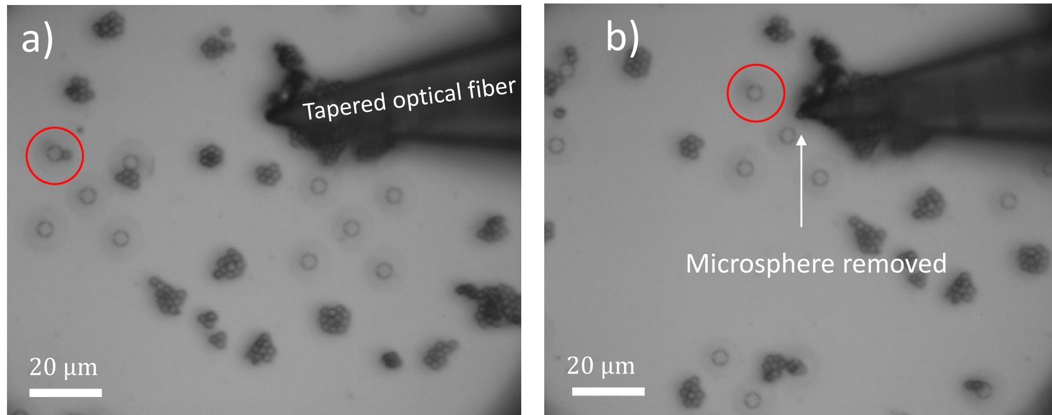

Figure 4.8. Microsphere removal process. a) Optical microscope image of the tapered fiber near the sphere to be removed. b) Optical microscope image of the microsphere removed. The microsphere is attached to the fiber likely due to Van Der Waals interactions.

In order to experimentally measure the collection enhancement, first we measured a QD (labeled QD2) with a sphere on top, and then after removing the sphere. The sphere was mechanically wiped away by a tapered optical fiber with a tip of about 200 nm (SNOM tip) mounted on translation stages. In Fig. 4.8 there are the images of the sample surface before and after the sphere removal. As it can be seen, the membrane is completely unaffected by the fiber, moreover the microsphere remains attached to the tapered fiber likely do to Van Der Walls interactions. Since the presence of the sphere can influence not only the collection but also the excitation power per unit area, PL spectra at 10 K, before and after the sphere removal, were acquired as a function of the excitation power. Indeed, the saturation power corresponds to an identical excitation condition, allowing to compare the intensities. The integrated intensity as a function of the excitation power for QD2, with the main excitonic peak at 1.357 eV, before and after sphere removal are reported in Fig. 4.7c. Fitting Eq. (4.1) to the data results in the solid lines of Fig. 4.7c. The ratio of the intensities of these two curves at the saturation power gives the collection enhancement, equals to 7.3 ± 0.7 (1 standard deviation).

The value predicted by FDTD simulations for NA = 0.7 at 1.357 eV (see Fig. 4.7b) is 4.3. The difference between these two values can be attributed to the unstable behaviour of the simulations: large differences in the simulation results are obtained even with small changes of the simulation conditions. In this respect, it is important to note that the simulations assume ideal fabrication parameters, which might deviate significantly from the real ones; just to make an example, the assumption of perfect, mirror-like GaAs/air interfaces is clearly unrealistic, especially given that the lower surface was obtained by chemical etching. This could easily result in an overestimate of the collection efficiency of the suspended GaAs membrane in the absence of the microsphere and, thus, in an underestimate of the collection enhancement due to the latter.

For the sake of completeness, in Fig. 4.7d we have reported the PL spectra of the QD before and after the sphere removal with an excitation power as close as possible to the saturation power. The enhancement of the collected signal is clearly observed. Moreover, it is worth mentioning that the change in the full width at half maximum (FWHM) of the main peak results within the spectral resolution of the system: $\mathrm{FWHM_{with}} = 1.41$ meV

and $FWHM_{without} = 1.29$ meV. Therefore, neither the presence of the microspheres nor its removal worsen the spectral properties of the emitters.

Finally, in order to investigate the physical origin of the collection enhancement, which, as explained above, should be mainly due to an improved directionality of the emission, we measured the angular distribution of the emission of a QD (labeled QD3), with a microsphere on top, whose spectrum is reported in Fig. 4.9a. The normalized angular emission pattern in k-space is reported in Fig. 4.9c. Analogously, we reported in Fig. 4.9b and 4.9d the spectrum and the normalized angular emission pattern in k-space of the $GaAs_{1-x}N_x$/GaAs QW before hydrogenation: this measurement was performed to mimic a point-like emission (like a QD) without a microsphere on top (without the sphere, the detected QD emission was too weak to perform k-resolved measurements; in and by itself, this is a testament to the effectiveness of the microspheres in improving the collection efficiency). It is clear that the angular distribution of the emission without the microsphere is much broader than that with the microsphere. The effect of the microsphere, as explained above, is to increase the directionality of the emission of the emitters placed below it. This result is more clearly observed looking at the profiles of the angular emission patterns of Fig. 4.9c and 4.9d. Cutting these two experimental maps along a direction passing through the center of the emission, and averaging against all possible directions, the profiles reported in Fig. 4.9e are obtained (blue circles and red squares). In order to compare these profiles against the theoretical expectations, we simulated the same system described above and we considered the far field pattern as a function of the emission angle – with and without the presence of the microsphere – obtaining the curves displayed in Fig. 4.9e as solid lines. Comparing the curves, a clear agreement is found.

Furthermore, from the k space maps we can obtain an evaluation of the precision of our fabrication technique in terms of lateral misplacement of the QD respect from the axis of the microsphere. To do so, it is relevant to note that an in-plane misalignment of the QD with the point contact of the sphere on the sample surface would result in an angular shift of the emission. To evaluate the shift we have performed a series of FDTD simulation consisting in a plane wave hitting a microsphere at different angles, as it can be seen in Fig. 4.10. From the simulations it results clear that the PJ produced can be rigidly shifted by tilting the incident plane wave. Measuring the PJ position as a function of the incident angle, we find a constant shift of 17 nm/°. Analogously, the reverse condition, the tilt of the beam originating from a QD at different distances from the sphere contact point, must give the same value of 17 nm/°, by Helmholtz reciprocity principle. To verify that we have consider a simple geometrical model, sketched in Fig. 4.11, in which we consider a QD placed in an off-axis position under the microsphere[85]. The position of the QD is labeled by the coordinates (x, y), where the $(0, 0)$ position is in axis position (i.e. the contact point of the microsphere). The coordinates of the QD are directly connected to the $k-$space coordinates by the formula:

$$\begin{aligned} x &= -r\,(k_x\lambda\!\!\!^{-})\left(1-(k_x\lambda\!\!\!^{-})^2-\left(k_y\lambda\!\!\!^{-}\right)^2\right)^{-1/2} \\ y &= -r\left(k_y\lambda\!\!\!^{-}\right)\left(1-(k_x\lambda\!\!\!^{-})^2-\left(k_y\lambda\!\!\!^{-}\right)^2\right)^{-1/2} \end{aligned} \tag{4.2}$$

where r is the microsphere radius and $\lambda\!\!\!^{-}$ is the vacuum wavelength of the QD divided by 2π. The displacement d between the microsphere and the QD can be calculated as $d = \sqrt{(x^2 + y^2)}$. However, in the condition of small angles it can be drastically simplified,

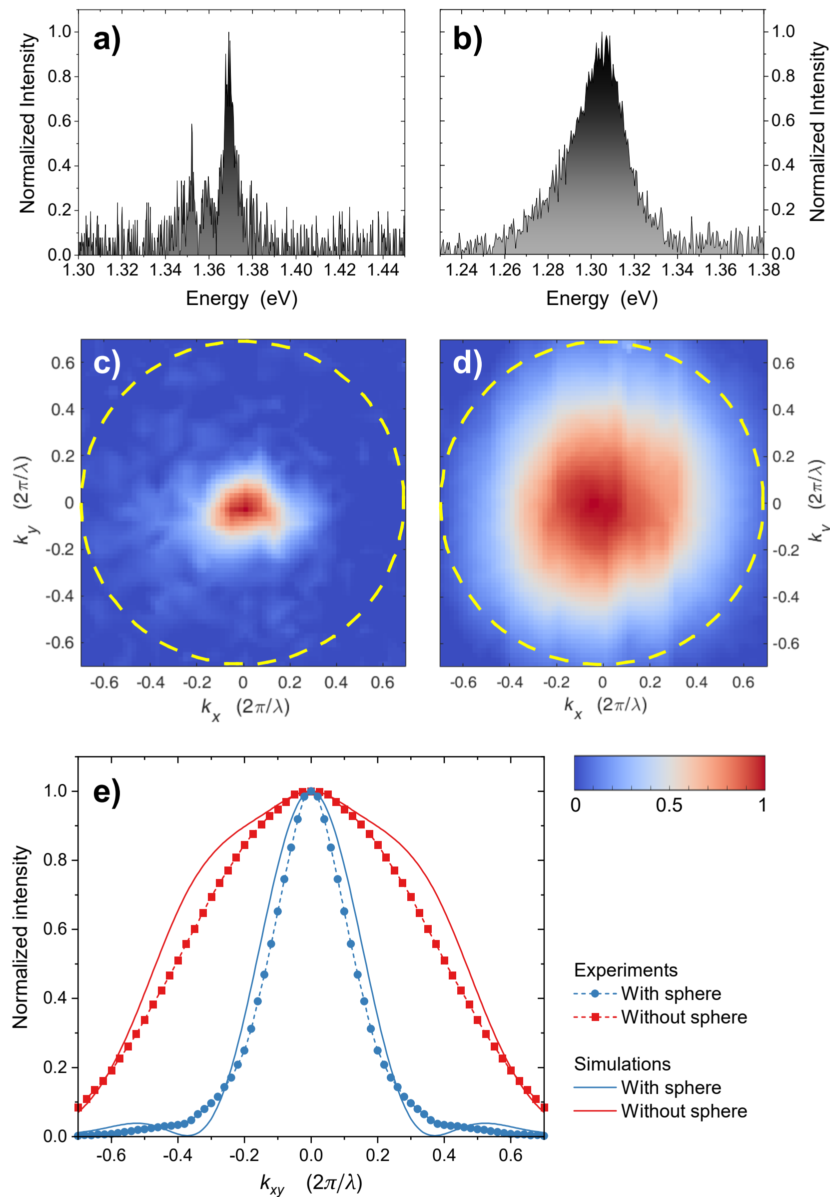

Figure 4.9. a,b) PL spectra of a QD (labeled QD3) under CW excitation, with a microsphere on top, and of the GaAsN/GaAs QW before hydrogenation, without a microsphere on top, respectively. These spectra correspond to the center of the maps reported in c) and d), respectively. c) PL angular emission map of the emission of the QD3 with a microsphere on top ($T = 10$ K, $P_{\mathrm{exc}} = 300$ nW, energy interval 1.362–1.376 eV). The yellow dashed circle represents the NA (NA = 0.7) of the objective used. d) PL angular emission map of the QW signal without a microsphere on top ($T = 10$ K, $P_{\mathrm{exc}} = 400\,\mu$W, energy interval 1.290–1.317 eV). The yellow dashed circle represents the NA (NA = 0.7) of the objective used. This measurement was performed to mimic a point-like emission without a microsphere. e) Experimental angular profiles (blue circles and red squares) extracted from the maps in panel c) and d), respectively, by a proper radial average. These data are compared with FDTD simulated angular profiles (blue and red solid lines) of emitters (emitting at 1.37 eV and 1.305 eV) with and without a microsphere, respectively, buried in GaAs 33 nm below the surface.

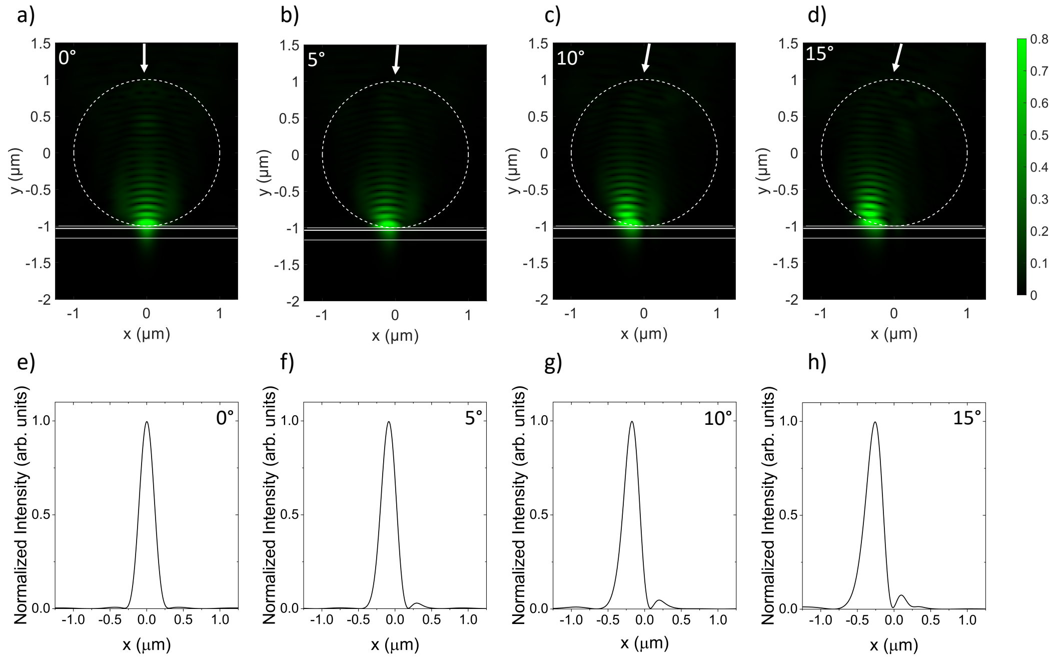

Figure 4.10. a), b), c) and d) display FDTD simulations of a series of PJs. They are obtained illuminating a dielectric microsphere with a plane wave (λ = 532 nm) at different incident angles, indicated by an arrow. The angle is measured clockwise with respect to the normal to the plane and its value is indicated on top of each panel. The white solid lines represent the contour of the sample while the dashed line represents the microsphere. e), f), g) and h) show the profiles of the photonic jets obtained within the QW for the incident angle displayed in a), b), c), d), respectively. Analyzing the peak position as a function of the wave incident angle, we obtain a shift of 17 nm/°.

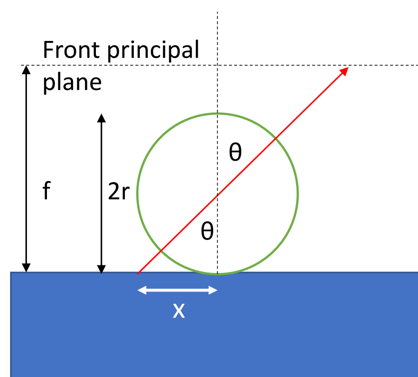

Figure 4.11. Sketch of the system where are reported the quantities and the geometrical configuration used to perform the ray-optics transformation from $k-$space to position space (and vice versa). The sketch is not on scale.

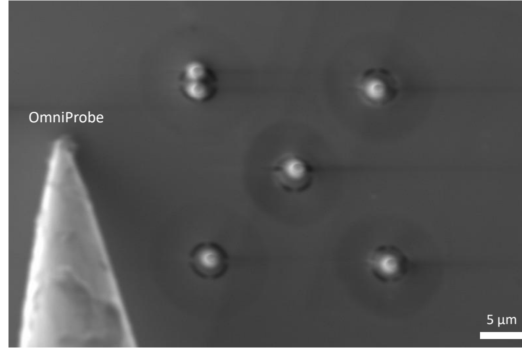

Figure 4.12. SEM image of some spheres positioned on top of the suspended membranes.

indeed $d = r\theta$, where θ is the emerging beam angle in radians. Therefore, with θ in degrees (°) and $r = 1000$ nm, we obtain $d = (17.45\,\text{nm}/°)\,\theta$, in good agreement with the simulations showed in Fig. 4.10. This value can be also read as: the QD emission is tilted of 0.059 ° per nm of misalignment. From Eq. 4.2 and the estimated precision in determining the central point in k space ($\sigma_k/(2\pi/\lambda) = 0.02$) and the estimated precision in determining the center of the emission ($\sigma_k/(2\pi/\lambda) = 0.02$), we can therefore estimate that the QD-sphere alignment is, at 1 standard deviation, ±30 nm, highlighting the power of our approach. As a final remark, it is worth noting that it would be possible to fabricate sphere-misaligned QDs via tilted illumination, obtaining a deterministic beam steering of the quantum emitters.

4.3 Summary and future developments of the technique

To summarize, we have demonstrated the possibility to create $GaAs_{1-x}N_x$ QDs exploiting PJ to locally tune the hydrogen content in dilute nitrides. This fabrication method inherently ensures a near-perfect (±30 nm) spatial alignment between the QD and the microsphere used to generate the PJ, thus leading to the maximization of the broadband enhancement of the collection efficiency (×7.3) for the light emitted by the QD. This technique has other several advantages: the fabrication is performed at room temperature, in air and without any lithography or etching procedure; it is low-cost with respect to most QD fabrication techniques; the emission can be tuned over a range larger than 200 meV controlling the hydrogen removal[116]; it is, in principle, possible to cover both telecommunication wavelength windows by tuning the nitrogen concentration and/or by introducing indium in $GaAs_{1-x}N_x$; the QDs are rewritable, since the fabricated nanostructures can be erased and rewritten multiple times, simply by re-hydrogenating the sample and by repeating the fabrication process.

Despite the several advantages, there are some issues, such as the large homogeneous broadening of the emission (≈ 1 meV), the limited brightness, the lack of control over the microspheres deposition and the inhomogeneous broadening of the emission energy of nominally identical QDs (40 meV). In our opinion, most of these problems can be potentially solved in a straightforward manner: as far as the large QD linewidth is concerned, the broadening is likely linked to surface defects [188], and can thus be reduced by growing a thicker capping layer on top of the $GaAs_{1-x}N_x$:H/GaAs QW (from the simulations we observe that the photonic jet keeps a narrow waist for nearly 1 µm when propagating in

bulk GaAs). Moreover, this would contribute also to an enhancement in the QD brightness, especially if combined with a QW of higher quality and an efficient back-reflector (e.g., a Distributed Bragg Reflector, DBR). Regarding the possibility to obtain site-controlled QDs, there are some possible alternatives: from mounting a microsphere at the end of an optical fiber (which, in turn, could be mounted on a nanopositioner as in the removal process), to forcing the microsphere positioning by engineering the material's surface prior to deposition[189] or by arbitrary moving them employing a nano-manipulator. To this end, there are some undergoing studies which have given some preliminary but promising results. In Fig. 4.12 we show an example of the efforts so far, where four microspheres are placed on top of four different membranes. However, it is clear that not all the spheres are well centered, therefore further efforts are needed. As a final remark, it is worth noting that this technique could be employed for the realization of complex structures such as QDs arrays, by packing up the microspheres in a honeycomb structure[190], or QDs molecules by illuminating a microsphere with two tilted light beams.

4.3.1 Future developments

In order to further optimize the fabrication process, we present the results of extensive numerical calculations studying the properties of the PJs, which are the cornerstone of our fabrication technique. In particular, the intensity and the FHWM of the PJs were studied as a function of the laser wavelength and the microsphere radius to identify optimal parameter combinations.

The simulations are done with SMUTHI (see Chapter 3.3.2) and they consist of a plane wave incident on a SiO_2 microsphere placed on top of a multilayer structure comprising, from bottom to top: a GaAs substrate, a 2 nm layer of Ga_2O_3, 1500 nm of air, another 2 nm layer of Ga_2O_3, a 162 nm layer of GaAs and an additional 2 nm layer of Ga_2O_3(see Fig. 4.13). The values of the refractive index of GaAs, Ga_2O_3, and SiO_2 are taken from Papatryfonos et al. [191], Malitson [192], and Rebien et al. [193], respectively. It is worth mentioning that SMUTHI accepts only layers that extend indefinitely in the plane, hence it was not possible to simulate the suspended membrane but only a floating GaAs layer (sandwiched within two thin layer of oxide) on which was placed the microsphere, as shown in Fig. 4.13. The use of a single layer of GaAs instead of a $GaAs_{1-x}N_x$:H/GaAs QW is due to the fact that a fully hydrogenated GaAsN layer has the same optical properties of a GaAs layer (within 1% [52]), while the Ga_2O_3 layers were included to account for the native GaAs oxidation process [194].

The parameters we are interested in are the FWHM and intensity of the PJs, which were studied as a function of the incident wavelength and of the microsphere radius. In particular, we scanned wavelengths between 400 nm and 1550 nm in 5 nm steps and radii between 250 nm and 1025 nm in 25 nm steps. The results of the simulations are shown in Fig. 4.14. The FWHM and intensity values were obtained from the electric field intensity profile evaluated both in the direction parallel to the polarization of the incoming plane wave and in the orthogonal one, 33 nm below the surface. This particular depth is chosen accordingly to where the $GaAs_{1-x}N_x$:H/GaAs QW was placed in the sample used for the QDs fabrication. The results for the FWHM are shown in Figs. 4.14a and 4.14b and are calculated with respect to the baseline intensity relative to the unperturbed plane wave illumination calculated at the same depth. On the other hand, Fig. 4.14c reports the values of the electric field intensity measured at the center of the layer, on-axis with the microsphere. The grey points in the

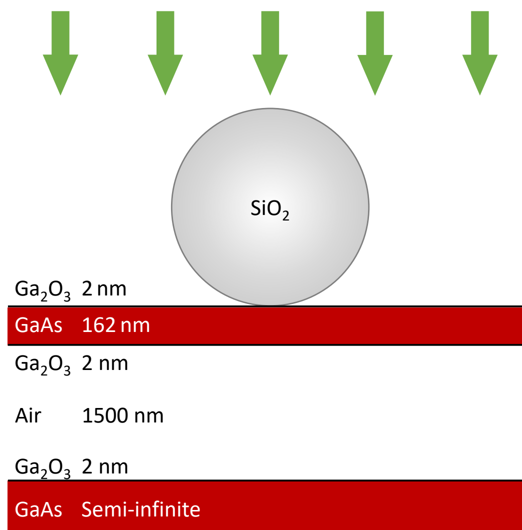

Figure 4.13. Scheme of the simulated sample, consisting of a suspended GaAs layer, an air-gap, a GaAs substrate and a SiO_2 microsphere. A thin Ga_2O_3 layer is also applied to all GaAs-air interfaces. The green arrows represent the plane wave hitting the microsphere and leading to the formation of the PJ. The drawing is not to scale.

maps represent those radius-wavelength combinations which are not associated with the formation of a PJ (i.e., the observed intensity maximum is off-axis), which would lead to the formation of the QD in a different position, or no QD formation altogether. Conversely, for all other radius-wavelength combinations, a PJ is properly formed within the GaAs layer, as we can see from Fig. 4.14e.

Observing the FWHM and intensity maps, the presence of an oscillating pattern immediately stands out. These oscillations can be better analyzed by plotting the quantities as a function of one of the two parameters, e.g. the wavelength, fixing the radius. As we can see from Fig. 4.14d, these oscillations are well pronounced between 400 nm and 800 nm, while at longer wavelengths they are less evident. Furthermore, it is clear, e.g. looking at the dashed lines, that the oscillations of the FWHM and the intensity are exactly out of phase (maxima of the former correspond to minima of the latter, and vice versa). The origin of this behavior is likely due to the interference between the incoming wave and the ones reflected within the microsphere and by the substrate. Due to the complexity of our system, this phenomenon is not easily attributable to a single origin. However, these oscillations can be exploited when selecting the proper microsphere radius and laser wavelength to tune the size of laser-written QDs, taking into account the actual sample geometry, within a broad range of values. Indeed, thanks to the presence of sharp oscillations in this composite system, it is possible to strongly change the PJs behaviour by slightly changing the laser wavelength, leading to an optimal control over the QDs dimension. Moreover, this effect can be combined with the control over the laser power to further increase the range of tunability. The wavelengths range in which the strongest oscillations appear (400-800 nm) overlaps nicely with the operating window of commercial Ti:Sa lasers (possibly equipped with a frequency-doubling crystal, in order to reach the lower end of the range). Furthermore, this is the ideal wavelength range for our laser-writing applications, since it includes perfectly the wavelengths window for breaking the N-H bonds (see Chapter 2.1).

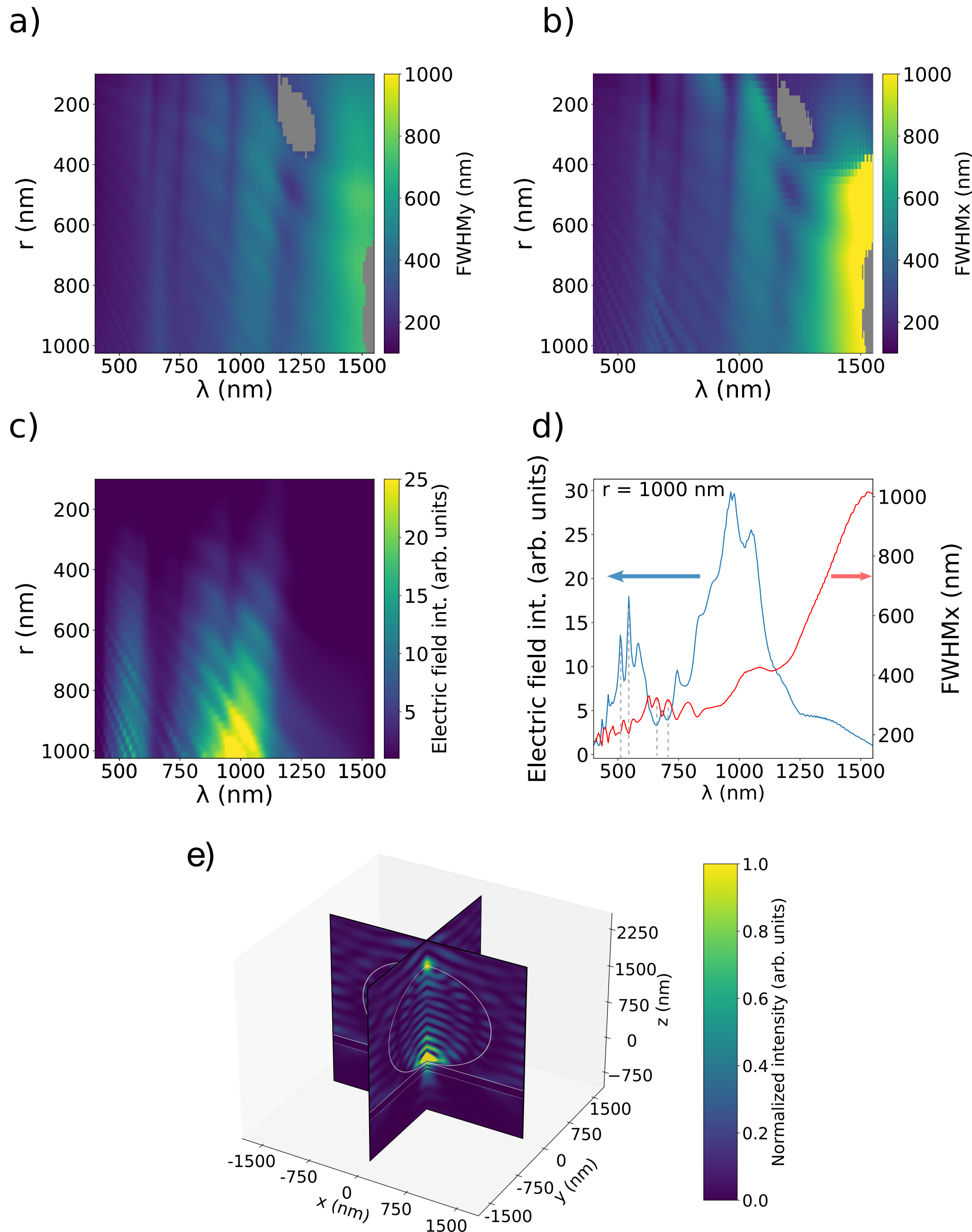

Figure 4.14. a) and b) 2D maps of the FWHM of the PJ along the y and x directions, respectively, as a function of the microsphere radius and of the wavelength. The incident wave is polarized along y. c) 2D map of the electric field intensity of the PJ as a function of the microsphere radius and of the wavelength. The grey points represent those radius-wavelength combinations that are associated with an intensity minimum rather than a maximum below the microsphere. d) plot of the FWHM (red curve) and the electric field intensity (blue curve) as a function of the wavelength for a microsphere of radius 1000 nm. The dashed lines are a guide to the eye to highlight the anti-phase behaviour. e) Map of the electric field intensity in the xz and yz planes, for a microsphere of radius 1 μm illuminated by a plane wave with $\lambda = 545$ nm. The white lines represent the contour of the microsphere and of the QW.

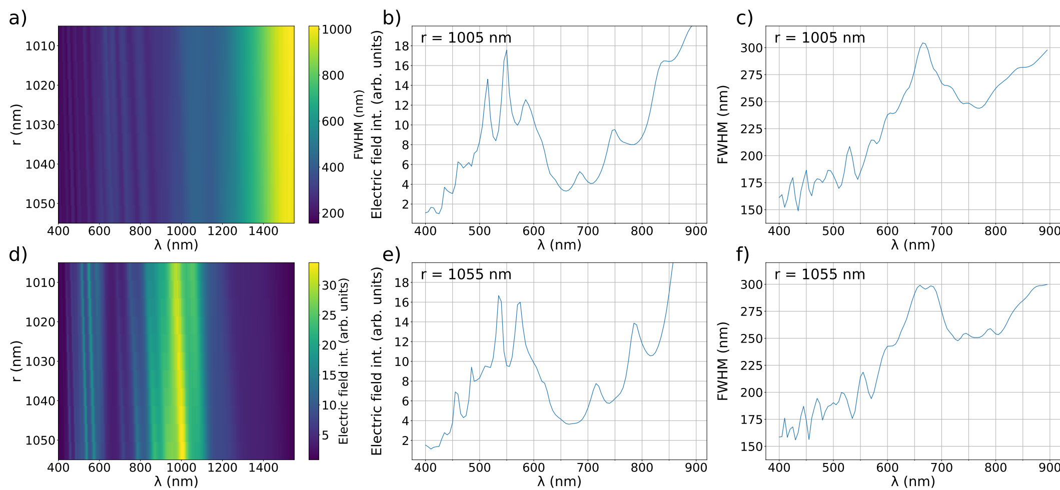

Figure 4.15. a) and d) 2D maps of the FWHM and the electric field intensity of the PJ, respectively, as a function of the microsphere radius and of the wavelength. b) and e) Plots of the electric field intensity as a function of the wavelength, in the range between 400 nm and 900 nm, for a microsphere of radius 1005 nm and 1055 nm, respectively. c) and d) Plots of the FWHM in the same configuration of b) and e). The reported wavelength range in these last four plots is selected to more clearly highlight the radius effect on the position of the peaks.

In order to apply the simulated results in practice, we must take into account that the microspheres are not perfectly identical; indeed, the standard deviation of their radii is about 25 nm. This inevitably leads to an uncertainty in determining the correct behaviour of the oscillations, which in turn is detrimental to the optimal control of the QDs' size. To this end, the results of a more detailed study of the effect of particle polydispersity are reported in Fig. 4.15, where the FWHM and intensity of the PJs are studied as a function of the wavelength, between 400 nm and 1550 nm with 5 nm step, and of the microsphere radius, focusing on a narrower interval (between 1005 nm and 1055 nm) sampled with higher precision (5 nm steps). From Figs.4.15a) and d), it is clear that a change in the radius causes a spectral shift of the observed oscillations. This effect is negligible if the change in the radius is below 10 nm but starts to be relevant above this value. Indeed, if we have a look at the the electric field intensity and FWHM plots for radii of 1005 nm and 1055 nm, we can see that a peak for one radius corresponds to a minimum for the other, and vice-versa (see Figs. 4.15b, 4.15c, 4.15e, 4.15f). Therefore, it is of utmost importance to determine the size of the microspheres used with an accuracy smaller than 10 nm to have a fine control over the PJ properties and thus on the QDs. To do so, the microspheres size could be measure with a SEM (Scanning Electron Microscope) or an AFM (Atomic Force Microscope). The measured value could be then used in the simulation, leading to the straightforward identification of the laser wavelength required to obtain the desired PJs' width and intensity. Furthermore, these detailed simulations clarify that the predominant cause at the origin of the big inhomogeneous broadening of the QDs emission is likely the differences in the microspheres radii employed for their fabrication.

Finally, one of the possible application of our fabrication technique is the ability to fabricate multiple QDs at once with a single laser pulse. To investigate this, we have studied the PJ properties generated by the simultaneous illumination of two adjacent microspheres. Considering two microspheres aligned along the x direction and a plane wave polarized

along the same direction the FWHM and peak intensity of the PJs are increased by 11% and decreased by 18%, respectively. While, considering a plane wave polarized along the y direction, the FWHM and peak intensity of the PJs are increased by 9% and decreased by 13%, In both cases, however, the position of the PJ remains within 10 nm from the intended fabrication position. Therefore, when using more than one microsphere, it will be important to evaluate case by case the effects over the PJs properties, in order to achieve optimal control on the fabricated QDs.

In conclusion, this systematic study of the properties of PJs as a function of particle radius and wavelength demonstrate the flexibility of PJs in the laser-writing process. Moreover, it leads to a deeper knowledge of the fabrication process and it paves the way to drastically increase the level of control over the QDs properties. Lastly, it is worth noting that this approach can be applied also to other kinds of emitters, and not only to QDs.

Chapter 5

Engineer G-centers emission with strain

In this chapter it will be presented an approach to locally tune the G-center emission employing strained suspended silicon membranes. The samples realized are optically characterized and the main results of such characterization are presented.

5.1 The samples structure

In this work we have fabricated three different samples named "1.3", "1.4", and "7.3". The structure of these samples is described in detail in Chapter 3.1.9, along with the description of the fabrication processes employed for their realization. To briefly summarize, they consist in SOI samples implanted with carbon atoms and made by: a 125 nm silicon layer, a 2 µm thick SiO_2 layer and a silicon substrate (see Fig. 5.1). Sample 1.3 and 1.4 contain carbon atoms at a nominal depth of about 24 nm while sample 7.3 at a nominal depth of 99 nm. The samples are patterned by optical lithography to realize 12 different fields, divided in 4 columns (labeled with letters) and 3 rows (labeled with numbers), each one containing 25 patterned squares.

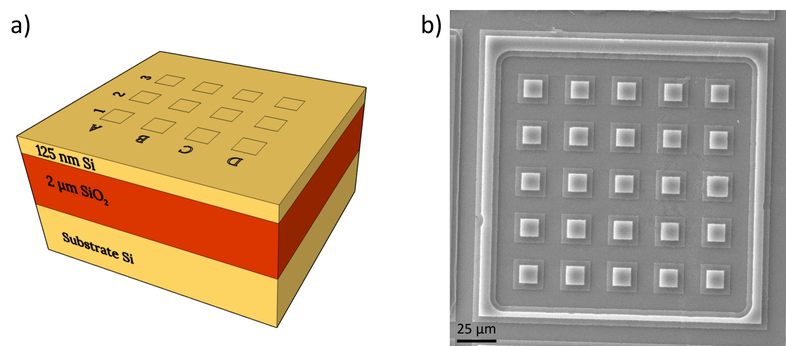

Figure 5.1. a) Sketch of the sample employed to realized the silicon suspended membranes. The 12 squares on top of the sample represent the 12 fields. b) SEM image of one of the fields after the realization of the suspended membranes. The whiter coloured parts are the silicon dioxide areas that support the suspended membranes, which are the transparent squares around the supports.

By chemically etching the SiO_2 layer, square silicon suspended membranes are realized. The size of these membranes increases going from row A to D, nominally they have a lateral size of 10, 12, 15, and 20 μm. Then, a SiN_x layer is deposited on top of the samples to introduce a static stress within the membranes. The different growth parameters leads to the introduction of strain of different nature within the three samples (see Table 3.1 and Chapter 3.1.9 for more details): sample 1.3 is stressed in a compressive way, sample 1.4 is stressed in a tensile way, sample 7.3 is slightly stressed in a tensile way or almost unstressed. In Fig. 4.1 the sample structure is shown, along with a SEM image of one of the field within the sample where we can clearly see the suspended membranes.

5.2 Samples characterization

Once the samples were fabricated, we optically characterized them by means of low temperature (10 K) micro PL. The first measurements were performed on the unpatterned areas of samples 1.3 and 1.4, i.e. far from the 12 fields. These samples are characterized by a shallower G-centers implant depth, hence the effects connected to the presence of the SiN_x layer would be easily detected. For the sake of simplicity, later on we will refer to the measurements performed in these areas as “Flat”.

In Fig. 5.2a are reported the PL spectra measured in the two samples and, for comparison, one from a sample without SiN_x. As we can see, the spectra profiles are almost identical and they are characterized by a sharp ZPL and a well defined phonon sideband. From the fit of the ZPL with a Lorentzian function we have found a FWHM of (868 ± 28) μeV for the sample without SiN_x, (848 ± 21) μeV for sample 1.3, and (773 ± 35) μeV for sample 1.4. Therefore, the presence of the SiN_x causes a slight narrowing of the ZPL peak. This is likely due to the defects passivation effect of silicon nitride, which is a well known and studied effect that makes this material widely used in solar cells fabrication[195]. Superimposing the PL spectra, a small shift in the ZPL energy position is observed (see inset Fig. 5.2b). Where the ZPL from sample 1.3 is red-shifted of about 200 μeV while the one from sample 1.4 is blue-shifted by the same amount. It is worth mentioning that these energy differences are

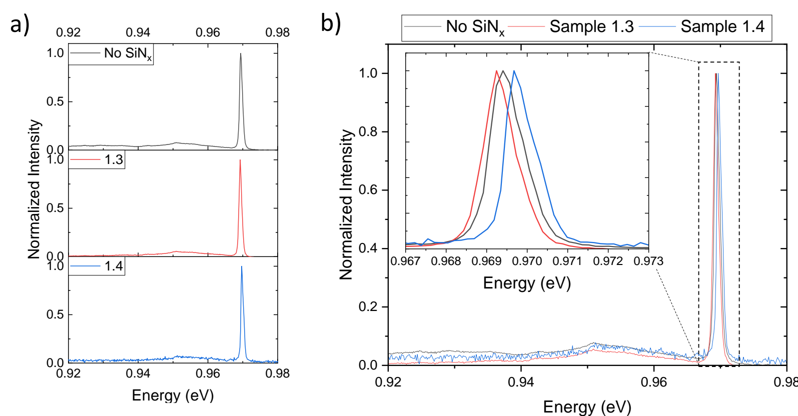

Figure 5.2. a) Low temperature micro-PL spectra of the G-centers collected in a SOI sample without SiN_x on top (black curve), in sample 1.3 (red curve) and in sample 1.4 (blue curve). The spectra are obtained with a CW excitation (λ = 532 mW, P_{exc} = 2 mW) b) Superposition of the three spectra colored as before. Inset: zoom around the ZPL peak energy.

perfectly within our spectral resolution, however their presence could indicate the presence of a small amount of strain in the topmost silicon layer due to SiN_x.

To test our hypothesis, we have performed room temperature micro-Raman measurements on two upatterned samples that have the same structure as sample 1.3 and 1.4. The measured spectra are reported in Fig. 5.3 along with the Raman spectrum of a bulk crystalline silicon sample, as a reference. The peak showed in Fig. 5.3 refers to the silicon Raman peak, which is centered at $(520.700 \pm 0.005)\,\mathrm{cm}^{-1}$ in the reference sample, perfectly coherent with the literature[196]. On the other hand, the signal coming from the samples containing SiN_x is slightly shifted. Fitting them with a Lorentzian function (see Fig. 5.3b) we found out that the peak from the sample similar to 1.3 is centered at $(520.873 \pm 0.013)\,\mathrm{cm}^{-1}$ while the other one is centered at $(520.541 \pm 0.004)\,\mathrm{cm}^{-1}$. These shifts are well within the system resolution, therefore we can safely assume that no stress is present within the flat areas of sample 1.3 and 1.4.

This is further confirmed by two other evidences. The first one is the fact that in the presence of a compressive strain the silicon band gap increase and thus, the G-centers ZPL should shift at higher energies. However, accordingly to the Raman measurements, the sample with the same structure as 1.3 shows a small compressive strain and yet the corresponding G-centers PL emission is red-shifted respect to the unstrained sample. It goes without saying that the same consideration with reversed parameters, i.e. tensile strain and blue-shift of the PL, is valid when considering the other sample. The second evidence relies on evaluating the stress within the two samples from the two Raman shifts measured. Assuming a uniaxial stress, σ, it can be written as: $\sigma\,(\mathrm{MPa}) = -434 \cdot \Delta\omega\,(\mathrm{cm}^{-1})$[197, 198], where $\Delta\omega$ is the shift of the Raman peak expressed in cm^{-1}. Therefore, evaluating the stress within the two samples, we find a stress of about -75 MPa for the former sample and about 69 MPa for the latter. According to the literature[199, 200], such values of stress would result in a splitting of the ZPL of the G-centers of about 1.79 meV and 1.95 meV, respectively, which was not observed.

From both micro-PL and Raman measurements we can conclude that the deposition of

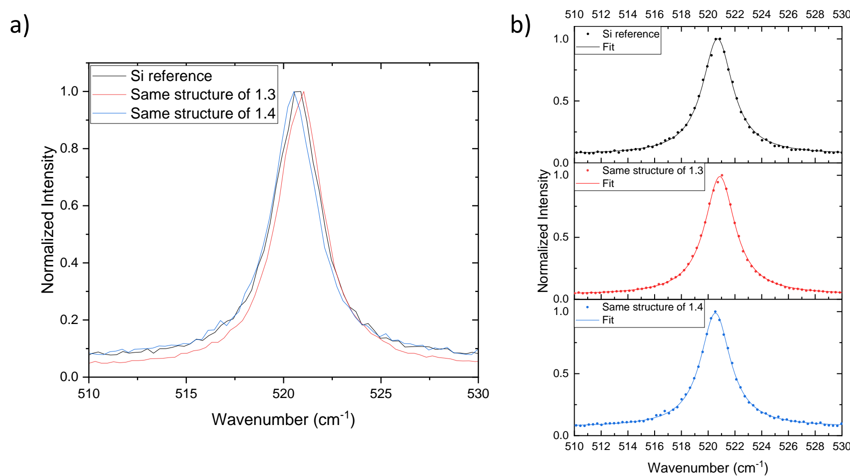

Figure 5.3. a) Micro-Raman spectra of the samples with the same structure as sample 1.3 and 1.4 (red and blue curve, respectively), superimposed to the spectrum of a bulk crystalline silicon sample as a reference (black curve). b) The same spectra showed in a) (dots) with the corresponding Lorentzian fit (continuous curves).

a strained SiN_x layer does not introduce strain within the unpatterned areas of the sample under study. This is likely due to fact that the silicon layer can relax towards the substrate. Moreover, the presence of the aforementioned layer does not worsen the optical properties of the G-centers.

5.2.1 Microphotoluminescence maps

In order to characterize the suspended membranes, we have performed low temperature micro-PL maps in all the three samples. Each map consists in a 2D raster scan of the sample with steps of 500 nm where, in each position, a PL spectrum is collected. The spectra are then integrated and an intensity map is obtained, see for example Fig. 5.4a. We can see that the presence of the suspended membranes immediately stands out. This is easily explained since otuside the membranes the silicon layer containing the G-center was etched away, hence no PL signal is expected from those regions.

It is worth noting that, just 15 μm outside the area patterned with the membranes, the PL spectrum is the same as in the flat area, i.e. formed by a single sharp ZPL line with the associated phonon sideband (see Fig. 5.4b), thus meaning that the fabrication process affects the emission only locally, i.e. within the membranes. Indeed, at the center of the suspended membrane, the ZPL peak splits in two sharp peaks as we can see from Fig. 5.4c. A similar peak splitting was observed by two independent groups when measuring the G-center PL in samples subjected to mechanical stress[199, 200]. In particular, they observed a splitting in two peaks when the stress was applied along the [001] crystalline direction. Moreover, the energy difference between the peaks is directly proportional to the amount of stress applied. They also found out that applying stress along the [111] and [110] directions results in a three and four peak splitting, respectively. This would mean that at the center of the membranes the dominant strain component is the one directed along the [001] direction, which, in our system, is the vertical direction (or z direction).

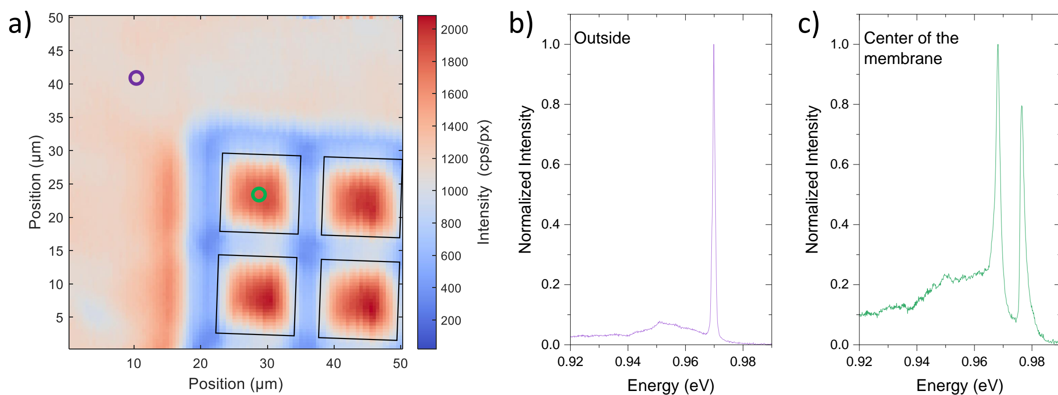

Figure 5.4. a) Low temperature micro-PL map of a portion of a field containing membranes with 12 μm lateral size ($\lambda_{exc} = 532$ nm, $P_{exc} = 2$ mW). The colorscale is given by the intensity of the PL signal in each position. It is obtained integrating the spectra between 0.92 and 0.99 eV, i.e. the whole energy range measured. The black squares are a guide to the eye to locate the membranes positions. The purple and green circles show the positions where the spectra in panel b) and c) are measured. b) and c) PL spectra measured far from the patterned area and at the center of a suspended membrane, respectively. A clear splitting of the G-center ZPL is observed in the membrane.

5.2.2 FEM simulations

To confirm the presence of strain within the silicon layer, we have performed FEM simulations of a suspended membrane. The simulated membrane mimics the actual structure and it consists in a square membrane formed by a silicon nitride layer on top of silicon. The membrane is supported by a silicon dioxide pillar with a square base and the whole structure is placed on a silicon substrate. A sketch of the membrane is reported in Fig.5.5.

The sizes of the simulated membrane and pillar are 5 µm and 3 µm, respectively. These values are obtained scaling by a factor 0.25 the real values measured from a SEM image of the membrane. Indeed, the equations regulating strain are self-similar and hence scaling the dimensions would give the same results. This is true as long as we are interested in the ratios between different strain components or if the components are referred to an initial strain value, ϵ_0, as in this case (i.e. the strain within the SiN_x layer). In any case, the strain components along x, y, and z were calculated in the whole 3D structure. However, we now report only the results within the silicon layer since they are the interesting ones. It is worth mentioning that the results that we will discuss are obtained simulating a silicon nitride layer under compressive strain.

In Figs. 5.6a to f, are reported the maps of the strain components in the $x - y$ plane calculated at the nominal implant depth of the G-centers in the three samples, i.e. 24 nm and 99 nm. Focusing on the center of the membrane, we can clearly see that in both scenarios the ϵ_{xx} and ϵ_{yy} components have the same values. Therefore, the G-centers perceive a homogeneous and omnidirectional in-plane strain that does not lead to a symmetry breaking into the plane and thus a splitting of the peaks is not expected. On the other hand, the presence of a non zero out-of-plane strain component leads to a break the symmetry along the z direction, thus leading to the two peaks splitting that we observed.

In addition, we have evaluated the behaviour of the out-of-plane strain component, in the center of the membrane, as a function of the depth within the silicon layer. As we can see from Fig. 5.6g, the ϵ_{zz} is practically constant within all the silicon layer, therefore we expect a two peak splitting independently from the implant depth. It is worth mentioning that different initial strain conditions within the SiN_x, i.e. tensile or compressive, would lead to the same two peaks splitting[201]. The only factor that matters is the absolute amount of strain introduced in the layer, which regulates the splitting between the two peaks.

Furthermore, we can see that the two in-plane components differ going from the center of the membrane to its border. Indeed, they maximally differs at the center of the four

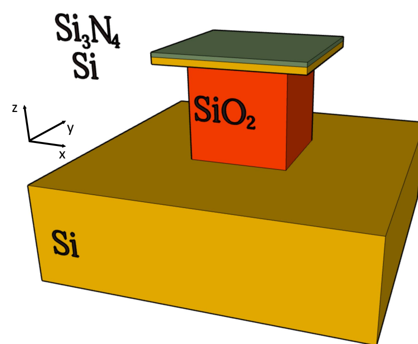

Figure 5.5. Sketch of the simulated membrane.

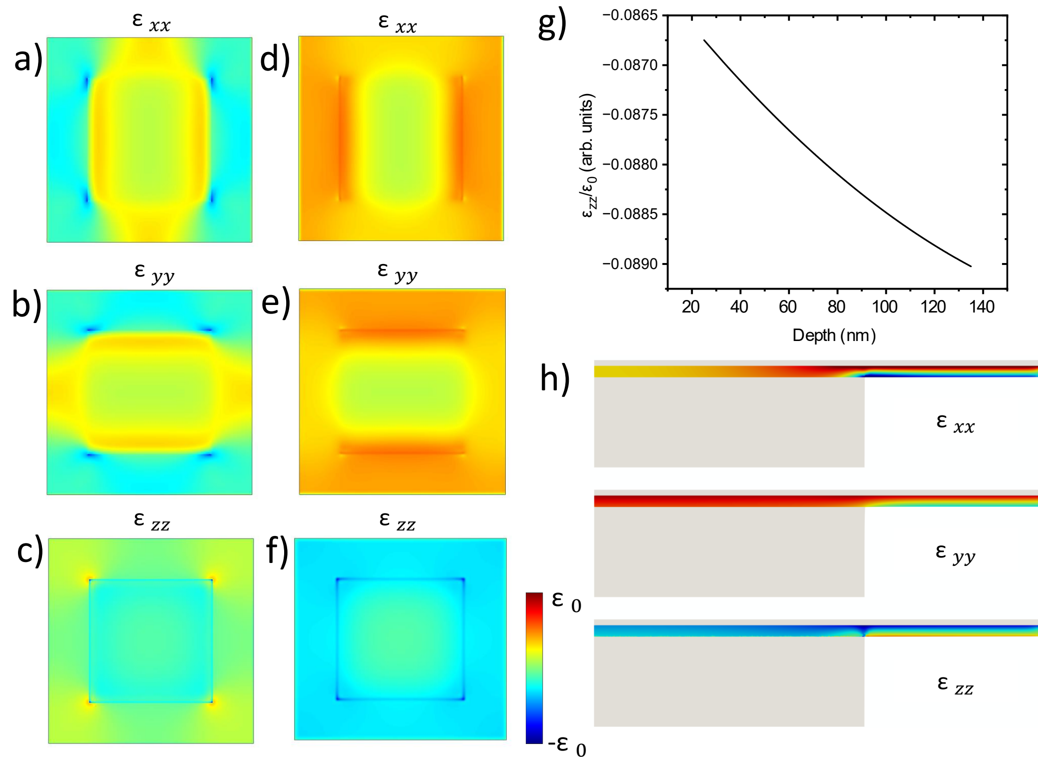

Figure 5.6. a) - f) 2D maps of the simulated strain components in the $x-y$ plane. In particular, a), b) and c) refer to the components evaluated 24 nm below the SiN_x/Si interface. Whereas, d), e) and f) refer to the components evaluated 99 nm below the interface. At both depth in the center of the membranes the ϵ_{xx} and ϵ_{yy} components have the same values. g) Plot of the ϵ_{zz} component, rescaled by the initial strain ϵ_0, as a function of the depth within the silicon layer. The relative change in the strain value is minimal, about 0.6%. h) 2D maps of the simulated strain components in the $x-z$ plane. The strain components in the supported areas are almost constant while within the suspended part they gradually change moving away from the interface. The resulting vertical displacement leads to a bending in the membranes downwards. The same colorbar is employed in all the maps.

suspended parts, while they are equal on the corners. Therefore, we expect to observe a second break of the symmetry along the sides of the membranes and thus the presence of more than two peaks. On the other hand, measuring the corners we expect to keep observing only two peaks.

It is worth mentioning that the value of the out-of-plane strain component at the center of the membrane strongly depends on ratio between the suspended membrane size and the supporting pillar size (simulations not shown). In particular, increasing it, it would result in an overall reduction of the strain value and vice versa. The membranes in our samples are realized by dipping the samples in a acidic solution for a fixed amount of time to perform chemical etching. Therefore, we can safely assume that the size of the suspended part is always the same, independently to the membrane size, and thus the membrane to pillar ratio is directly proportional to the membrane size. As a consequence, the resulting strain would follow the opposite trend and thus, we expect a reduction in the G-centers peak splitting when increasing the membranes size.

As a final remark we can see that the FEM simulations correctly predict the observed bending of the membranes, connected to the presence of strain. In Fig. 5.6h is reported the maps of the three strain components evaluated in the $x-z$ plane obtained cutting the membrane along the plane passing from its center. We can see that in proximity to the silicon nitride layer there is an in-plane tensile strain, i.e. $\epsilon > 0$, and an out-of-plane compressive strain, $\epsilon < 0$. Focusing on the ϵ_{zz} component, we can see that, moving away from the SiN_x/Si interface, it decreases until it changes sign, i.e. it becomes tensile. This causes a vertical displacement which in turn leads to a bending of the suspended part downwards. This results is perfectly coherent with what we expected and with what we observed by the SEM measurements performed on the fabricated membranes (see Fig. 3.8c). It goes without saying that the considerations proposed so far would be reversed considering a silicon nitride layer with tensile strain.

5.2.3 Analysis of the microphotoluminescence spectra

To confirm the results of the simulations, we have extracted a spectrum in the center of the membrane from each micro-PL map. These spectra are reported in Fig. 5.7. As correctly predicted, in all three samples we observe two distinguished peaks, along with the typical phonon sideband. Moreover, we can observe that that the energy splitting between the two peaks increases when reducing the membranes size. This is the experimental confirmation of the dependence of the strain on the ratio between the membrane size and the supporting pillar size. Furthermore, the peaks measured in sample 7.3 show a reduced linewidth with the respect to the others measured in sample 1.3 and 1.4. This is likely connected to the deeper G-centers implant depth and thus, a reduced effect of surface defects in broadening the emission.

Studying the energy position of the two peaks as a function of the membranes size, we have found that it depends linearly on the inverse of the membrane area, as it is clear from Fig. 5.8a. Moreover, we can see that the high energy peak (HE peak) is more sensitive to changes of the membrane area with respect to the low energy peak (LE peak).

The three samples show three different linear dependencies which can be in part explained considering the absolute value of the strain introduced by the SiN_x layer. Indeed, nominally, the SiN_x layer in sample 1.3 is the most strained one (in absolute terms) and thus is the one presenting the higher splittings, i.e. the steepest slopes. Moreover, the absolute

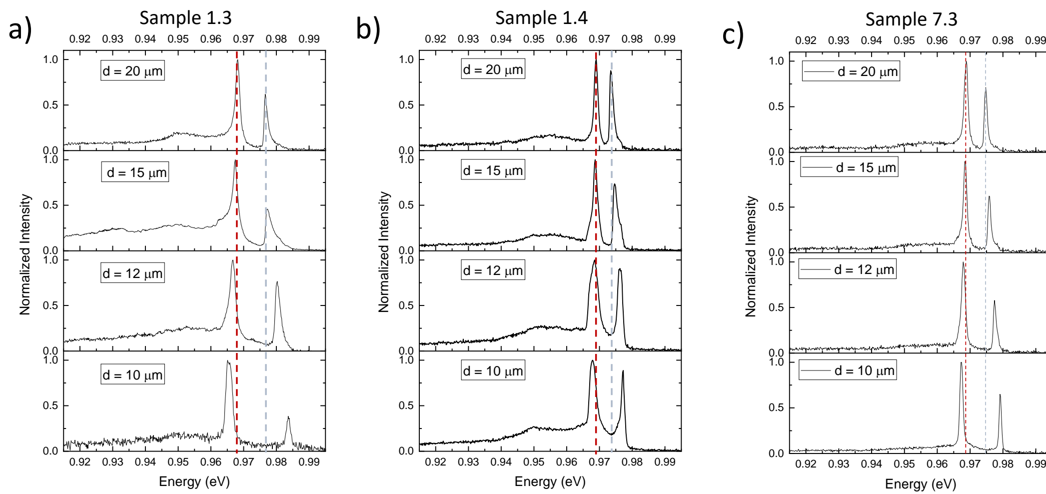

Figure 5.7. a), b) and c) Low temperature micro-PL spectra (λ_{exc} = 532 nm, P_{exc} = 2 mW) extracted from the micro-PL maps performed on four membranes of different size in sample 1.3, 1.4 and 7.3, respectively. The blue and red dashed lines are guides for the eye to underline the dependence between the peaks splitting and the membranes size.

value of the strain in this sample is, at least in theory, about two times the one in the SiN_x layer of sample 1.4 and this perfectly reflects in the measured data. Indeed, within all the membranes the splitting of sample 1.3 is about two times the one in sample 1.4 (e.g. in the smallest membrane $\Delta E_{1.4}$ = 9.4 meV and $\Delta E_{1.3}$ = 18.2 meV). However, sample 7.3 does not follow the same trend, indeed it should be the least strained and thus presenting the smallest splittings. The behaviour of this sample is not yet fully understood and it is currently under further studies. Despite this, we have shown that can tune the G-centers emission acting on two different parameters: the membrane size and the SiN_x deposition properties. Combining both effects we were able to tune the G-centers emission over a ≈ 20 meV energy range. Therefore, by simply realizing suspended strained membranes, we have developed a technique to tune a SPE emission in a 25 nm range without the need of any external fields.

Controlling the G-centers emission comes with the cost of broadening the emission peaks. Indeed, by fitting the HE and LE peaks with a Lorentzian function, we can see that their FWHM is higher than the one of the ZPL peak in the flat areas of sample 1.3 and 1.4 (see e.g. Figs. 5.8d and 5.8e). However, in light of exploiting the G-centers as SPEs for QIT, this is only a minor issue since it can be easily solved by spectrally filtering the emission or by selecting an application where a reduced broadening (i.e. a high indistinguishability) is not required such as QKD.

As said before in this work, one of the important properties of SPEs is their brightness. To evaluate it in our samples, we have integrated the PL spectra showed in Fig. 5.7 over the emission peak, i.e. the LE or HE peak, and we have multiplied the result by the efficiency of our setup at the G-centers emission wavelength (22%). From doing so, we have obtained an estimation of the photon counts on the first lens. The results are showed in Figs. 5.8b and c, where we have also reported the values measured in the flat areas of sample 1.3 and 1.4 for comparison. It must be taken into account that we are measuring ensembles of G-centers and not single defects, hence these values cannot be directly compared with the ones from other

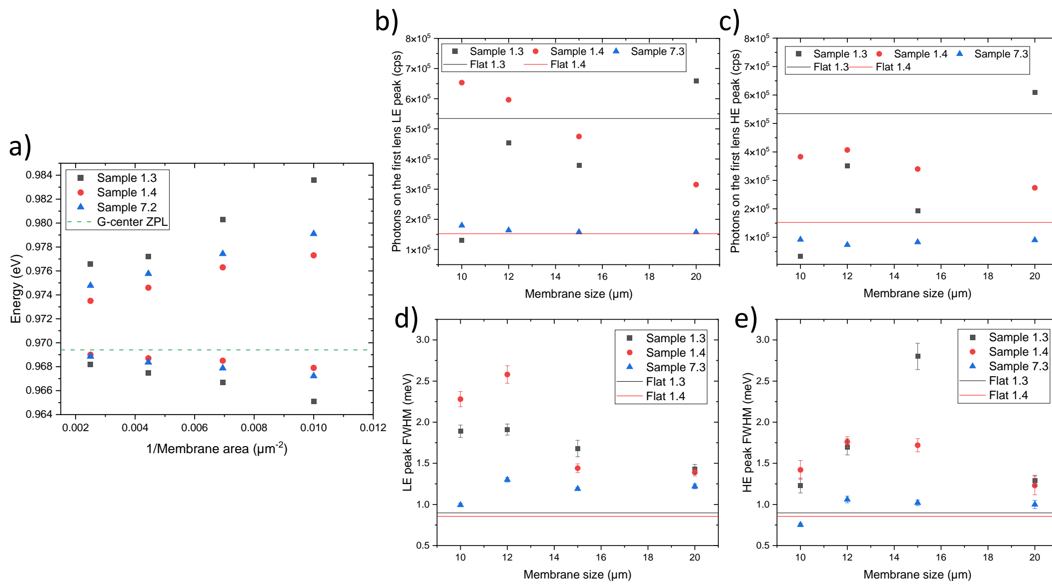

Figure 5.8. a) Plot of the energy position of the two observed peaks within the three different samples (scatter plots), along with the value of the G-centers ZPL energy position in a sample without SiN_x (dashed line), as a function of the inverse of the membrane area. The linear dependence between the two immediately stands out. b) and c) plot of the intensity of the LE an HE peak, respectively, in terms of photons impinging on the first lens as a function of the membrane size. The value is obtained integrating the emission peak and multiplying it by the nominal efficiency of the system (22%, see Chapter 3). d) and e) plot of the LE and HE peak FWHM, respectively, obtained fitting the peak with a Lorentzian function as a function of the membrane size.

SPEs. However, we are not interest in the absolute brightness values but on evaluating the intrinsic efficiency of our emitters and the effects connected to the membranes fabrication and to the SiN_x deposition.

Starting from the results measured in sample 7.3, we can see that the brightness is quite limited and it remains more or less constant within all the membranes. On the contrary, in the other two samples we observe a dependence on the membrane size. Indeed, in sample 1.3 we can see that the brightness of both peaks seems directly proportional to the membrane size, with only one exception (i.e. the 15 μm membrane). However, only within the biggest membrane a higher brightness, with respect to the flat area, is observed. On the other hand, the brightness of both LE and HE peak measured in sample 1.4 is always higher than the one measured in the flat area. Moreover, both peaks show an inversely proportional dependence on the membrane size. These are interesting results since they suggest that employing the strained suspended membranes to tune the G-centers emission will results in drastically changing the brightness of the emitters. In particular, within the membrane of the same nominal size, in sample 1.4 we observe an enhancement of the brightness of a factor 4 with respect to the flat area, while in sample 1.3 we observe a reduction of a factor 3.8. Therefore, we need to carefully select the optimal conditions, in terms of membrane size and SiN_x deposition parameters, to achieve both the desired energy emission and the optimal brightness to employ the G-centers in the desired application.

In addition to the spectra at the center of the membranes, from the micro-PL maps we have extracted the spectra measured at the corners and in the sides. Indeed, we wanted to

verify what we expected from the FEM simulations, i.e. the presence of only two peaks in the corner and of more than two in the sides. In Fig. 5.9 is reported a micro-PL map from which we have extracted the aforementioned spectra. As we can see, we observe the expected results. Moreover, the presence of four different spectra is coherent with both FEM simulations and literature.

From the simulated strain maps showed in Figs. 5.6a-f we can see that, along the sides of the membranes, one of the two in-plane components, i.e. ϵ_{xx} and ϵ_{yy}, is always predominant. Therefore, considering that the out-of-plane component is always present, in these regions the strain is mainly directed along the [011] or [101] crystalline direction (in our sample the out-of-plane direction corresponds to the [001] crystalline direction). Recalling the results observed in the literature, they observed the presence of a four peaks splitting in the presence

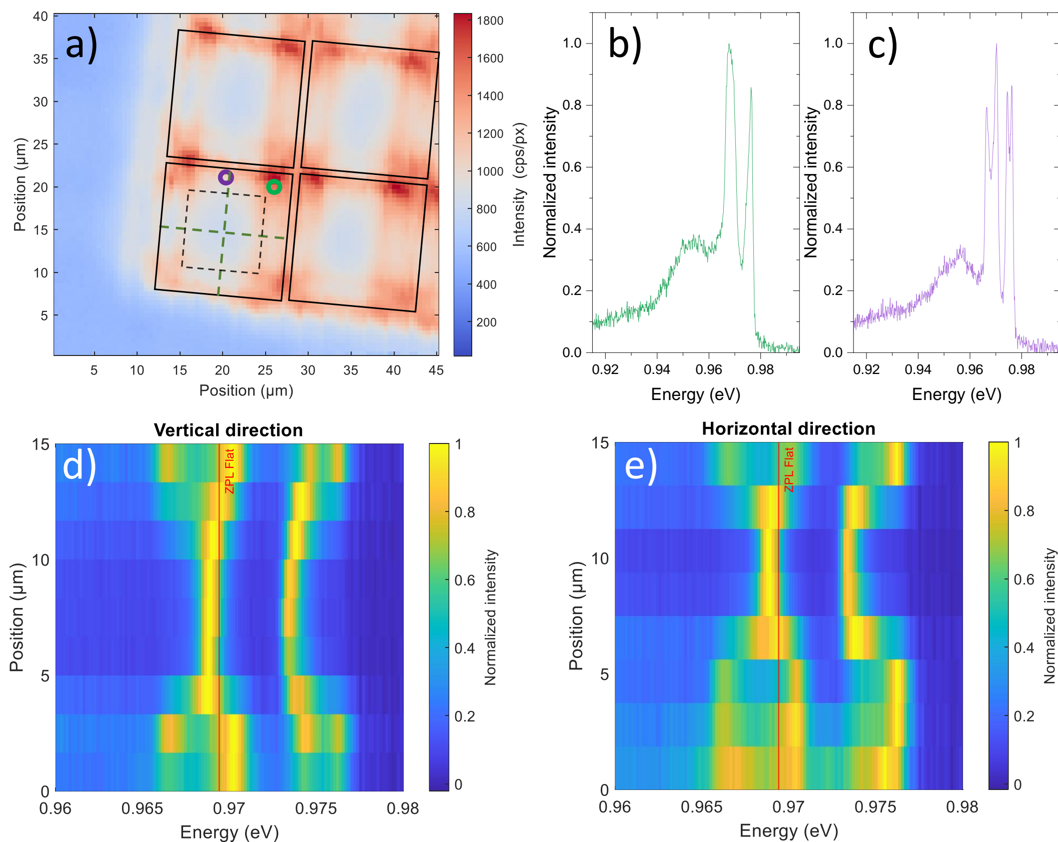

Figure 5.9. a) Micro-PL map of some a portion of a field containing 15 µm membranes (λ_{exc} = 532 nm, P_{exc} = 2 mW). From the map we can clearly distinguish the presence of the membranes and their suspended part. As a guide for the eye, we have draw black continuous squares to identify the membranes and a black dashed square for the pillar supporting the membrane. The green dashed lines represent the directions along which the plot showed in panels d) and e) are extracted. The purple and green circles indicate the position of the spectra showed in b) and c), colored accordingly. b) and c) normalized PL spectra extracted from the map, showing the presence of two peaks in the corner of the membrane and of four distinguished peaks in the side. d) and e) normalized PL spectra extracted along the vertical and horizontal direction, respectively. The red line represent the energy of the ZPL measured in the flat area of the sample. The behaviour of the spectra along the two directions is in good agreement with the simulations.

of an uniaxial strain along [110] direction, which, for symmetry reasons, is equivalent to the [011] and [101] directions. Therefore, combining the results from the simulations and the literature, on the sides of the membranes a four peaks splitting was expected and indeed observed. To clearly show the transition between two and four peaks we have extracted the PL spectra along the vertical and horizontal directions passing through the center of the membrane. The spectra are represented in Figs. 5.9d and e. We can clearly see that moving away from the membranes center the presence of more than two peaks emerges.

5.2.4 Time-resolved photoluminescence measurements

A parameter to evaluate the achievable maximum brightness of our emitters is the radiative decay time. To measure it, time-resolved PL (TRPL) measurements were performed in all the three samples both in the flat areas and within the membranes. It goes without saying that within the membranes we have measured the time decay constant of both the HE and LE peaks. In order to not weight down this work, we present only the results concerning sample 1.4, since they show some interesting properties.

In Fig. 5.10a are reported the TRPL measurements in the flat area of sample 1.4 and within the membranes, along with a TRPL measurement in a sample without SiN_x as reference. We can clearly see that the two curves are in a very good agreement. This further confirms that the presence of SiN_x does not affect the G-centers emission and, moreover, does not introduce any additional non-radiative channel. To evaluate the time decay constant

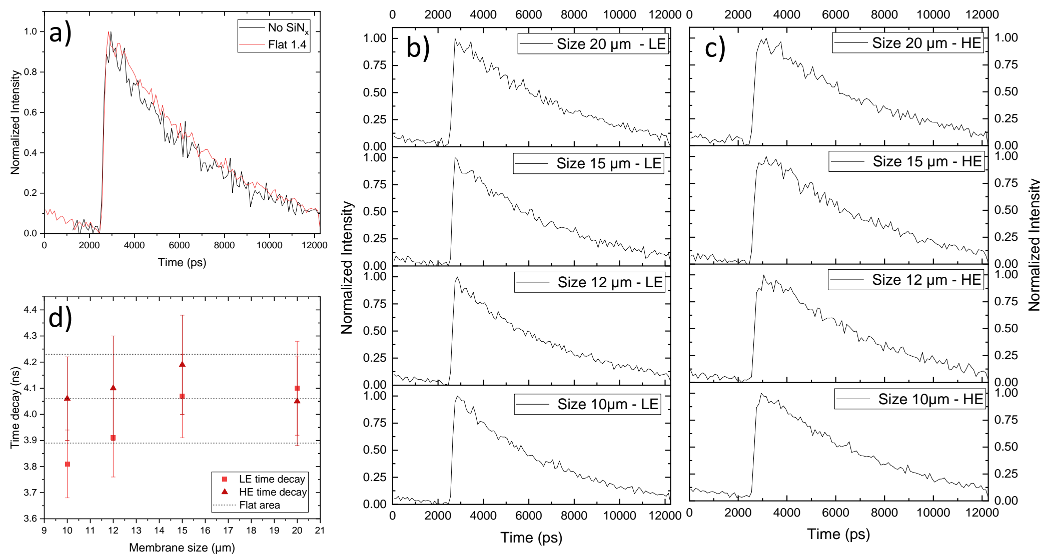

Figure 5.10. a) TRPL measurement in the flat area of sample 1.4 (red curve) compared with the same measurement performed in a sample without SiN_x (black curve). There is a clear agreement between the two decay curves, whose fits give the time decay constants of (4.06 ± 0.17) ns for the flat area, and (4.13 ± 0.25) nm for the sample without SiN_x. These values are perfectly in agreement with the literature. b) and c) TRPL measurements of the LE and HE peak, respectively, performed within the membranes. d) Time decay constants for the LE and HE peak within sample 1.4 as a function of the membrane size. In the plot is reported also the value in the flat area with the corresponding error (dashed lines) for comparison.

we have fitted the curves with an exponential convoluted with a Gaussian. The Gaussian curve models the impulse response function of our system (FWHM = 200 ps). By fitting the two TRPL measurements with this function we find: $\tau_{Flat} = (4.06 \pm 0.17)$ ns and $\tau_{NoSiN_x} = (4.13 \pm 0.25)$ ns. Therefore the two measurements are perfectly consistent within the error. It goes without saying that even the measurements performed in the flat areas of sample 1.3 and 7.3 are coherent with these values.

In Figs. 5.10b and c are shown the TRPL measurements of LE and HE peak, respectively, within membranes of different sizes. At a first glance the decays seems independence to the membrane size however, fitting the curves, we find out that the radiative decay constant of both peaks rises, increasing the membrane size up to 15 µm, and then it goes back down (see Fig. 5.10d). This behaviour could be connected to the symmetry breaking due to the presence of strain that allows transitions with shorter lifetimes that were previously forbidden. However, it is worth noting that all the time decay constants are almost consistent within the error, therefore it could be simply due a slightly different concentration of non-radiative defects around the emitters and thus not being connected to the presence of strain. In Fig. 5.10d is also reported, as a dashed line, the measurement of the time decay within the flat area. As we can see, all the measured decays are consistent with the one measured in this area, meaning that the membranes fabrication process does not introduce further non radiative defects in the sample. This is confirmed by the observed increase in the emitters brightness showed above. An interesting aspect that emerges from these measurements is the consistency between the HE and LE time decays, especially in the biggest membranes. This implies that the physical origin of these two emissions is the same. Indeed, as said before, the presence of the two PL peaks is related to the removal of the G-centers energy degeneracy due to the introduction of strain within the system. Therefore, a similar time decay constant was expected.

The measurements performed on sample 1.3 and 7.3 gives time decay constants in a temporal range between 3.6 and 4.6 ns, perfectly consistent with the literature and sample 1.4. The measured radiative time decays show that the G-centers within the suspended membranes could easily reach a brightness of hundreds of MHz. Despite the TRPL measurements were performed on ensemble of G-centers, it is worth noting that the such values represent the achievable brightness also for single G-centers. Indeed, it was proved that single and ensemble of G-centers are characterized by similar decay times[136]. In light of employing G-centers as SPE in QIT, this value would be an optimal starting point, which could be optimized combining the use of strain to tune the emission with a Purcell effect to reduce the radiative decay time and thus, enhance the emitter brightness.

5.2.5 Polarization measurements

The previous studies on the G-centers in stressed samples reported that the peaks that emerge from the splitting of the ZPL were polarized[199, 200]. In particular, when applying the stress along the [001] crystalline direction, the HE peak appears to be strongly polarized perpendicularly to the strain direction while the LE peak is only partially polarized (up to 30%) along the direction parallel to the strain component. Moreover, they observed that the degree of polarization was independent from the amount of stress applied.

To confirm this, we have performed polarization measurements within the membranes of sample 1.4, to test both the polarization of the peaks and its independence from the amount of strain applied. To do so, we have decided to perform the measurements in the

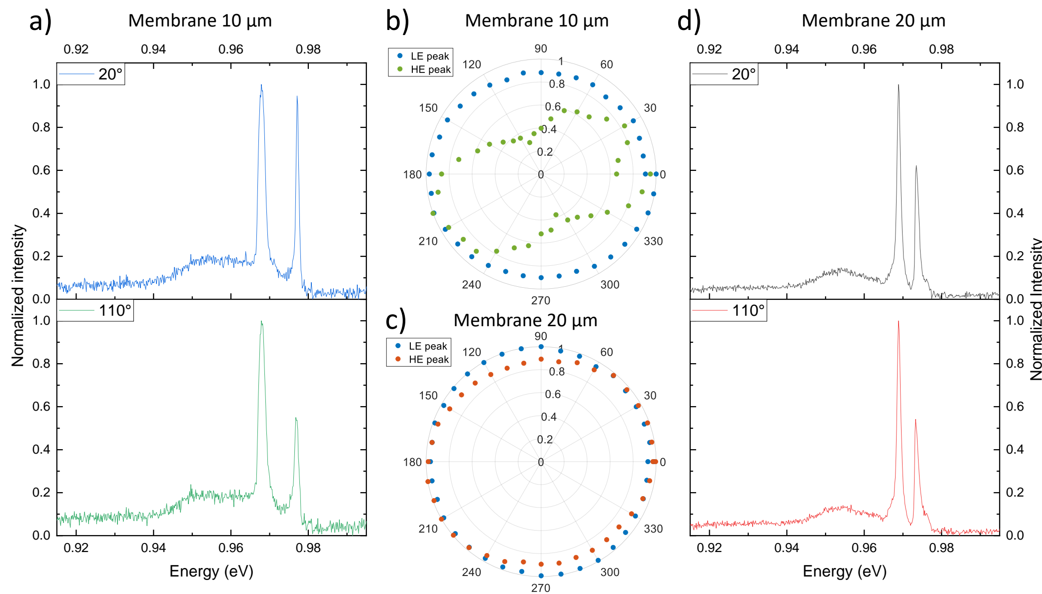

Figure 5.11. a) Low temperature micro-PL spectra measured with a polarizer oriented at 20° (blue curve) and 110° (green curve) at the center of the smallest membrane (λ_{exc} = 532 nm, P_{exc} = 2 mW). The HE peak intensity reduction is evident. b) Polar plot of the LE and HE peak areas as a function of the polarizer rotational angles, measured within a membrane with size 10 µm. The values are obtained integrating over the peak of interest. The HE peak is clearly polarized while the LE peak not. c) Polar plot of the LE and HE peak areas as a function of the polarizer rotational angles, measured within a membrane with size 20 µm. Here the HE peak is only slightly polarized while the LE is not polarized. d) Low temperature micro-PL spectra measured with a polarizer oriented at 20° (black curve) and 110° (red curve) at the center of the biggest membrane (λ_{exc} = 532 nm, P_{exc} = 2 mW). The intensity of the HE peak changes only slightly between the two configurations.

least and in the most strained membranes, i.e. the biggest and smallest ones. The results of these measurements are reported in Fig. 5.11. As we can see, the results from the smallest membrane clearly show that the HE peak is strongly polarized, while the LE peak is not. This is perfectly in agreement with what observed in the literature. Indeed, recalling that the presence of the two PL peaks is connected to the strain component directed vertically and the fact that we measured in backscattering configuration, i.e. the line of sight of our system is the vertical direction, when performing polarization measurements we are scanning the in-plane directions, i.e. perpendicularly to the strain direction. This means that the intensity of the LE peak, which polarization should be parallel to the strain direction, has to be constant while changing the polarizer angle, while the intensity HE peak, which polarization should be perpendicular to the strain direction, has to change and in fact, this is what we observed. Within the biggest membrane the LE peak show a similar behaviour, however the HE peak is only slightly polarized along the same direction as before. Therefore, contrary to what was observed in the past, we find that the degree of polarization of the HE peak is strain dependent.

We have confirmed that even when the strain is applied only locally, i.e. at the microscale, it leads to the formation of two distinguished peaks with different polarization. Moreover, from our measurements it appears that the polarization degree depends on strain and thus,

it could be controlled. Applying our technique to SPEs would be highly appealing since, not only we could easily tune the G-center emission, but we could even select the peak of interest by simply employing a polarizer, thus not needing complex spectral filtering techniques.

5.3 Summary and future developments

To summarize, we have demonstrated the ability to locally tune the G-centers emission wavelength employing strain. Indeed, employing silicon suspended membranes in combination with strained thin films of silicon nitride we have realized a technique to control the splitting of the G-centers ZPL and thus their emission. By changing the membrane size and the silicon nitride deposition parameters, we were able to tune the emission in a $\approx$20 meV range (i.e. a 25 nm range). In addition to that, we have proved that this technique does not worsen the optical quality of the G-centers emission but instead, in some configurations, it enhances the brightness of the emitters. This fabrication technique has other advantages: the local strain control allows to realize emitters at different wavelengths within the same sample, the obtained peaks are polarized along different directions, the sample are fabricated on SOI which is the ideal material for the realization of photonic circuits, and all the employed fabrication techniques are easy to implement and they can be scaled up for mass production with minimal efforts. It is worth mentioning that, to our knowledge, this is the first attempt to tune the G-centers emission employing strain at the microscale.

Despite the several advantages there are still some issues to be solved: the limited brightness of the G-centers, their large linewidth, and the fact that our technique leads to a passive tuning of the G-centers emission. However, we believed that these issues can be solved in straightforward ways.

Concerning the limited brightness our technique can be combined with one of the several technique for the collection enhancement that we have previously described in Chapter 1.5. For example, since we have shown that the two G-centers peak are clearly present within 4 μm from the membrane center (see Figs. 5.9d and e), we could combine the verified collection enhancement effect of the microsphere with the G-centers thus obtaining the desired brightness enhancement.

In relation to the broad linewidth of the G-centers, it can be solved employing SOI based on ^{28}Si. Indeed, the use of an isotopically purified material reduce the emission broadening connected to the presence of different isotopes, which is one of the more relevant contributor to the G-centers emission linewidth in natural silicon. Moreover, this material can be realized with a reduced defects concentration thus leading also to an increase in the emitters brightness.

Regarding the latter issue, we believe it can be solved by employing piezoelectric materials that can be electrically driven. Indeed, the samples can be positioned on top of a piezo actuator which can be exploit to actively change the strain within the system. This approach is well known and it is commonly used with other SPEs such as QDs[202].

Therefore, in the short term the future developments of the technique would be the realization of suspended membrane on SOI with ^{28}Si and in parallel the combination of the realized samples with piezo actuators to verify the feasibility of actively tuning the strain and thus the G-centers emission. Whereas, in the long term, a possible future development would be to reduce the size of the membrane even further in order to verify the limits of

this technique. This would require the use of other fabrication approaches such as EBL, that would complicate the whole technique but would lead to a higher spatial resolution. In parallel to this, our technique could be employed in SOI samples implanted with low carbon doses (better if the SOI is made by ^{28}Si for the aforementioned reasons) in order to obtain the tuning of single and isolated G-centers. It would be of utmost interest to tune the emission of a SPE in such a broad energy range, in such easy way and without worsening its optical properties.

As a final remark, it is worth noting that this technique relies only on strain effects and thus it could be easily employed with all the known luminescence defects in silicon.

Chapter 6

Conclusions and future perspectives

This thesis work was focused on two solid-state SPEs: isolated $GaAs_{1-x}N_x$ QDs and ensembles of G-centers. In order to give some context the concept of SPE was explained in detail and their most important properties thoroughly described. A special attention was dedicated to those techniques which enhance the SPEs emission collection. Within this framework, we have presented the two solid state SPEs studied in this work. In particular, we have described their most relevant properties along with the state of the art techniques that relies on such emitters. In addition to that, we have then presented two novel techniques that we have developed. The first one is focused on the fabrication of $GaAs_{1-x}N_x$ QDs by laser writing them, while the second one is focused on tuning the emission of ensembles of G-centers with strain.

More in detail, the $GaAs_{1-x}N_x$ QDs fabrication technique is based on locally removing the hydrogen from a fully hydrogenated $GaAs_{1-x}N_x$/GaAs QW exploiting PJs, which are intense light beam characterized by a sub-diffraction lateral size that were obtained illuminating silica microspheres with a laser light. We have successfully demonstrated the efficacy of our technique realising several QDs of different size, which were fabricated by simply changing the laser power. The realized QDs were then characterized by means of low temperature micro-PL spectroscopy. Analysing their PL spectra the size of the QDs was evaluated and the expected dependence between this quantity and the laser power was observed. The measured second order autocorrelation function confirms the SPE nature of the QDs realized.

Furthermore, we verified an additional advantage of our technique: the PL collection enhancement. Indeed, we were able to measure that the presence of the microsphere on top of the QDs caused an enhancement in the measured PL of a factor (7.3 ± 0.7). By performing angular measurements we were able to attribute the enhancement to an increase in the directionality of the emission, which was further confirmed by FDTD simulations.

In this work we have shown the efficacy of this novel $GaAs_{1-x}N_x$ QDs fabrication technique and its main advantages: the fabrication process is performed in air and at room temperature, no lithographic process are needed, the technique shows an intrinsic broadband enhancement of the collected emission, the size of the fabricated QDs can be easily controlled and, above all, this fabrication technique is reversible. Indeed, by hydrogenating the QW, the QDs can be cancelled and the process can be performed once again, for example, employing different fabrication parameters. Along with these advantages we have illustrated the limitation of the technique and their possible solutions.

The possible further developments for these technique are several. The first one would be to increase the control over the QDs properties by finely tuning the PJs employed for their fabrication. To this end, we have realized and presented a detailed series of simulations to study the PJs properties as a function of the laser wavelength and microsphere radius. Therefore, by carefully selecting the wavelength-radius combinations we should be able to achieve a much higher control over the whole fabrication process. Another future application of our technique could be the realization of site-controlled $GaAs_{1-x}N_x$ QDs. This could be achieved by engineering the sample surface to force the microsphere positioning or by simply positioning them, one by one, with a nanopositioner. In this direction an attempt is currently under study. This development is of interest for the realization of a $GaAs_{1-x}N_x$ QD embedded in a photonic crystal cavity to reduce its radiative lifetime and thus, increasing its achievable brightness. Lastly, an interesting development would be the realization of complex structures based on QDs such as a QD molecule or a QD array. The former can be realized by illuminating the microsphere at different angles. Indeed, we have shown that a tilt in the illumination results in a shift of the PJs and thus a shift in position of the fabricated QD. The latter, instead, can be realize by packing the microsphere in an honeycomb structure and illuminating them with a laser light in a single shot. This application would be of utmost interest for the large scale fabrication of SPEs to be employed in QIT.

The second technique that we have developed and presented in this thesis work is a novel approach to locally tune the G-centers emission with strain. This was achieved by realizing suspended silicon membranes from a SOI sample and by depositing on top of them a strained SiN_x layer which, in turn, introduced strain within the silicon layer. By changing the membranes size we were able to tune the G-centers emission within a 20 meV energy range.

The low temperature micro-PL measurements performed on the G-centers implanted in the membranes showed the splitting of the ZPL in two different peaks. Such energy splitting is clearly dependent on the membrane size and on the amount of strain present in the SiN_x layer. Regarding the latter, we have observed that, at least in two samples, there is a linear relation between the energy splitting and the nominal amount of strain within the sample. We have investigated the physical origin of this phenomenon performing FEM simulations and TRPL measurements. From the latter, it resulted that the two peaks show a similar radiative decay and hence, they have the same physical origin. While from the former, it resulted that in the membranes there is the presence of an out-of-plane strain component that break the symmetry of the system. Therefore, we have concluded that the presence of the two emissions arises from the removal of the degenerancy of the G-centers energy level, due to strain. This is further confirmed by the fact that we have observed the two peaks splitting independently from the SiN_x strain nature, i.e. tensile or compressive.

To the best of our knowledge, the technique presented in this work represents the first attempt to locally tune the G-centers emission with strain. The possibility to achieve such control at the microscale leads to being able to realize several SPEs, all characterized by a controlled emission energy, within the same sample. This is one of the various advantages that our technique presents. First of all, both the membrane fabrication process and the presence of the SiN_x layer does not worsen the G-centers emission. This was verified both measuring the PL intensity and the radiative decay time, which was consistent with the one measured in untreated samples. Another clear advantage is that this technique can be easily scaled up, indeed all the fabrication steps relies on commercial processes that are commonly diffused in semiconductor technologies. To this end, it is worth noting that this technique is

realized on SOI, which is the ideal material for the realization of photonic structures within which embedding the G-centers. Lastly, it is interesting to note that this technique could be easily employed with all the other luminescent point defects within silicon.

Even for this second technique there are some further developments which could be of interest. First of all, the limits of the technique should be tested, for example by increasing the range of membranes sizes employed. To this end, several samples are under fabrication and they will be tested in the near future. In parallel to this, it would be interesting to realize an active control of the strain within our samples. Indeed, the membranes acts as passive stressors, therefore, once created the amount of strain introduced within them cannot be easily modified. The active strain control is typically performed employing piezoelectric materials which can be easily controlled modifying the voltage across them. To this end, a first attempt could be to attach the sample on a piezo actuator to actively modify the strain value. Lastly, as said before, it would be highly interesting to apply this technique to other radiative emitting defects in silicon, such as the W-centers or the T-centers.

It is undoubtedly that solid state SPEs represent the most appealing single photon sources for QIT applications. Therefore, it is of utmost importance to design techniques for their realization and their control. With this in mind, we have designed and realized the two techniques presented in this work, which represent a small step forward towards the large scale implementation of Quantum Information Technologies.

Appendix A

$GaAs_{1-x}N_x$/GaAs quantum well

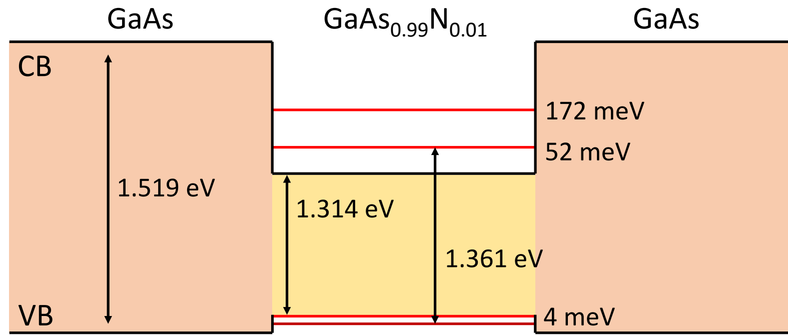

Figure A.1. Scheme of the band alignment of a $GaAs_{1-x}N_x$/GaAs QW with the same nominal characteristics as the one employed in this work.

In Fig. A.1 is reported a scheme of the band alignment in a QW with the same characteristics as the one employed for the fabrication of $GaAs_{1-x}N_x$ QDs. The reported energy values are calculated from the measurements as follows. The energy gap of GaAs is well known and accurately measured and at 10 K its value is 1.519 eV[203]. The $GaAs_{1-x}N_x$ energy gap as a function of temperature and nitrogen concentration was measured by Uesugi et al.[91]. From their measurements we can extract the value of the energy gap at 10 K and for a nitrogen concentration of about 1.1%: $E_g = 1.314$ eV. The difference between the valence band maxima V_h is obtained from density functional theory (DFT) simulations and for a nitrogen concentration of 1% $V_h = 7$ meV[204]. Therefore we can calculate the difference between the conduction band minima of the two elements: $V_e = E_g^{GaAs} - E_g^{GaAsN} - V_h = 198$ meV. From the two confinement potentials V_h and V_e we can calculate the confinement energies for electrons and holes. Indeed, assuming that they are characterized by a constant effective masses of $m_e^* = 0.14\, m_0$ and $m_h^* = 0.63\, m_0$, with m_0 the electron mass in vacuum, and a QW width of 6 nm we can easily calculate $E_e = 52$ meV and $E_h = 4$ meV. Once calculated these values we can estimate the QW exciton energy transition, E_X, which is given by: $E_X = E_g^{GaAsN} + E_e + E_h - E_b = 1.36$ eV, where E_b is the exciton binding energy which is ~ 10 meV[205]. However, this value differs of about 60 meV from what we observed (see Fig. 4.3). This difference likely arise from an actually higher nitrogen concentration within the $GaAs_{1-x}N_x$ layer. Another plausible explanation is the extension of the density of state within the band gap due to the presence of localized states originated by disorder in the

material.

The reduced confinement potentials of the carriers, especially the holes, gives an upper limit for the temperature at which we can observe the $GaAs_{1-x}N_x$ PL which is about 100 K.

Appendix B

Evaluation of the quantum dots diameter

We report here the simple model employed for estimate the fabricated $GaAs_{1-x}N_x$ QDs sizes[116]. The model relies on assuming a cylindrical shape for our QDs, which is reasonable since the PJs employed for their fabrication maintain a cylindrical shape along all the sample QW. We consider that they are characterized by the same thickness as the QW, i.e. 6 nm, and by a radius R, which is determined by the fabrication parameters. The emission energies of an exciton in a QW of thickness L and in a cylindrical QD with the same thickness and radius R are:

$$E^{QW} = E_g + E_L - E_b^{QW} \tag{B.1}$$

and

$$E^{QD} = E_g + E_L + E_R - E_b^{QD} \tag{B.2}$$

where E_g is the energy gap, E_L and E_R are the confinement energies along the vertical and radial direction, respectively, E_b^{QW} and E_b^{QD} are the exciton binding energies for the QD and QW, respectively. Therefore, the difference between the two exciton emissions is given by:

$$\Delta E = E_R - (E_b^{QD} - E_b^{QW}) \tag{B.3}$$

where ΔE can be experimentally determined by the spectra in Fig. 4.3a and the expression for E_R as a function of R is given by[206]:

$$E_R = b\frac{\hbar^2 u_{mp}^2}{2m^* R^2} \tag{B.4}$$

where u_{mp}^2 is the $p-$th zero of the $m-$th Bessel function (J_m) and $m_e^* = 0.14m_0$ is the electron efective mass in $GaAs_{1-x}N_x$ (m_0 being the electron mass)[207, 95] and b is a factor to take into account the finite barrier around the dot (about 200 meV for the electrons). Considering the lowest energy level $u_{01} \approx 2.4018$, whereas, assuming that b is the same of the vertical direction we have $b = 0.63$. Such value is given by the ratio of the electron confinement energies calculated for the $GaAs_{1-x}N_x$/GaAs QW with finite and infinite potential barriers. We are neglecting the hole confinement contribution since they are subjected to a much lower confinement potential (about 7 meV)[204].

The lowest energy exciton in a QW with the same characteristics as ours has been demonstrated to have $E_b^{QW} \sim 10\,\mathrm{meV}$[205]. However, no value has been reported in literature for E_b^{QD}. We can assume its value to be $E_b^{QD} \approx 20\,\mathrm{meV}$ considering that in other $III - V$ systems the binding energy of the exciton is approximately two times the one observed in the corresponding QW of comparable thickness[208].

Therefore, we can easily evaluate the QD diameter, 2R, by reversing Eq. B.3 and combining it with Eq. B.2 thus obtaining:

$$2R = \sqrt{\frac{2b\hbar^2 u_{01}^2}{m^*(\Delta E + E_b^{QD} - E_b^{QW})}} \tag{B.5}$$

Considering the spectra showed in Fig. 4.3a we obtain the following ΔE values: 29 meV, 40 meV, 49 meV and 77 meV. These values are obtained with fabrication power of 70, 66, 62 and 58 mW and they correspond to a QD diameter of: 10, 8.9, 8.2 and 6.7 nm, respectively. In Fig. 4.3b the plot of the QD diameter as a function of the fabrication power is shown. Such small QD sizes confirm our ability to remove hydrogen from an area much smaller than the diffraction limit with our technique.

Appendix C

Second-order autocorrelation fitting model

In Fig. C.1 are reported the available states for the QD which are considered in the model that we will describe in the following. When exciting the sample with a pulsed excitation the delta-like pulse generates a population of electron-holes ($e-h$) pairs in a reservoir, from which carriers are transferred to the QD with capture rate $\gamma_{cap} = 1/\tau_{cap}$, which is set equal for both electron and holes. As a consequence the probability of finding an electron or a hole in the reservoir evolves as $p_{e/h} = e^{-(t+\Delta t)/t_{cap}}$ over time (assuming that no other mechanism causes the decay of the reservoir population). The parameter Δt allows us to set a delay between the excitation time and the origin of the time axis, which is crucial to properly fit the experimental data.

The carriers then populates the ladder of possible QD occupation states, as sketched in Fig. C.1. Capturing the carrier from the reservoir the system moves up in the ladder (horizontal and/or vertical arrows) with rate $\gamma_{cap} \cdot p_{e/h}$. While, through recombination of the $e-h$ pairs the number of carriers in the QD decreases (diagonal arrows) with rate $\gamma_{rec} = 1/\tau_{rec}$ (this takes into account both radiative and non radiative processes). Therefore the QD dynamics can be obtained by solving a system of rate equations accounting for all the phenomena just described and sketched in Fig. C.1 (i.e. carriers captures, recombination and relaxation). The solutions of this system of equations are the the probabilities, $p_i(t)$, of finding the QD in its i different occupation states.

Considering for simplicity the time positive axis ($t > 0$) the autocorrelation histogram for a given QD state, $g^{(2)}_{AA}(\tau)$, can be obtained from the corresponding state occupation probabilities, p_A, by analyzing the process resulting in the collection of an autocorrelation count: (*i*) following the excitation of an empty QD-reservoir system by a laser pulse, a first photon corresponding to the transition associated with the state A is detected. The probability of observing such a photon after a time $\Delta\tau$ is proportional to $p_A(\Delta\tau)$, as obtained by solving the QD rate equations with the system initially empty. (*ii*) At this point, the QD is in the state resulting from the recombination of an $e-h$ pair from state A. In addition to that, the fact that a time $\Delta\tau$ is passed from the last laser pulse has to be taken into account when evaluating $p_{e/h}$ and thus, the carrier capture rates. To find the probability of observing a second photon connected to the state A after a given time τ from the observation of the first photon, the system of rate equations that has to be solved is bound to a series of conditions such that its solution takes the form of a conditional probability, $p_A(\tau|\Delta\tau)$. Weighting this

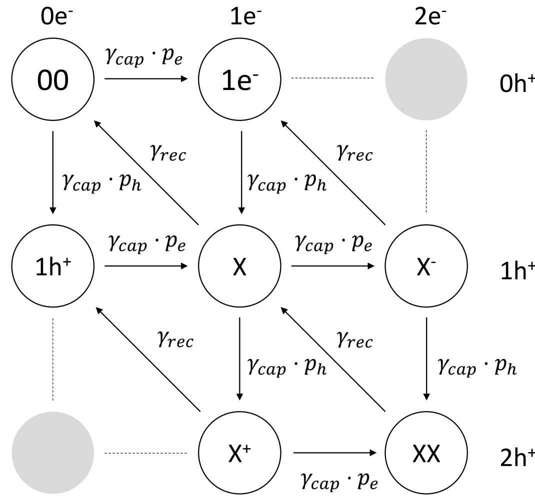

Figure C.1. Scheme of the ladder of available QD states taken into account in the second order aturocorrelation fit model. In the sketch are shown also the associated recombination and capture rate γ_{rec} and γ_{cap}, respectively.

conditional probability with $p_A(\tau)$ and integrating over all the possible $\Delta\tau$ values we obtain:

$$g_{AA}^{(2),\tau_p=0}(\tau) = \int_0^\infty p_A(\tau|\Delta\tau)p_A(\tau)d\Delta\tau \tag{C.1}$$

However, this equation accounts only for the central peak of the autocorrelation histogram, center at $\tau_p = 0$. For a time delay equal to $n\tau_{rep}$ (where n is an integer and τ_{rep} is the reverse of the laser repetition rate) the arrival of a new excitation pulse automatically "reset" the QD dynamics, so that for the other peaks of the $g_{AA}^{(2)}(\tau)$ we can write:

$$g_{AA}^{(2),\tau_p=n\tau_{rep}}(\tau) = \int_0^\infty p_A(\tau - n\tau_{rep} + \tau')p_A(-\tau')d\tau' \tag{C.2}$$

where n= $1 \ldots \infty$ and both p_A values are obtained by solving the system of rate equations for $\Delta\tau = 0$ and with the QD in its empty state.

By summing over n and considering that $g_{AA}^{(2)}(\tau) = g_{AA}^{(2)}(-\tau)$, we finally get:

$$\begin{cases} g_{AA}^{(2)}(\tau) = g_{AA}^{(2),\tau_p=0}(\tau) + \sum_{n=1}^{\infty} g_{AA}^{(2),\tau_p=n\tau_{re}}(\tau) \\ g_{AA}^{(2)}(\tau) = g_{AA}^{(2)}(-\tau) \end{cases} \tag{C.3}$$

The curve showed in Fig. 4.6 is obtained by fitting Eq. C.3 to the experimental data with τ_{cap} and τ_{rec} as the only fitting parameters.

Bibliography

[1] I. Aharonovich, D. Englund, and M. Toth, “Solid-state single-photon emitters,” *Nature Photonics*, vol. 10, pp. 631–641, sep 2016.

[2] P. Lodahl, S. Mahmoodian, and S. Stobbe, “Interfacing single photons and single quantum dots with photonic nanostructures,” *Reviews of Modern Physics*, vol. 87, pp. 347–400, may 2015.

[3] J. L. O'Brien, A. Furusawa, and J. Vučković, “Photonic quantum technologies,” *Nature Photonics*, vol. 3, pp. 687–695, dec 2009.

[4] W. B. Gao, A. Imamoglu, H. Bernien, and R. Hanson, “Coherent manipulation, measurement and entanglement of individual solid-state spins using optical fields,” *Nature Photonics*, vol. 9, pp. 363–373, may 2015.

[5] T. E. Northup and R. Blatt, “Quantum information transfer using photons,” *Nature Photonics*, vol. 8, pp. 356–363, apr 2014.

[6] S. Buckley, K. Rivoire, and J. Vučković, “Engineered quantum dot single-photon sources,” *Reports on Progress in Physics*, vol. 75, p. 126503, nov 2012.

[7] M. A. Nielsen and I. L. Chuang, *Quantum Computation and Quantum Information*. Cambridge University Press, jun 2012.

[8] N. Gisin, G. Ribordy, W. Tittel, and H. Zbinden, “Quantum cryptography,” *Reviews of Modern Physics*, vol. 74, pp. 145–195, mar 2002.

[9] S. Pirandola, U. L. Andersen, L. Banchi, M. Berta, D. Bunandar, R. Colbeck, D. Englund, T. Gehring, C. Lupo, C. Ottaviani, J. L. Pereira, M. Razavi, J. S. Shaari, M. Tomamichel, V. C. Usenko, G. Vallone, P. Villoresi, and P. Wallden, “Advances in quantum cryptography,” *Advances in Optics and Photonics*, vol. 12, p. 1012, dec 2020.

[10] T. Heindel, C. A. Kessler, M. Rau, C. Schneider, M. Fürst, F. Hargart, W.-M. Schulz, M. Eichfelder, R. Roßbach, S. Nauerth, M. Lermer, H. Weier, M. Jetter, M. Kamp, S. Reitzenstein, S. Höfling, P. Michler, H. Weinfurter, and A. Forchel, “Quantum key distribution using quantum dot single-photon emitting diodes in the red and near infrared spectral range,” *New Journal of Physics*, vol. 14, p. 083001, aug 2012.

[11] T. D. Ladd, F. Jelezko, R. Laflamme, Y. Nakamura, C. Monroe, and J. L. O’Brien, “Quantum computers,” *Nature*, vol. 464, pp. 45–53, mar 2010.

[12] S. S. Gill, A. Kumar, H. Singh, M. Singh, K. Kaur, M. Usman, and R. Buyya, "Quantum computing: A taxonomy, systematic review and future directions," *Software: Practice and Experience*, vol. 52, pp. 66–114, oct 2021.

[13] J. L. O'Brien, "Optical quantum computing," *Science*, vol. 318, pp. 1567–1570, dec 2007.

[14] A. Beveratos, R. Brouri, T. Gacoin, A. Villing, J.-P. Poizat, and P. Grangier, "Single photon quantum cryptography," *Physical Review Letters*, vol. 89, p. 187901, oct 2002.

[15] F. B. Basset, M. Valeri, E. Roccia, V. Muredda, D. Poderini, J. Neuwirth, N. Spagnolo, M. B. Rota, G. Carvacho, F. Sciarrino, and R. Trotta, "Quantum key distribution with entangled photons generated on demand by a quantum dot," *Science Advances*, vol. 7, p. eabe6379, mar 2021.

[16] Y. Cao, Y. Zhao, Q. Wang, J. Zhang, S. X. Ng, and L. Hanzo, "The evolution of quantum key distribution networks: On the road to the qinternet," *IEEE Communications Surveys & Tutorials*, vol. 24, no. 2, pp. 839–894, 2022.

[17] H. J. Kimble, M. Dagenais, and L. Mandel, "Photon antibunching in resonance fluorescence," *Physical Review Letters*, vol. 39, pp. 691–695, sep 1977.

[18] F. Diedrich and H. Walther, "Nonclassical radiation of a single stored ion," *Physical Review Letters*, vol. 58, pp. 203–206, jan 1987.

[19] A. Kuhn, M. Hennrich, and G. Rempe, "Deterministic single-photon source for distributed quantum networking," *Physical Review Letters*, vol. 89, p. 067901, jul 2002.

[20] M. Keller, B. Lange, K. Hayasaka, W. Lange, and H. Walther, "Continuous generation of single photons with controlled waveform in an ion-trap cavity system," *Nature*, vol. 431, pp. 1075–1078, oct 2004.

[21] P. G. Kwiat, K. Mattle, H. Weinfurter, A. Zeilinger, A. V. Sergienko, and Y. Shih, "New high-intensity source of polarization-entangled photon pairs," *Physical Review Letters*, vol. 75, pp. 4337–4341, dec 1995.

[22] T. Pittman, B. Jacobs, and J. Franson, "Heralding single photons from pulsed parametric down-conversion," *Optics Communications*, vol. 246, pp. 545–550, feb 2005.

[23] C. Couteau, "Spontaneous parametric down-conversion," *Contemporary Physics*, vol. 59, pp. 291–304, jul 2018.

[24] X.-L. Wang, L.-K. Chen, W. Li, H.-L. Huang, C. Liu, C. Chen, Y.-H. Luo, Z.-E. Su, D. Wu, Z.-D. Li, H. Lu, Y. Hu, X. Jiang, C.-Z. Peng, L. Li, N.-L. Liu, Y.-A. Chen, C.-Y. Lu, and J.-W. Pan, "Experimental ten-photon entanglement," *Physical Review Letters*, vol. 117, p. 210502, nov 2016.

[25] M. Atatüre, D. Englund, N. Vamivakas, S.-Y. Lee, and J. Wrachtrup, "Material platforms for spin-based photonic quantum technologies," *Nature Reviews Materials*, vol. 3, pp. 38–51, apr 2018.

[26] I. Aharonovich, S. Castelletto, D. A. Simpson, C.-H. Su, A. D. Greentree, and S. Prawer, "Diamond-based single-photon emitters," *Reports on Progress in Physics*, vol. 74, p. 076501, jun 2011.

[27] A. Lohrmann, B. C. Johnson, J. C. McCallum, and S. Castelletto, "A review on single photon sources in silicon carbide," *Reports on Progress in Physics*, vol. 80, p. 034502, jan 2017.

[28] M. E. Bathen and L. Vines, "Manipulating single-photon emission from point defects in diamond and silicon carbide," *Advanced Quantum Technologies*, vol. 4, p. 2100003, may 2021.

[29] A. Durand, Y. Baron, W. Redjem, T. Herzig, A. Benali, S. Pezzagna, J. Meijer, A. Kuznetsov, J.-M. Gérard, I. Robert-Philip, M. Abbarchi, V. Jacques, G. Cassabois, and A. Dréau, "Broad diversity of near-infrared single-photon emitters in silicon," *Physical Review Letters*, vol. 126, p. 083602, feb 2021.

[30] X. He, H. Htoon, S. K. Doorn, W. H. P. Pernice, F. Pyatkov, R. Krupke, A. Jeantet, Y. Chassagneux, and C. Voisin, "Carbon nanotubes as emerging quantum-light sources," *Nature Materials*, vol. 17, pp. 663–670, jun 2018.

[31] A. Sajid, M. J. Ford, and J. R. Reimers, "Single-photon emitters in hexagonal boron nitride: a review of progress," *Reports on Progress in Physics*, vol. 83, p. 044501, mar 2020.

[32] M. Toth and I. Aharonovich, "Single photon sources in atomically thin materials," *Annual Review of Physical Chemistry*, vol. 70, pp. 123–142, jun 2019.

[33] K. Parto, S. I. Azzam, K. Banerjee, and G. Moody, "Defect and strain engineering of monolayer WSe2 enables site-controlled single-photon emission up to 150 k," *Nature Communications*, vol. 12, jun 2021.

[34] P. Michler, ed., *Single Semiconductor Quantum Dots*. Springer Berlin Heidelberg, 2009.

[35] S. Hepp, M. Jetter, S. L. Portalupi, and P. Michler, "Semiconductor quantum dots for integrated quantum photonics," *Advanced Quantum Technologies*, vol. 2, no. 9, p. 1900020, 2019.

[36] J. Lee, V. Leong, D. Kalashnikov, J. Dai, A. Gandhi, and L. A. Krivitsky, "Integrated single photon emitters," *AVS Quantum Science*, vol. 2, p. 031701, oct 2020.

[37] S. Zhao, J. Lavie, L. Rondin, L. Orcin-Chaix, C. Diederichs, P. Roussignol, Y. Chassagneux, C. Voisin, K. Müllen, A. Narita, S. Campidelli, and J.-S. Lauret, "Single photon emission from graphene quantum dots at room temperature," *Nature Communications*, vol. 9, p. 3470, aug 2018.

[38] Y.-S. Park, S. Guo, N. S. Makarov, and V. I. Klimov, "Room temperature single-photon emission from individual perovskite quantum dots," *ACS Nano*, vol. 9, pp. 10386–10393, sep 2015.

[39] M. J. Holmes, K. Choi, S. Kako, M. Arita, and Y. Arakawa, “Room-temperature triggered single photon emission from a III-nitride site-controlled nanowire quantum dot,” *Nano Letters*, vol. 14, pp. 982–986, jan 2014.

[40] K. D. Sattler, ed., *Handbook of Nanophysics*. CRC Press, 2011.

[41] P. Senellart, G. Solomon, and A. White, “High-performance semiconductor quantum-dot single-photon sources,” *Nature Nanotechnology*, vol. 12, pp. 1026–1039, nov 2017.

[42] N. Somaschi, V. Giesz, L. D. Santis, J. C. Loredo, M. P. Almeida, G. Hornecker, S. L. Portalupi, T. Grange, C. Antón, J. Demory, C. Gómez, I. Sagnes, N. D. Lanzillotti-Kimura, A. Lemaítre, A. Auffeves, A. G. White, L. Lanco, and P. Senellart, “Near-optimal single-photon sources in the solid state,” *Nature Photonics*, vol. 10, pp. 340–345, mar 2016.

[43] F. Liu, A. J. Brash, J. O’Hara, L. M. P. P. Martins, C. L. Phillips, R. J. Coles, B. Royall, E. Clarke, C. Bentham, N. Prtljaga, I. E. Itskevich, L. R. Wilson, M. S. Skolnick, and A. M. Fox, “High purcell factor generation of indistinguishable on-chip single photons,” *Nat. Nanotechnol.*, vol. 13, pp. 835–840, jul 2018.

[44] K. H. Madsen, S. Ates, A. Javadi, S. M. Albrecht, I. Yeo, S. Stobbe, and P. Lodahl, “Efficient out-coupling of high-purity single photons from a coherent quantum dot in a photonic-crystal cavity,” *Phys. Rev. B*, vol. 90, p. 155303, oct 2014.

[45] J. Claudon, J. Bleuse, N. S. Malik, M. Bazin, P. Jaffrennou, N. Gregersen, C. Sauvan, P. Lalanne, and J. M. Gèrard, “A highly efficient single-photon source based on a quantum dot in a photonic nanowire,” *Nat. Photonics*, vol. 4, pp. 174–177, jan 2010.

[46] O. J. Trojak, S. I. Park, J. D. Song, and L. Sapienza, “Metallic nanorings for broad-band, enhanced extraction of light from solid-state emitters,” *Applied Physics Letters*, vol. 111, p. 021109, jul 2017.

[47] O. J. Trojak, C. Woodhead, S.-I. Park, J. D. Song, R. J. Young, and L. Sapienza, “Combined metallic nano-rings and solid-immersion lenses for bright emission from single InAs/GaAs quantum dots,” *Applied Physics Letters*, vol. 112, p. 221102, may 2018.

[48] A. Ristori, T. Hamilton, D. Toliopoulos, M. Felici, G. Pettinari, S. Sanguinetti, M. Gurioli, H. Mohseni, and F. Biccari, “Photonic jet writing of quantum dots self-aligned to dielectric microspheres,” *Advanced Quantum Technologies*, vol. 4, p. 2100045, jul 2021.

[49] M. Gschrey, A. Thoma, P. Schnauber, M. Seifried, R. Schmidt, B. Wohlfeil, L. Krüger, J. H. Schulze, T. Heindel, S. Burger, F. Schmidt, A. Strittmatter, S. Rodt, and S. Reitzenstein, “Highly indistinguishable photons from deterministic quantum-dot microlenses utilizing three-dimensional in situ electron-beam lithography,” *Nature Communications*, vol. 6, p. 7662, jul 2015.

[50] P. Stepanov, A. Delga, N. Gregersen, E. Peinke, M. Munsch, J. Teissier, J. Mørk, M. Richard, J. Bleuse, J. M. Gérard, and J. Claudon, "Highly directive and gaussian far-field emission from "giant" photonic trumpets," *Appl. Phys. Lett.*, vol. 107, p. 141106, oct 2015.

[51] K. A. Serrels, E. Ramsay, P. A. Dalagarno, B. Gerardot, J. A. O'Connor, R. H. Hadfield, J. Warburton, and D. T. Reid, "Solid immersion lens applications for nanophotonic devices," *J. Nanophotonics*, vol. 2, p. 021854, dec 2008.

[52] G. Ciatto, ed., *Hydrogenated Dilute Nitride Semiconductors*. Jenny Stanford Publishing, apr 2015.

[53] A. Ristori, M. Felici, G. Pettinari, L. Pattelli, and F. Biccari, "Photonic jets and single-photon emitters," *Advanced Photonics Research*, vol. n/a, no. n/a, p. 2100365, 2022.

[54] R. Loudon, *The quantum theory of light*. OUP Oxford, 2000.

[55] A. A. Michelson and E. W. Morley, "On the relative motion of the earth and of the luminiferous ether," *Sidereal Messenger, vol. 6, pp. 306-310*, vol. 6, pp. 306–310, 1887.

[56] R. H. Brown and R. Q. Twiss, "Correlation between photons in two coherent beams of light," *Nature*, vol. 177, pp. 27–29, jan 1956.

[57] D. F. Walls, "Squeezed states of light," *Nature*, vol. 306, pp. 141–146, nov 1983.

[58] D. Istrati, Y. Pilnyak, J. C. Loredo, C. Antón, N. Somaschi, P. Hilaire, H. Ollivier, M. Esmann, L. Cohen, L. Vidro, C. Millet, A. Lemaître, I. Sagnes, A. Harouri, L. Lanco, P. Senellart, and H. S. Eisenberg, "Sequential generation of linear cluster states from a single photon emitter," *Nature Communications*, vol. 11, p. 5501, oct 2020.

[59] J. B. Spring, B. J. Metcalf, P. C. Humphreys, W. S. Kolthammer, X.-M. Jin, M. Barbieri, A. Datta, N. Thomas-Peter, N. K. Langford, D. Kundys, J. C. Gates, B. J. Smith, P. G. R. Smith, and I. A. Walmsley, "Boson sampling on a photonic chip," *Science*, vol. 339, no. 6121, pp. 798–801, 2013.

[60] M. Tillmann, B. Dakić, R. Heilmann, S. Nolte, A. Szameit, and P. Walther, "Experimental boson sampling," *Nature Photonics*, vol. 7, pp. 540–544, may 2013.

[61] K. Azuma, K. Tamaki, and H.-K. Lo, "All-photonic quantum repeaters," *Nature Communications*, vol. 6, apr 2015.

[62] Y.-M. He, Y. He, Y.-J. Wei, D. Wu, M. Atatüre, C. Schneider, S. Höfling, M. Kamp, C.-Y. Lu, and J.-W. Pan, "On-demand semiconductor single-photon source with near-unity indistinguishability," *Nature Nanotechnology*, vol. 8, pp. 213–217, feb 2013.

[63] C. K. Hong, Z. Y. Ou, and L. Mandel, "Measurement of subpicosecond time intervals between two photons by interference," *Physical Review Letters*, vol. 59, pp. 2044–2046, nov 1987.

[64] S. G. Lukishova and L. J. Bissell, “Nanophotonic advances for room-temperature single-photon sources,” *Chapter of: "Quantum Photonics: Pioneering Advances and Emerging Applications" by Boyd R. W. et al. (eds.)*, pp. 103–178, 2019.

[65] P. Kok, W. J. Munro, K. Nemoto, T. C. Ralph, J. P. Dowling, and G. J. Milburn, “Linear optical quantum computing with photonic qubits,” *Rev. Mod. Phys.*, vol. 79, pp. 135–174, jan 2007.

[66] J. Liu, R. Su, Y. Wei, B. Yao, S. F. C. da Silva, Y. Yu, J. Iles-Smith, K. Srinivasan, A. Rastelli, J. Li, and X. Wang, “A solid-state source of strongly entangled photon pairs with high brightness and indistinguishability,” *Nature Nanotechnology*, vol. 14, pp. 586–593, apr 2019.

[67] D. Huber, M. Reindl, Y. Huo, H. Huang, J. S. Wildmann, O. G. Schmidt, A. Rastelli, and R. Trotta, “Highly indistinguishable and strongly entangled photons from symmetric GaAs quantum dots,” *Nature Communications*, vol. 8, may 2017.

[68] G. Kiršanskė, H. Thyrrestrup, R. S. Daveau, C. L. Dreeßen, T. Pregnolato, L. Midolo, P. Tighineanu, A. Javadi, S. Stobbe, R. Schott, A. Ludwig, A. D. Wieck, S. I. Park, J. D. Song, A. V. Kuhlmann, I. Söllner, M. C. Löbl, R. J. Warburton, and P. Lodahl, “Indistinguishable and efficient single photons from a quantum dot in a planar nanobeam waveguide,” *Physical Review B*, vol. 96, p. 165306, oct 2017.

[69] Ł. Dusanowski, S.-H. Kwon, C. Schneider, and S. Höfling, “Near-unity indistinguishability single photon source for large-scale integrated quantum optics,” *Physical Review Letters*, vol. 122, p. 173602, may 2019.

[70] H.-S. Zhong, Y. Li, W. Li, L.-C. Peng, Z.-E. Su, Y. Hu, Y.-M. He, X. Ding, W. Zhang, H. Li, L. Zhang, Z. Wang, L. You, X.-L. Wang, X. Jiang, L. Li, Y.-A. Chen, N.-L. Liu, C.-Y. Lu, and J.-W. Pan, “12-photon entanglement and scalable scattershot boson sampling with optimal entangled-photon pairs from parametric down-conversion,” *Physical Review Letters*, vol. 121, p. 250505, dec 2018.

[71] S. I. Bogdanov, M. Y. Shalaginov, A. S. Lagutchev, C.-C. Chiang, D. Shah, A. S. Baburin, I. A. Ryzhikov, I. A. Rodionov, A. V. Kildishev, A. Boltasseva, and V. M. Shalaev, “Ultrabright room-temperature sub-nanosecond emission from single nitrogen-vacancy centers coupled to nanopatch antennas,” *Nano Letters*, vol. 18, pp. 4837–4844, jul 2018.

[72] T. Schröder, F. Gädeke, M. J. Banholzer, and O. Benson, “Ultrabright and efficient single-photon generation based on nitrogen-vacancy centres in nanodiamonds on a solid immersion lens,” *New Journal of Physics*, vol. 13, p. 055017, may 2011.

[73] D. Najer, I. Söllner, P. Sekatski, V. Dolique, M. C. Löbl, D. Riedel, R. Schott, S. Starosielec, S. R. Valentin, A. D. Wieck, N. Sangouard, A. Ludwig, and R. J. Warburton, “A gated quantum dot strongly coupled to an optical microcavity,” *Nature*, vol. 575, pp. 622–627, Oct. 2019.

[74] C. Haws, E. Perez, M. Davanco, J. D. Song, K. Srinivasan, and L. Sapienza, “Broadband, efficient extraction of quantum light by a photonic device comprised of a

metallic nano-ring and a gold back reflector," *Applied Physics Letters*, vol. 120, p. 081103, Feb. 2022.

[75] L. Sapienza, M. Davanço, A. Badolato, and K. Srinivasan, "Nanoscale optical positioning of single quantum dots for bright and pure single-photon emission," *Nature Communications*, vol. 6, p. 7833, jul 2015.

[76] O. Gazzano, S. Michaelis de Vasconcellos, C. Arnold, A. Nowak, E. Galopin, I. Sagnes, L. Lanco, A. Lemaître, and P. Senellart, "Bright solid-state sources of indistinguishable single photons," *Nat. Commun.*, vol. 4, p. 1425, feb 2012.

[77] M. Sartison, S. L. Portalupi, T. Gissibl, M. Jetter, H. Giessen, and P. Michler, "Combining in-situ lithography with 3D printed solid immersion lenses for single quantum dot spectroscopy," *Sci. Rep.*, vol. 7, p. 39916, jan 2017.

[78] M. Sartison, L. Engel, S. Kolatschek, F. Olbrich, C. Nawrath, S. Hepp, M. Jetter, P. Michler, and S. L. Portalupi, "Deterministic integration and optical characterization of telecom O-band quantum dots embedded into wet-chemically etched Gaussian-shaped microlenses," *Appl. Phys. Lett.*, vol. 113, p. 032103, jul 2018.

[79] A. Dousse, L. Lanco, J. Suffczyński, E. Semenova, A. Miard, A. Lemaître, I. Sagnes, C. Roblin, J. Bloch, and P. Senellart, "Controlled light-matter coupling for a single quantum dot embedded in a pillar microcavity using far-field optical lithography," *Physical Review Letters*, vol. 101, p. 267404, dec 2008.

[80] K. Beha, H. Fedder, M. Wolfer, M. C. Becker, P. Siyushev, M. Jamali, A. Batalov, C. Hinz, J. Hees, L. Kirste, H. Obloh, E. Gheeraert, B. Naydenov, I. Jakobi, F. Dolde, S. Pezzagna, D. Twittchen, M. Markham, D. Dregely, H. Giessen, J. Meijer, F. Jelezko, C. E. Nebel, R. Bratschitsch, A. Leitenstorfer, and J. Wrachtrup, "Diamond nanophotonics," *Beilstein Journal of Nanotechnology*, vol. 3, pp. 895–908, dec 2012.

[81] S. Moehl, H. Zhao, B. Dal Don, S. Watcher, and H. Kalt, "Solid immersion lens-enhanced nano-photoluminescence: Principle and applications," *J. Appl. Phys.*, vol. 93, pp. 6265–6272, may 2003.

[82] Y. Chen, M. Zopf, R. Keil, F. Ding, and O. G. Schmidt, "Highly-efficient extraction of entangled photons from quantum dots using a broadband optical antenna," *Nat. Commun.*, vol. 9, p. 2994, jul 2018.

[83] D. G. Gérard, J. Wenger, A. Devilez, D. Gachet, B. Stout, N. Bonod, E. Popov, and H. Rigneault, "Strong electromagnetic confinement near dielectric microspheres to enhance single-molecule fluorescence," *Optical Society of America*, vol. 16, p. 15297, sep 2008.

[84] D. Gérard, A. Devilez, H. Aouani, B. Stout, N. Bonod, J. Wenger, E. Popov, and H. Rigneault, "Efficient excitation and collection of single-molecule fluorescence close to a dielectric microsphere," *Journal of the Optical Society of America B*, vol. 26, p. 1473, jun 2009.

[85] F. Biccari, T. Hamilton, A. Ristori, S. Sanguinetti, S. Bietti, M. Gurioli, and H. Mohseni, "Quantum dots luminescence collection enhancement and nanoscopy

by dielectric microspheres," *Particle & Particle Systems Characterization*, vol. 37, p. 1900431, dec 2019.

[86] M. Henini, *Dilute Nitride Semiconductors*. Elsevier, 2005.

[87] M. Kondow and F. Ishikawa, "High-quality growth of GaInNAs for application to near-infrared laser diodes," *Advances in Optical Technologies*, vol. 2012, pp. 1–11, nov 2012.

[88] I. Vurgaftman, J. R. Meyer, and L. R. Ram-Mohan, "Band parameters for III–v compound semiconductors and their alloys," *Journal of Applied Physics*, vol. 89, pp. 5815–5875, jun 2001.

[89] R. T. Senger and K. K. Bajaj, "Photoluminescence excitonic linewidth in GaAsN alloys," *Journal of Applied Physics*, vol. 94, no. 12, p. 7505, 2003.

[90] W. G. Bi and C. W. Tu, "Bowing parameter of the band-gap energy of GaNxAs1-x," *Applied Physics Letters*, vol. 70, pp. 1608–1610, mar 1997.

[91] K. Uesugi, N. Morooka, and I. Suemune, "Reexamination of n composition dependence of coherently grown GaNAs band gap energy with high-resolution x-ray diffraction mapping measurements," *Applied Physics Letters*, vol. 74, pp. 1254–1256, mar 1999.

[92] P. J. Klar, H. Grüning, W. Heimbrodt, J. Koch, F. Höhnsdorf, W. Stolz, P. M. A. Vicente, and J. Camassel, "From n isoelectronic impurities to n-induced bands in the GaNxAs1-x alloy," *Applied Physics Letters*, vol. 76, pp. 3439–3441, jun 2000.

[93] I. Schwartz, "Calculation of energy bands," *MATLAB Central File Exchange*, 2022.

[94] J. Wu, W. Shan, and W. Walukiewicz, "Band anticrossing in highly mismatched III v semiconductor alloys," *Semiconductor Science and Technology*, vol. 17, pp. 860–869, jul 2002.

[95] F. Masia, G. Pettinari, A. Polimeni, M. Felici, A. Miriametro, M. Capizzi, A. Lindsay, S. B. Healy, E. P. O'Reilly, A. Cristofoli, G. Bais, M. Piccin, S. Rubini, F. Martelli, A. Franciosi, P. J. Klar, K. Volz, and W. Stolz, "Interaction between conduction band edge and nitrogen states probed by carrier effective-mass measurements $InGaAs_{1-x}N_x$," *Phys. Rev. B*, vol. 73, p. 073201, feb 2006.

[96] G. Pettinari, F. Masia, A. Polimeni, M. Felici, A. Frova, M. Capizzi, A. Lindsay, E. P. O'Reilly, P. J. Klar, W. Stolz, G. Bais, M. Piccin, S. Rubini, F. Martelli, and A. Franciosi, "Influence of nitrogen-cluster states on the gyromagnetic factor of electrons in $GaAs_{1-x}N_x$," *Phys. Rev. B*, vol. 74, p. 245202, dec 2006.

[97] E. P. O'Reilly, A. Lindsay, P. J. Klar, A. Polimeni, and M. Capizzi, "Trends in the electronic structure of dilute nitride alloys," *Semiconductor Science and Technology*, vol. 24, p. 033001, feb 2009.

[98] C. G. V. de Walle and J. Neugebauer, "HYDROGEN IN SEMICONDUCTORS," *Annual Review of Materials Research*, vol. 36, pp. 179–198, aug 2006.

[99] E. Anders and M. Ebihara, "Solar-system abundances of the elements," *Geochimica et Cosmochimica Acta*, vol. 46, pp. 2363–2380, nov 1982.

[100] J. I. Pankove, "Chapter 3 hydrogenation of defects in crystalline silicon," in *Semiconductors and Semimetals*, pp. 35–47, Elsevier, 1991.

[101] D. E. Carlson and C. R. Wronski, "Amorphous silicon solar cell," *Applied Physics Letters*, vol. 28, pp. 671–673, jun 1976.

[102] H. Kang, "Crystalline silicon vs. amorphous silicon: the significance of structural differences in photovoltaic applications," *IOP Conference Series: Earth and Environmental Science*, vol. 726, p. 012001, apr 2021.

[103] L. Wen, M. Stavola, W. B. Fowler, R. Trotta, A. Polimeni, M. Capizzi, G. Bisognin, M. Berti, S. Rubini, and F. Martelli, "Microscopic origin of compressive strain in hydrogen-irradiated dilute $GaAs_{1-y}N_y$ alloys: Role of N-H_n centers with $n > 2$ and their thermal stability," *Phys. Rev. B*, vol. 86, p. 085206, aug 2012.

[104] R. Trotta, A. Polimeni, and M. Capizzi, "Hydrogen incorporation in III-N-V semiconductors: From macroscopic to nanometer control of the materials' physical properties," *Adv. Funct. Mater.*, vol. 22, no. 9, pp. 1782–1801, 2012.

[105] R. Trotta, D. Giubertoni, A. Polimeni, M. Bersani, M. Capizzi, F. Martelli, S. Rubini, G. Bisognin, and M. Berti, "Hydrogen diffusion in $GaAs_{1-x}N_x$," *Physical Review B*, vol. 80, p. 195206, nov 2009.

[106] N. Balakrishnan, G. Pettinari, O. Makarovsky, L. Turyanska, M. W. Fay, M. D. Luca, A. Polimeni, M. Capizzi, F. Martelli, S. Rubini, and A. Patanè, "Band-gap profiling by laser writing of hydrogen-containing III-n-vs," *Physical Review B*, vol. 86, p. 155307, oct 2012.

[107] G. Bisognin, D. D. Salvador, E. Napolitani, M. Berti, A. Polimeni, M. Capizzi, S. Rubini, F. Martelli, and A. Franciosi, "High-resolution x-ray diffraction *in situ* study of very small complexes: the case of hydrogenated dilute nitrides," *Journal of Applied Crystallography*, vol. 41, pp. 366–372, mar 2008.

[108] A. A. Bonapasta, F. Filippone, and G. Mattioli, "H-induced dangling bonds in h-isoelectronic-impurity complexes formed in $GaAs_{1-y}N_y$ alloys," *Physical Review Letters*, vol. 98, p. 206403, may 2007.

[109] S. Birindelli, M. Felici, J. S. Wildmann, A. Polimeni, M. Capizzi, A. Gerardino, S. Rubini, F. Martelli, A. Rastelli, and R. Trotta, "Single photons on demand from novel site-controlled GaAsN/GaAsN:H quantum dots," *Nano Lett.*, vol. 14, pp. 1275–1280, mar 2014.

[110] G. Pettinari, M. Felici, F. Biccari, M. Capizzi, and A. Polimeni, "Site-controlled quantum emitters in dilute nitrides and their integration in photonic crystal cavities," *Photonics*, vol. 5, p. 10, may 2018.

[111] M. Felici, G. Pettinari, F. Biccari, A. Boschetti, S. Younis, S. Birindelli, M. Gurioli, A. Vinattieri, A. Gerardino, L. Businaro, M. Hopkinson, S. Rubini, M. Capizzi, and

A. Polimeni, “Broadband enhancement of light-matter interaction in photonic crystal cavities integrating site-controlled quantum dots,” *Phys. Rev. B*, vol. 101, p. 205403, may 2020.

[112] G. Pettinari, L. A. Labbate, M. S. Sharma, S. Rubini, A. Polimeni, and M. Felici, “Plasmon-assisted bandgap engineering in dilute nitrides,” *Nanophotonics*, vol. 8, pp. 1465–1476, apr 2019.

[113] G. Pettinari, G. Marotta, F. Biccari, A. Polimeni, and M. Felici, “Tailoring the optical properties of dilute nitride semiconductors at the nanometer scale,” *Nanotechnology*, vol. 32, p. 185301, feb 2021.

[114] A. Zayats and D. Richards, *Nano-optics and near-field optical microscopy*. Norwood: Artech House, 2008.

[115] P. Bazylewski, S. Ezugwu, and G. Fanchini, “A review of three-dimensional scanning near-field optical microscopy (3d-SNOM) and its applications in nanoscale light management,” *Applied Sciences*, vol. 7, p. 973, sep 2017.

[116] F. Biccari, A. Boschetti, G. Pettinari, F. La China, M. Gurioli, F. Intonti, A. Vinattieri, M. S. Sharma, M. Capizzi, A. Gerardino, L. Businaro, M. Hopkinson, A. Polimeni, and M. Felici, “Site-controlled single-photon emitters fabricated by near-field illumination,” *Adv. Mater.*, vol. 30, p. 1705450, apr 2018.

[117] R. Trotta, A. Polimeni, M. Capizzi, F. Martelli, S. Rubini, M. Francardi, A. Gerardino, and L. Mariucci, “Light polarization control in strain-engineered GaAsN/GaAsN:h heterostructures,” *Applied Physics Letters*, vol. 94, p. 261905, jun 2009.

[118] J. Q. Grim, A. S. Bracker, M. Zalalutdinov, S. G. Carter, A. C. Kozen, M. Kim, C. S. Kim, J. T. Mlack, M. Yakes, B. Lee, and D. Gammon, “Scalable in operando strain tuning in nanophotonic waveguides enabling three-quantum-dot superradiance,” *Nature Materials*, vol. 18, pp. 963–969, jul 2019.

[119] F. Priolo, T. Gregorkiewicz, M. Galli, and T. F. Krauss, “Silicon nanostructures for photonics and photovoltaics,” *Nature Nanotechnology*, vol. 9, pp. 19–32, jan 2014.

[120] M. T. Mądzik, S. Asaad, A. Youssry, B. Joecker, K. M. Rudinger, E. Nielsen, K. C. Young, T. J. Proctor, A. D. Baczewski, A. Laucht, V. Schmitt, F. E. Hudson, K. M. Itoh, A. M. Jakob, B. C. Johnson, D. N. Jamieson, A. S. Dzurak, C. Ferrie, R. Blume-Kohout, and A. Morello, “Precision tomography of a three-qubit donor quantum processor in silicon,” *Nature*, vol. 601, no. 7893, pp. 348–353, 2022.

[121] A. Noiri, K. Takeda, T. Nakajima, T. Kobayashi, A. Sammak, G. Scappucci, and S. Tarucha, “Fast universal quantum gate above the fault-tolerance threshold in silicon,” *Nature*, vol. 601, no. 7893, pp. 338–342, 2022.

[122] X. Xue, M. Russ, N. Samkharadze, B. Undseth, A. Sammak, G. Scappucci, and L. M. K. Vandersypen, “Quantum logic with spin qubits crossing the surface code threshold,” *Nature*, vol. 601, pp. 343–347, jan 2022.

[123] X. Xue, B. Patra, J. P. G. van Dijk, N. Samkharadze, S. Subramanian, A. Corna, B. Paquelet Wuetz, C. Jeon, F. Sheikh, E. Juarez-Hernandez, B. P. Esparza, H. Rampurawala, B. Carlton, S. Ravikumar, C. Nieva, S. Kim, H.-J. Lee, A. Sammak, G. Scappucci, M. Veldhorst, F. Sebastiano, M. Babaie, S. Pellerano, E. Charbon, and L. M. K. Vandersypen, "Cmos-based cryogenic control of silicon quantum circuits," *Nature*, vol. 593, no. 7858, pp. 205–210, 2021.

[124] A. M. J. Zwerver, T. Krähenmann, T. F. Watson, L. Lampert, H. C. George, R. Pillarisetty, S. A. Bojarski, P. Amin, S. V. Amitonov, J. M. Boter, R. Caudillo, D. Correas-Serrano, J. P. Dehollain, G. Droulers, E. M. Henry, R. Kotlyar, M. Lodari, F. Lüthi, D. J. Michalak, B. K. Mueller, S. Neyens, J. Roberts, N. Samkharadze, G. Zheng, O. K. Zietz, G. Scappucci, M. Veldhorst, L. M. K. Vandersypen, and J. S. Clarke, "Qubits made by advanced semiconductor manufacturing," *Nature Electronics*, vol. 5, no. 3, pp. 184–190, 2022.

[125] L. Weiss, A. Gritsch, B. Merkel, and A. Reiserer, "Erbium dopants in nanophotonic silicon waveguides," *Optica*, vol. 8, no. 1, pp. 40–41, 2021.

[126] E. MacQuarrie, C. Chartrand, D. Higginbottom, K. Morse, V. Karasyuk, S. Roorda, and S. Simmons, "Generating t centres in photonic silicon-on-insulator material by ion implantation," *New Journal of Physics*, vol. 23, no. 10, p. 103008, 2021.

[127] C. Chartrand, L. Bergeron, K. Morse, H. Riemann, N. Abrosimov, P. Becker, H.-J. Pohl, S. Simmons, and M. Thewalt, "Highly enriched ^{28}si reveals remarkable optical linewidths and fine structure for well-known damage centers," *Physical Review B*, vol. 98, no. 19, p. 195201, 2018.

[128] G. Zhang, Y. Cheng, J.-P. Chou, and A. Gali, "Material platforms for defect qubits and single-photon emitters," *Applied Physics Reviews*, vol. 7, no. 3, p. 031308, 2020.

[129] G. Davies, S. Hayama, L. Murin, R. Krause-Rehberg, V. Bondarenko, A. Sengupta, C. Davia, and A. Karpenko, "Radiation damage in silicon exposed to high-energy protons," *Physical Review B*, vol. 73, no. 16, p. 165202, 2006.

[130] L. Bergeron, C. Chartrand, A. T. K. Kurkjian, K. J. Morse, H. Riemann, N. V. Abrosimov, P. Becker, H. J. Pohl, M. L. W. Thewalt, and S. Simmons, "Characterization of the t center in ^{28}si," *arXiv*, 2020.

[131] G. Davies, E. C. Lightowlers, and Z. E. Ciechanowska, "The 1018 meV (w or i_1) vibronic band in silicon," *Journal of Physics C: Solid State Physics*, vol. 20, pp. 191–205, jan 1987.

[132] G. Davies, A. Oates, R. Newman, R. Woolley, E. Lightowlers, M. Binns, and J. Wilkes, "Carbon-related radiation damage centres in czochralski silicon," *Journal of Physics C: Solid State Physics*, vol. 19, no. 6, p. 841, 1986.

[133] A. Safonov, E. Lightowlers, G. Davies, P. Leary, R. Jones, and S. Öberg, "Interstitial-carbon hydrogen interaction in silicon," *Physical review letters*, vol. 77, no. 23, p. 4812, 1996.

[134] P. Udvarhelyi, B. Somogyi, G. Thiering, and A. Gali, "Identification of a telecom wavelength single photon emitter in silicon," *Physical review letters*, vol. 127, no. 19, p. 196402, 2021.

[135] C. Beaufils, W. Redjem, E. Rousseau, V. Jacques, A. Y. Kuznetsov, C. Raynaud, C. Voisin, A. Benali, T. Herzig, S. Pezzagna, J. Meijer, M. Abbarchi, and G. Cassabois, "Optical properties of an ensemble of g-centers in silicon," *Physical Review B*, vol. 97, p. 035303, jan 2018.

[136] M. Hollenbach, Y. Berencén, U. Kentsch, M. Helm, and G. V. Astakhov, "Engineering telecom single-photon emitters in silicon for scalable quantum photonics," *Optics Express*, vol. 28, no. 18, pp. 26111–26121, 2020.

[137] W. Redjem, A. Durand, T. Herzig, A. Benali, S. Pezzagna, J. Meijer, A. Y. Kuznetsov, H. S. Nguyen, S. Cueff, J.-M. Gérard, I. Robert-Philip, B. Gil, D. Caliste, P. Pochet, M. Abbarchi, V. Jacques, A. Dréau, and G. Cassabois, "Single artificial atoms in silicon emitting at telecom wavelengths," *Nature Electronics*, vol. 3, pp. 738–743, nov 2020.

[138] M. Prabhu, C. Errando-Herranz, L. De Santis, I. Christen, C. Chen, and D. R. Englund, "Individually addressable artificial atoms in silicon photonics," *arXiv preprint arXiv:2202.02342*, 2022.

[139] C. E. Dreyer, A. Alkauskas, J. L. Lyons, A. Janotti, and C. G. V. de Walle, "First-principles calculations of point defects for quantum technologies," *Annual Review of Materials Research*, vol. 48, pp. 1–26, jul 2018.

[140] R. J. Spry and W. D. Compton, "Recombination luminescence in irradiated silicon," *Phys. Rev.*, vol. 175, pp. 1010–1020, Nov 1968.

[141] C. E. Jones, E. S. Johnson, W. D. Compton, J. R. Noonan, and B. G. Streetman, "Temperature, stress, and annealing effects on the luminescence from electron-irradiated silicon," *Journal of Applied Physics*, vol. 44, no. 12, pp. 5402–5410, 1973.

[142] J. L. Benton, J. Michel, L. C. Kimerling, B. E. Weir, and R. A. Gottscho, "Carbon reactions in reactive ion etched silicon," *Journal of Electronic Materials*, vol. 20, pp. 643–647, sep 1991.

[143] S. G. Cloutier, P. A. Kossyrev, and J. Xu, "Optical gain and stimulated emission in periodic nanopatterned crystalline silicon," *Nature materials*, vol. 4, no. 12, pp. 887–891, 2005.

[144] E. Rotem, J. M. Shainline, and J. M. Xu, "Enhanced photoluminescence from nanopatterned carbon-rich silicon grown by solid-phase epitaxy," *Applied Physics Letters*, vol. 91, p. 051127, jul 2007.

[145] K. Murata, Y. Yasutake, K.-i. Nittoh, S. Fukatsu, and K. Miki, "High-density g-centers, light-emitting point defects in silicon crystal," *Aip Advances*, vol. 1, no. 3, p. 032125, 2011.

[146] D. D. Berhanuddin, M. A. Lourenço, R. M. Gwilliam, and K. P. Homewood, "Co-implantation of carbon and protons: An integrated silicon device technology compatible method to generate the lasing g-center," *Advanced Functional Materials*, vol. 22, pp. 2709–2712, apr 2012.

[147] Y. Baron, A. Durand, T. Herzig, M. Khoury, S. Pezzagna, J. Meijer, I. Robert-Philip, M. Abbarchi, J.-M. Hartmann, S. Reboh, J.-M. Gérard, V. Jacques, G. Cassabois, and A. Dréau, "Single g centers in silicon fabricated by co-implantation with carbon and proton," *Applied Physics Letters*, vol. 121, p. 084003, aug 2022.

[148] C. Schuck, X. Guo, L. Fan, X. Ma, M. Poot, and H. X. Tang, "Quantum interference in heterogeneous superconducting-photonic circuits on a silicon chip," *Nature communications*, vol. 7, no. 1, pp. 1–7, 2016.

[149] J. Sprengers, A. Gaggero, D. Sahin, S. Jahanmirinejad, G. Frucci, F. Mattioli, R. Leoni, J. Beetz, M. Lermer, M. Kamp, *et al.*, "Waveguide superconducting single-photon detectors for integrated quantum photonic circuits," *Applied Physics Letters*, vol. 99, no. 18, p. 181110, 2011.

[150] L. Canham, K. Barraclough, and D. Robbins, "1.3-μm light-emitting diode from silicon electron irradiated at its damage threshold," *Applied physics letters*, vol. 51, no. 19, pp. 1509–1511, 1987.

[151] L. Zhu, S. Yuan, C. Zeng, and J. Xia, "Manipulating photoluminescence of carbon g-center in silicon metasurface with optical bound states in the continuum," *Advanced Optical Materials*, vol. 8, no. 8, p. 1901830, 2020.

[152] J. M. Ulloa, P. M. Koenraad, and M. Hopkinson, "Structural properties of GaAsN/GaAs quantum wells studied at the atomic scale by cross-sectional scanning tunneling microscopy," *Appl. Phys. Lett.*, vol. 93, p. 083103, aug 2008.

[153] I. Tiginyanu, V. Ursaki, and V. Popa, "Nanoimprint lithography (NIL) and related techniques for electronics applications," in *Nanocoatings and Ultra-Thin Films*, pp. 280–329, Elsevier, 2011.

[154] C. Acikgoz, M. A. Hempenius, J. Huskens, and G. J. Vancso, "Polymers in conventional and alternative lithography for the fabrication of nanostructures," *European Polymer Journal*, vol. 47, pp. 2033–2052, nov 2011.

[155] J. Proust, F. Bedu, S. Chenot, I. Soumahoro, I. Ozerov, B. Gallas, R. Abdeddaim, and N. Bonod, "Chemical alkaline etching of silicon mie particles," *Advanced Optical Materials*, vol. 3, pp. 1280–1286, may 2015.

[156] K. E. Chong, B. Hopkins, I. Staude, A. E. Miroshnichenko, J. Dominguez, M. Decker, D. N. Neshev, I. Brener, and Y. S. Kivshar, "Observation of fano resonances in all-dielectric nanoparticle oligomers," *Small*, vol. 10, pp. 1985–1990, feb 2014.

[157] T. Coenen, J. van de Groep, and A. Polman, "Resonant modes of single silicon nanocavities excited by electron irradiation," *ACS Nano*, vol. 7, pp. 1689–1698, jan 2013.

[158] V. R. Manfrinato, A. Stein, L. Zhang, C.-Y. Nam, K. G. Yager, E. A. Stach, and C. T. Black, “Aberration-corrected electron beam lithography at the one nanometer length scale,” *Nano Letters*, vol. 17, pp. 4562–4567, apr 2017.

[159] F. Karouta, K. Vora, J. Tian, and C. Jagadish, “Structural, compositional and optical properties of PECVD silicon nitride layers,” *Journal of Physics D: Applied Physics*, vol. 45, p. 445301, oct 2012.

[160] M. Morita, T. Ohmi, E. Hasegawa, M. Kawakami, and M. Ohwada, “Growth of native oxide on a silicon surface,” *Journal of Applied Physics*, vol. 68, pp. 1272–1281, aug 1990.

[161] G. Pettinari, A. Gerardino, L. Businaro, A. Polimeni, M. Capizzi, M. Hopkinson, S. Rubini, F. Biccari, F. Intonti, A. Vinattieri, M. Gurioli, and M. Felici, “A lithographic approach for quantum dot-photonic crystal nanocavity coupling in dilute nitrides,” *Microelectron. Eng.*, vol. 174, pp. 16–19, apr 2017.

[162] K. Vedam, “Spectroscopic ellipsometry: a historical overview,” *Thin Solid Films*, vol. 313-314, pp. 1–9, feb 1998.

[163] M. Ledinský, L. Fekete, J. Stuchlík, T. Mates, A. Fejfar, and J. Kočka, “Characterization of mixed phase silicon by raman spectroscopy,” *Journal of Non-Crystalline Solids*, vol. 352, pp. 1209–1212, jun 2006.

[164] T. R. Hart, R. L. Aggarwal, and B. Lax, “Temperature dependence of raman scattering in silicon,” *Physical Review B*, vol. 1, pp. 638–642, jan 1970.

[165] R. J. Angel, M. Murri, B. Mihailova, and M. Alvaro, “Stress, strain and raman shifts,” *Zeitschrift für Kristallographie - Crystalline Materials*, vol. 234, pp. 129–140, sep 2018.

[166] J. B. Schneider, “Understanding the finite-difference time-domain method,” *www.eecs.wsu.edu/ schneidj/ufdtd*, 2010.

[167] A. Egel, K. M. Czajkowski, D. Theobald, K. Ladutenko, A. S. Kuznetsov, and L. Pattelli, “SMUTHI: A python package for the simulation of light scattering by multiple particles near or between planar interfaces,” *Journal of Quantitative Spectroscopy and Radiative Transfer*, vol. 273, p. 107846, oct 2021.

[168] J. F. Ziegler and J. P. Biersack, “The stopping and range of ions in matter,” in *Treatise on heavy-ion science*, pp. 93–129, Springer, 1985.

[169] Z. Chen, A. Taflove, and V. Backman, “Photonic nanojet enhancement of backscattering of light by nanoparticles: a potential novel visible-light ultramicroscopy technique,” *Optics Express*, vol. 12, no. 7, p. 1214, 2004.

[170] A. V. Itagi and W. A. Challener, “Optics of photonic nanojets,” *Journal of the Optical Society of America A*, vol. 22, p. 2847, Dec. 2005.

[171] A. Heifetz, S. C. Kong, A. V. Sahakian, A. Taflove, and V. Backman, “Photonic nanojets,” *J. Comput. Theor. Nanosci.*, vol. 6, pp. 1979–1992, sep 2009.

[172] A. Mandal and V. R. Dantham, "Photonic nanojets generated by single microspheres of various sizes illuminated by resonant and non-resonant focused gaussian beams of different waists," *Journal of the Optical Society of America B*, vol. 37, p. 977, Mar. 2020.

[173] T. Jalali and D. Erni, "Highly confined photonic nanojet from elliptical particles," *Journal of Modern Optics*, vol. 61, pp. 1069–1076, June 2014.

[174] M. Yousefi, D. Necesal, T. Scharf, and M. Rossi, "Structured light engineering using a photonic nanojet," *arXiv*, Mar. 2021.

[175] V. Pacheco-Peña, M. Beruete, I. V. Minin, and O. V. Minin, "Terajets produced by dielectric cuboids," *Applied Physics Letters*, vol. 105, p. 084102, Aug. 2014.

[176] D. Grojo, N. Sandeau, L. Boarino, C. Constantinescu, N. D. Leo, M. Laus, and K. Sparnacci, "Bessel-like photonic nanojets from core-shell sub-wavelength spheres," *Optics Letters*, vol. 39, p. 3989, June 2014.

[177] Y.-J. Wang, C.-A. Dai, and J.-H. Li, "Numerical study of tunable photonic nanojets generated by biocompatible hydrogel core-shell microspheres for surface-enhanced raman scattering applications," *Polymers*, vol. 11, p. 431, Mar. 2019.

[178] D. McCloskey, J. J. Wang, and J. Donegan, "Low divergence photonic nanojets from si_3n_4 microdisks," *Optics Express*, vol. 20, p. 128, Dec. 2011.

[179] C. Zhang, J. Lin, and M. Gu, "High-quality longitudinally polarized photonic nanojet created by a microdisk," *Optics Letters*, vol. 46, p. 3127, June 2021.

[180] Y. E. Geints, A. A. Zemlyanov, and E. K. Panina, "Microaxicon-generated photonic nanojets," *Journal of the Optical Society of America B*, vol. 32, p. 1570, July 2015.

[181] Z. Hengyu, C. Zaichun, C. T. Chong, and H. Minghui, "Photonic jet with ultralong working distance by hemispheric shell," *Optics Express*, vol. 23, p. 6626, Mar. 2015.

[182] C.-B. Lin, Y.-H. Lin, W.-Y. Chen, and C.-Y. Liu, "Photonic nanojet modulation achieved by a spider-silk-based metal–dielectric dome microlens," *Photonics*, vol. 8, p. 334, Aug. 2021.

[183] U. Katsuhiro, S. Ikuo, H. Tatsuo, A. Tomoyuki, and N. Takayoshi, "Temperature dependence of band gap energies of GaAsN alloys," *Appl. Phys. Lett.*, vol. 76, p. 1285, feb 2000.

[184] M. Abbarchi, C. Mastrandrea, T. Kuroda, T. Mano, A. Vinattieri, K. Sakoda, and M. Gurioli, "Poissonian statistics of excitonic complexes in quantum dots," *J. Appl. Phys.*, vol. 106, p. 053504, sep 2009.

[185] M. Abbarchi, C. Mastrandrea, T. Kuroda, T. Mano, A. Vinattieri, T. Mano, N. Koguchi, K. Sakoda, and M. Gurioli, "Line broadening of excitonic complexes in self-assembled GaAs/AlGaAs single quantum dots," *Phys. Status Solidi C*, vol. 6, pp. 886–889, apr 2009.

[186] M. Pelton, C. Santori, J. Vučković, B. Zhang, G. S. Solomon, J. Plant, and Y. Yamamoto, "Efficient source of single photons: A single quantum dot in a micropost microcavity," *Phys. Rev. Lett.*, vol. 89, p. 233602, nov 2002.

[187] A. Mohan, P. Gallo, M. Felici, B. Dwir, A. Rudra, J. Faist, and E. Kapon, "Engineering conduction and valence band states in site-controlled pyramidal quantum dots," *Appl. Phys. Lett.*, vol. 98, p. 253102, jun 2011.

[188] N. Ha, T. Mano, Y.-L. Chou, Y.-N. Wu, S.-J. Cheng, J. Bocquel, P. M. Koenraad, A. Ohtake, Y. Sakuma, K. Sakoda, and T. Kuroda, "Size-dependent line broadening in the emission spectra of single GaAs quantum dots: Impact of surface charge on spectral diffusion," *Phys. Rev. B*, vol. 92, p. 075306, aug 2015.

[189] J. Hou, M. Li, and Y. Song, "Patterned colloidal photonic crystals," *Angew. Chem. Int. Ed.*, vol. 57, no. 10, pp. 2544–2553, 2018.

[190] J.-Y. Choi, T. L. Alford, and C. B. Honsberg, "Solvent-controlled spin-coating method for large-scale area deposition of two-dimensional silica nanosphere assembled layers," *Langmuir*, vol. 30, pp. 5732–5738, may 2014.

[191] K. Papatryfonos, T. Angelova, A. Brimont, B. Reid, S. Guldin, P. R. Smith, M. Tang, K. Li, A. J. Seeds, H. Liu, and D. R. Selviah, "Refractive indices of MBE-grown AlxGa(1-x)as ternary alloys in the transparent wavelength region," *AIP Advances*, vol. 11, p. 025327, Feb. 2021.

[192] I. H. Malitson, "Interspecimen comparison of the refractive index of fused silica," *Journal of the Optical Society of America*, vol. 55, p. 1205, Oct. 1965.

[193] M. Rebien, W. Henrion, M. Hong, J. P. Mannaerts, and M. Fleischer, "Optical properties of gallium oxide thin films," *Applied Physics Letters*, vol. 81, pp. 250–252, July 2002.

[194] B. Schwartz, "GaAs surface chemistry - a review," *C R C Critical Reviews in Solid State Sciences*, vol. 5, pp. 609–624, Nov. 1975.

[195] R. S. Bonilla, B. Hoex, P. Hamer, and P. R. Wilshaw, "Dielectric surface passivation for silicon solar cells: A review," *physica status solidi (a)*, vol. 214, p. 1700293, jun 2017.

[196] J. H. Parker, D. W. Feldman, and M. Ashkin, "Raman scattering by silicon and germanium," *Physical Review*, vol. 155, pp. 712–714, mar 1967.

[197] V. Senez, A. Armigliato, I. D. Wolf, G. Carnevale, R. Balboni, S. Frabboni, and A. Benedetti, "Strain determination in silicon microstructures by combined convergent beam electron diffraction, process simulation, and micro-raman spectroscopy," *Journal of Applied Physics*, vol. 94, pp. 5574–5583, nov 2003.

[198] X. Wu, J. Yu, T. Ren, and L. Liu, "Micro-raman spectroscopy measurement of stress in silicon," *Microelectronics Journal*, vol. 38, pp. 87–90, jan 2007.

[199] C. P. Foy, M. C. do Carmo, G. Davies, and E. C. Lightowlers, “Uniaxial stress measurements on the 0.97 eV line in irradiated silicon,” *Journal of Physics C: Solid State Physics*, vol. 14, pp. L7–L12, jan 1981.

[200] K. Thonke, H. Klemisch, J. Weber, and R. Sauer, “New model of the irradiation-induced 0.97-eV (G) line in silicon: A $C_S - Si^*$ complex,” *Physical Review B*, vol. 24, pp. 5874–5886, nov 1981.

[201] S. Tiwari, *Semiconductor Physics: Principles, Theory and Nanoscale*. Electroscience Series, OUP Oxford, 2020.

[202] A. Rastelli, F. Ding, J. D. Plumhof, S. Kumar, R. Trotta, C. Deneke, A. Malachias, P. Atkinson, E. Zallo, T. Zander, A. Herklotz, R. Singh, V. Křápek, J. R. Schröter, S. Kiravittaya, M. Benyoucef, R. Hafenbrak, K. D. Jöns, D. J. Thurmer, D. Grimm, G. Bester, K. Dörr, P. Michler, and O. G. Schmidt, “Controlling quantum dot emission by integration of semiconductor nanomembranes onto piezoelectric actuators,” *physica status solidi (b)*, vol. 249, pp. 687–696, feb 2012.

[203] J. Shay and R. Nahory, “Exciton reflectance and photoreflectance in GaAs,” *Solid State Communications*, vol. 7, pp. 945–948, jul 1969.

[204] H.-P. Komsa, E. Arola, E. Larkins, and T. T. Rantala, “Band offset determination of the GaAs/GaAsN interface using the density functional theory method,” *Journal of Physics: Condensed Matter*, vol. 20, p. 315004, jun 2008.

[205] B. Gil and P. Bigenwald, “Exciton binding energies and oscillator strengths in GaAsN-GaAs quantum wells,” *physica status solidi (a)*, vol. 183, pp. 111–116, jan 2001.

[206] A. S. Baltenkov and A. Z. Msezane, “Electronic quantum confinement in cylindrical potential well,” *Eur. Phys. J. D*, vol. 70, p. 81, apr 2016.

[207] T. Dannecker, Y. Jin, H. Cheng, C. F. Gorman, J. Buckeridge, C. Uher, S. Fahy, C. Kurdak, and R. S. Goldman, “Nitrogen composition dependence of electron effective mass in $GaAs_{1-x}N_x$,” *Phys. Rev. B*, vol. 82, p. 125203, sep 2010.

[208] T. S. Koh, Y. P. Feng, X. Xu, and H. N. Spector, “Excitons in semiconductor quantum discs,” *Journal of Physics: Condensed Matter*, vol. 13, pp. 1485–1498, jan 2001.